Combined therapy of SMN-ASO and Plastin 3 overexpression rescues severe SMA in mice

Inaugural-Dissertation

zur

Erlangung des Doktorgrades

der Mathematisch-Naturwissenschaftlichen Fakultät

der Universität zu Köln

vorgelegt von

Miriam Peters

aus München

Köln 2017

This Doctoral Thesis "PLS3 as a protective modifier in an intermediate mouse model of SMA" was performed at the Institute of Human Genetics, Institute of Genetics and Center for Molecular Medicine Cologne (CMMC) of the University of Cologne from May 2012 to November 2016.

Berichterstatter: Prof. Dr. Brunhilde Wirth

                      Prof. Dr. Sigrun Korsching

Tag der mündlichen Prüfung: 16.01.17

Für meine Eltern

Acknowledgements - Danksagung

Table of Contents

Abbreviations

3'	3-prime (for nucleic acids)
5'	5-prime (for nucleic acids)
ACh	Acetylcholine
AChR	Acetylcholine receptor
ADF	Actin destabilizing factor
ADP	Adenosindiphosphat
approx.	approximately
APS	Ammonium persulfate
ARF	ADP ribosylation Factor
ASO	Antisense oligonucleotide
ATX2	Ataxin-2
BBB	Blood brain barrier
BDNF	Brain-derived neurotrophic factor
ß-ME	ß-Mercaptoethanol
bp	base pairs
BSA	Bovine serum albumine
CaMKII	Ca^{2+}/calmodulin-dependent protein kinase II
CB	Cajal body
Cdk5	Cyclin dependent kinase 5
ChAT	Choline acetyltransferase
CHO	Chinese hamster ovary
CNTF	Ciliary Neurotrophic Factor
CNV	copy number variant
CV-1	Cercopithecus aethiops monkey kidney cell line
dATP	deoxyadenosine triphosphate
dCTP	deoxycytidine triphosphate
DEPC	Diethylpyrocarbonate
dGTP	deoxyguanosine triphosphate
DMSO	Dimethyl sulfoxide
DNA	Deoxyribonucleic acid
dNTP	deoxynucleoside triphosphate
dpc	dies post coitum (days after copulation)
DTT	Dithiothreitol
dTTP	deoxythymidine triphosphate
EDTA	Ethylenediaminetetraacetic acid
EM	Electron microscopy
ESE	Exonic splicing enhancer
EtOH	Ethanol

FBS	Fetal bovine serum
FL	full-length
FMRP	Fragile X mental retardation syndrome protein
fwd	forward
GAP43	cytoskeleton-associated growth-associated protein 43
Gapdh	Glyceraldehyde 3-phosphate dehydrogenase
GC	Gastrocnemius muscle
GDNF	Glial cell-derived neurotrophic factor
GTP	Guanosine triphosphate
h	hour(s)
HDAC	Histone deacetylase
HDACi	Histone deacetylase inhibitor
HBSS	Hanks' Balanced Salt Solution
HLS	Hind limb score
hnRNP	Heterogeneous nuclear ribonuclear protein
HPRT	Hypoxanthine phosphoribosyltransferase
HRP	Horseradish peroxidase
HSP	Heat-shock-protein
HuD	Hu-antigen D protein
Ig	Immunoglobulin
ILV	intraluminal vesicle
IPSC	Induced pluripotent stem cell
IMP1	Insulin-like growth factor-II mRNA-binding protein 1
KO	Knock-out
LE	Late endosome
LLC-PK1	Lilly laboratories ell for porcine kidney cell line
MEF	Murine embryonic fibroblast
min	minute(s)
MN	Motor neuron
NaAc	Sodium acetate
NF	Neurofilament
NGF	Nerve growth factor
NGS	Next generation sequencing
NMJ	Neuromuscular junction
NSF	N-Ethylmaleimide-sensitive factor
NT3	Neurotrophin-3
NT4/5	Neurotrophin-4/5
PABP	Poly(A)-binding protein
PBS	Phosphate buffered saline
PCR	Polymerase chain reaction
PFA	Paraformaldehyde
PKA	Protein kinase A
PLS3	Plastin-3

PtdIns(4,5)P$_2$ Phosphatidylinositol *4,5*-bisphosphate
PVDF   Polyvinylidene fluoride
rev   reverse
RNA   Ribonucleic acid
ROI   Region of interest
rpm   revolutions per minute
RT   Room temperature
SAHA   Suberoylanilide hydroxamic acid
s. c.   spinal cord
scAAV9   adeno-associated virus 9
SD   Standard deviation
SDS   Sodium dodecyl sulfate
sec   second(s)
SEM   Standard error of the mean
SG   Stress granules
SLE   Systemic lupus erythematosus
Sm   Smith antigen
SMA   Spinal muscular atrophy
SMN1   Survival of motor neuron gene 1
SMN2   Survival of motor neuron gene 2
SNAP   NSF attachment proteins
SNARE   SNAP receptors
snRNA   Small nuclear RNA
snRNP   Small nuclear ribonucleoprotein
SV2   Synaptic vesicle glycoprotein 2A; synaptic vesicles
TBE   Tris buffered EDTA
TBS   Tris buffered saline
TBST   Tris buffered saline Tween-20
TEMED   Tertramethylethylenediamine
TVA   Transverse abdominis
UNRIP   UNR-interacting protein
VAP   Valproic acid
VGlut1   Vesicular glutamate transporter 1
vol.   Volume
vs.   versus
wt   wildtype

List of Tables

List of Figures

1. Introduction

1.1 SPINAL MUSCULAR ATROPHY

Spinal muscular atrophy as a general term includes many different motor neuron disorders, in which proximal muscles and motor neurons are involved. Due to different modes of inheritance, there exist several possible forms of spinal muscular atrophies that include autosomal dominant and recessive, as well as X-linked ones. Among these are spinal muscular atrophy with respiratory distress (SMARD) (Grohmann et al. 2003), spinal and bulbar muscular atrophy (Kennedy's disease), X-linked spinal muscular atrophy (XL-SMA) (Baumbach-Reardon et al. 1993) and distal spinal muscular atrophy (Takata et al. 2004). In this thesis, spinal muscular atrophy refers to the recessive autosomal type, caused by functional loss of SMN1 gene.

Nowadays, autosomal recessive proximal spinal muscular atrophy (SMA) is the leading genetic cause of infant death (Montes et al. 2009). In the Western European population, SMA is the second most frequent autosomal recessive disorder in humans after cystic fibrosis. The incidence of SMA is 1 in 10,000 live births in Western Europe (Pearn 1978; Emery 1991). The carrier frequency is 1:35 – 1:40 (Feldkotter et al. 2002; Wirth et al. 2013). Homozygous loss or mutation of the disease-causing *Survival of motor neuron gene 1 (SMN1)* located on chromosome 5q13 (Brzustowicz et al. 1990; Melki et al. 1990) leads to SMA. This results in the degeneration of spinal α-motor neurons as well as their respective efferent axons. As a consequence, affected individuals suffer from progressive weakness of muscles.

1.1.1 Symptoms

SMA is caused by the progressive degeneration of α-motor neurons in the anterior horns of the spinal cord. This leads to a steadily increasing hypotonia and weakness of the voluntary muscles, e.g. limb or intercostal muscle of the chest and ultimately resulting in the atrophy of proximal voluntary muscles. Although diaphragmatic strength is usually intact, weakening of intercostal chest muscles can lead to a severely restrictive lung deficit and finally to the need of ventilatory support (Markowitz et al. 2004). While the atrophy is more pronounced in the lower extremities, hands and feet are usually spared in the early stages of SMA

(Markowitz et al. 2004). Later symptoms, especially in the less affected type II, III or IV patients (1.1.2), typically also include progressive weakening of the distal muscle. Since muscles of the legs are affected first, patients will usually be wheelchair bound or suffer major problems in climbing stairs or getting up from the floor. With ongoing progression and depending on the severity of the disease, further symptoms include a weak cough, difficulties to suck and swallow, bladder weakness, tremor of the hands, areflexia and an increased susceptibility to respiratory tract infections (Rudnik-Schöneborn et al. 1994). In contrast, facial and oculomotor nerves are typically unaffected and also cognitive skills are not impaired. The denervation of muscle finally results in atrophy, whereby often a few residual motor neurons stay connected. The uncontrolled and sporadic firing of such remaining motor neurons leads to twitching (fasciculation), particular of the tongue and fingers, a finding often used in diagnosis (Markowitz et al. 2004).

1.1.2 Classification

Phenotypical variation of SMA, ranging from very severe forms with early onset to rather mild chronic SMA disease, led to the development of a classification scheme for SMA. The characteristics of five types (SMA type 0-IV) will briefly be outlined as defined by the International SMA Consortium in 1992 (Munsat and Davies 1992). Classification criteria that are relevant to the clinic were used to define types of SMA, among these are age of onset and distribution of muscle weakness (Russman 2007; Wang et al. 2007). Type 0 SMA is considered the most severe form of SMA with perinatal onset, problems to swallow and breath, possible facial dysplasia and no motoric abilities (Russman 2007). Type I SMA (*Werdnig-Hoffmann* disease), also called the infantile acute form of SMA, accounts for ~60% of all SMA cases (Werdnig 1891; Pearn 1978; Markowitz et al. 2004; Monani and De Vivo 2014). The onset of disease is before the age of 6 months with a life expectancy of less than two years (Rudnik-Schoneborn et al. 2009). The proportion of patients surviving more than 2 years is ~6% (Rudnik-Schoneborn et al. 2009; Cobben and de Visser 2002; Carre and Empey 2016). Patients will never be able to sit or walk independently. Proximal intercostal muscles are strongly affected and patients suffer from severe breathing problems concomitant with an increased infection rate. Many patients undergo gastrostomy for swallowing problems and are not able to thrive properly, or are in need of a non-invasive ventilation and tracheostomy due to their respiratory difficulties (De Sanctis et al. 2016). The onset of type II SMA (intermediate form) is between 6 and 18 months. Patients are mostly

able to sit but cannot walk. The prognosis is rather variable depending on the degree of respiratory muscle involvement and the problems associated with the development of kyphoscoliosis (Talbot 1999). Type III SMA or juvenile SMA (Kugelberg and Welander 1956) is quite variable in its age of onset but generally first symptoms occur after the 18th month of life. Depending on the exact age of onset, SMA type III is divided into two subtypes: if first symptoms are diagnosed before the age of three years, the disease is called type IIIa, if the patient is older than three years it is called type IIIb (Zerres and Rudnik-Schoneborn 1995). Type III SMA is very heterogeneous, as some affected individuals may need wheelchair assistance in childhood, whereas others may continue to walk throughout their whole lives. SMA Type IV (adult form) is a very mild form of SMA with a rather late onset beyond the age of 30 (Zerres and Rudnik-Schoneborn 1995). As in all SMA forms, weakness is progressive but affects mostly proximal muscles. Type IV patients have a normal life expectancy.

1.1.3 SMN1 and SMN2 genes

In 1995, the *survival of motor neuron 1 gene* (*SMN1*) was identified as the SMA-determining gene (Lefebvre et al. 1995), while *SMN2*, a paralog of *SMN1*, is the major modifier of SMA disease severity (Feldkotter et al. 2002). Each *SMN* gene copy lies within a repeat unit of a copy number variant (CNV) on chromosome 5q13, while each repeat unit is about 500 kb and oriented in inverse direction (Lefebvre et al. 1995; Burglen et al. 1996). The *SMN1* gene encompasses a 28 kb genomic region and comprises 10 exons (1, 2a, 2b, 3, 4, 5, 6a, 6b, 7 and 8). The coding sequence of *SMN1* is 882 bp and produces a ~1.5 kb transcript, which is ubiquitously expressed (Lefebvre et al. 1995; Chen et al. 1998) and encodes for a protein of 294 amino acids. *SMN1* was found to be highly conserved between species (Miguel-Aliaga et al. 1999; Paushkin et al. 2000), emphasizing that it is essential for every organism. *SMN2* differs from *SMN1* by only five nucleotide exchanges localized at the 3'end of the genes: one nucleotide exchange in each of the exons 7 and 8 and intron 6 and two in intron 7 (Lefebvre et al. 1995; Burglen et al. 1996). Besides *SMN*, another four genes have been shown to be included in the duplicated 500 kb segment: *BIRC1* (*baculoviral IAP repeat-containing protein 1*) which is also known as *NAIP* (*neuronal apoptosis inhibitory protein*), *SERF1* (*small EDRK-rich factor 1*), also termed *H4F5*, *GTF2H2* (*general transcription factor IIH*) or p44 (Figure 1), and *OCLN* (*occludin*) (Lefebvre et al. 1995; Schmutz et al. 2004). Proximally, this highly polymorphic region is flanked by *RAD17*, whereas the distally adjacent gene is *BDP1* (Deimling von et al. 1999; Kelter et al. 2000).
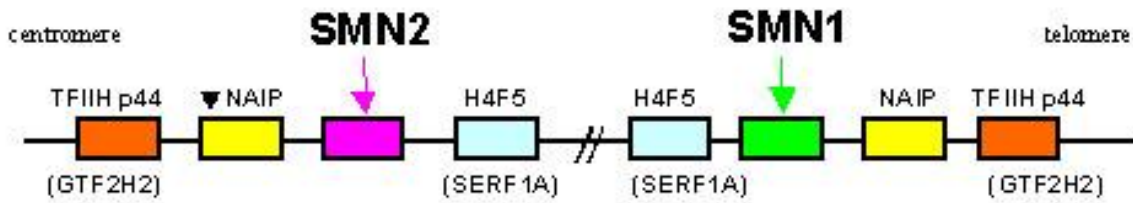
Figure 1: 500 kb telomeric and centromeric region containing *SMN1* and its duplicated version *SMN2*, respectively. In the centromeric region, a nearly identical copy of *SMN1* is located, termed *SMN2*, which has been found to be present in all SMA patients. *SMN2* differs from *SMN1* by only 5 silent discrepancies: a synonymous mutation in exon 7 (c.C280T in *SMN2*), exon 8 (nt 27869 G>A), intron 6 (nt 27092 G>A) and another two in Intron 7 (nt 27289 A>G and 27404 A>G) (Lefebvre et al. 1995; Burglen et al. 1996).

All other variants are not specific to either of the two copies. The c.C280T transition in exon 7 of *SMN2* is translationally silent but causes the disruption of an exonic splicing enhancer (ESE) (Lorson et al. 1999; Cartegni and Krainer 2002) and additionally creates a new splicing silencer (Kashima and Manley 2003).
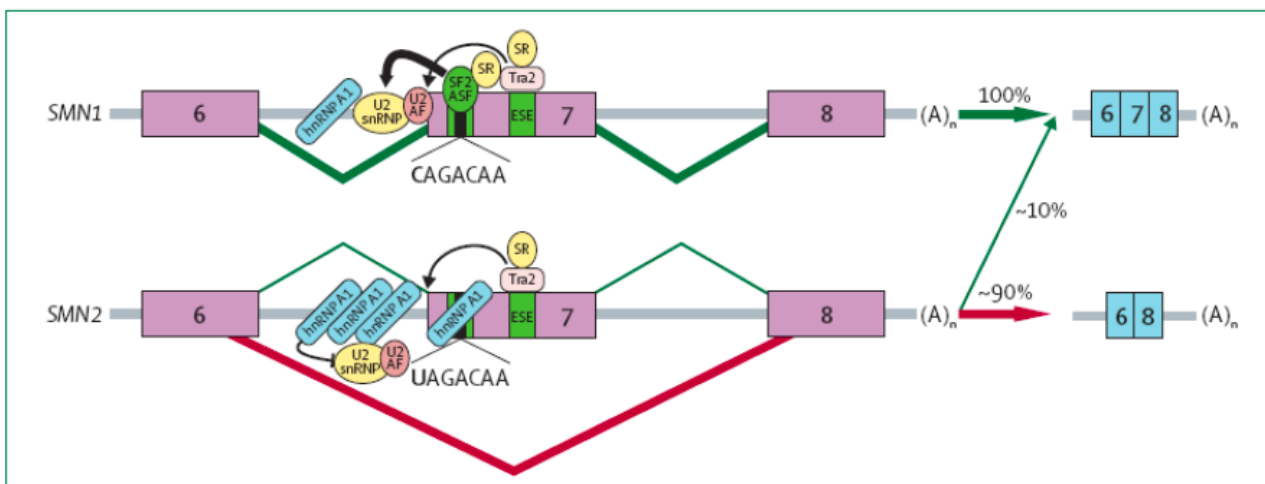
Figure 2: Pre-mRNA splicing of *SMN1* and *SMN2*. In *SMN1*, an exonic splicing enhancer (ESE) which contains the nucleotide cytosine (C) at position six in exon seven (Ex7+6), is recognized by splicing factor 2 or alternative splicing factor (SF2/ASF) which interacts (thick black arrow) with the U2 class of small nuclear ribonuclear protein (U2 snRNP) to remove intron six. Other splicing factors (e.g. SFRS10) determine splicing through interactions (thin black arrow) with ESE elements found centrally within exon seven. Serine and arginine (SR)-rich proteins might also exert a positive splicing effect. In SMN2, the ribonucleotide uridine (transcribed from thymidine) at Ex7+6 favours exon seven exclusion by binding to heterogeneous nuclear ribonuclear protein (hnRNP) A1; a negative splicing factor. Moreover, SF2/ASF no longer recognizes this sequence motif. Binding of hnRNP A1 is also believed to prohibit U2 snRNP binding to the branch point which results in about 90% of *SMN2* final mRNA transcripts with no exon seven. The positive splicing factors downstream (thin black arrow) are functioning and could account for exon 7 inclusion in about 10% of SMN2 transcripts. (taken from (Lunn and Wang 2008))

As a consequence, 90% of *SMN2* pre-mRNAs are alternatively spliced lacking exon 7. Only about 10% of *SMN2* mRNA transcripts are correctly spliced and encode a protein identical to that generated by the *SMN1* gene. Exon 7 skipping leads to a frameshift and an alternative stop codon in exon 8 (Figure 2), encoding for a truncated protein (Δ7SMN2) of reduced oligomerization capacity and stability (Lorson et al. 1998; Lorson and Androphy 2000). The truncation generates a degradation signal at the C-terminal part of the SMN protein, which leads to rapid degradation by the proteasome pathway (Cho and Dreyfuss 2010). A large genetic variability has been found concerning the number of repeat units (null to four) per chromosome, the size and orientation of this CNV, which can lead to rearrangements and *SMN2* copy numbers being variable among the population. Although a strong inverse correlation has been found between the number of *SMN2* copies and disease severity (Feldkotter et al. 2002), this correlation is not absolute, as the genetic integrity, splicing, transcription, translation and stability of the *SMN2* gene, RNA or protein can be influenced by various *cis* or *trans* or even exogenous factors (Wirth et al. 2013). In general, the more *SMN2* copies a patient has, the milder the phenotype. Most SMA type I patients carry two *SMN2* copies, SMA type II patients carry three *SMN2* copies, SMA type III patients carry three or four copies and SMA type IV usually carry up to six *SMN2* copies (Feldkotter et al. 2002; Wirth et al. 2006). The correlation between copy number of *SMN2* and the severity of the SMA phenotype in mouse and human is depicted in Figure 3. Noteworthy, there are the different requirements of FL-*SMN2* levels in humans and mice to fully compensate for the lack of *SMN1* and *Smn*, respectively. It has been shown that three copies of *SMN2* are enough to rescue the survival in the SMA mouse model, while in humans 6-8 *SMN2* copies compensate for the lack of *SMN1* gene (Michaud et al. 2010; Wirth et al. 2013). Interestingly, cases have been reported, in which patients develop a mild type III SMA despite having only 2 *SMN2* copies and vice versa, type I SMA patients have been identified carrying 3 *SMN2* copies (Feldkotter et al. 2002). They hypothesized that these unexpected correlation between *SMN2* copy numbers and phenotypic appearance might be due to modifying genes or other external factors, intragenic mutations within *SMN2*, or *SMN2* genes being partially deleted or duplicated. *SMN2* occurred during a recent evolutionary event during transition from primates to humans. The gene duplication event occurred for the first time in primates roughly five million years ago. However, also in man's closest relative *Pan troglodytes*, only two to seven copies of *SMN1* are present whereas the *SMN2* gene is unique to humans (Rochette et al. 2001) Since homozygous mutations in any species carrying a single copy cause early embryonic lethality (Schrank et al. 1997), *SMN2* and SMA are human-specific.
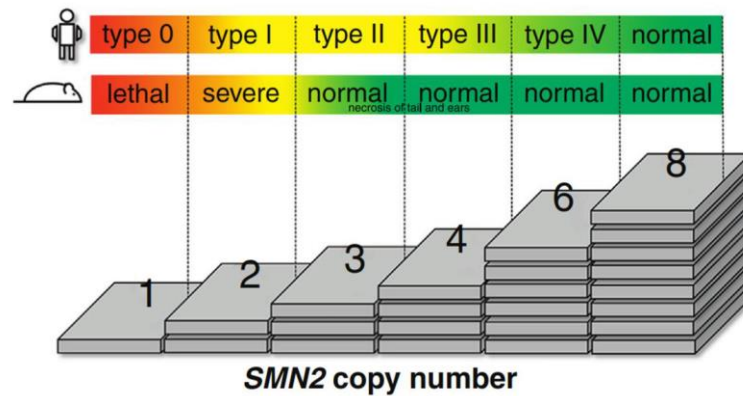
Figure 3: Different requirement of *SMN2* gene compensate the SMA phenotype in human and mouse. Since each *SMN2* produces 10% functional FL-SMN protein, more *SMN2* copies lead to a milder phenotype or complete rescue (Wirth et al. 2013). Note the different requirement of FL-*SMN2* levels in humans and mice to fully compensate for the lack of *SMN1* and *Smn*, respectively. In mice three instead of two *SMN2* copies lead to an almost normal phenotype. In humans only eight copies lead to a normal phenotype.

1.1.4 SMN protein

The human SMN protein is a 294 aa protein of about 38 kDa in size and ubiquitously expressed in all tissues, with highest levels present in the CNS and liver (Carvalho et al. 1999; Young et al. 2000; Young et al. 2001). Since SMN abundance markedly declines after birth, it is thought that elevated SMN levels may play an important role throughout prenatal development (Burlet et al. 1998). Inside the cell, SMN is present in both the cytoplasm and the nucleus. While in the cytoplasm it is diffusely distributed, distinct SMN foci are observed inside the nucleus (Burlet et al. 1998; Coovert et al. 1997; Liu and Dreyfuss 1996). These very bright dot-like structures in the nucleus termed gemini of Cajal bodies (CBs), or gems are often located in close proximity or overlap with CBs, which play an important role in RNA transcription and processing (Young et al. 2001; Schul et al. 1998; Lyon et al. 1997). Like the majority of cytoplasmic proteins, SMN is degraded via the ubiquitin-proteasome-system (UPS) (Burnett et al. 2009; Chang et al. 2004). The SMN protein consists of several functional domains. N-terminally, exon 2b and the beginning of exon three encode for an RNA-binding-domain (RBD) (Bertrandy et al. 1999), whereas the major part of exon 3 is spanned by a Tudor-domain, facilitating Sm protein binding during U snRNP biogenesis (Selenko et al. 2001). Exons 4 and 5 carry a proline-rich stretch, facilitating interaction with Profilins (Bowerman et al. 2009; Bowerman et al. 2007; Giesemann et al. 1999). In addition, the YG-box, encoded by exon 6 in conjunction with exon 2b (Lorson et al. 1998) is required for SMN self-oligomerization.

1.1.5 SMN function

Since the SMN protein possesses diverse functions in many different environments and subsequently in a plethora of cellular pathways and molecular mechanisms, its functions are categorized into a) housekeeping functions, b) neuron specific functions and c) muscle specific functions and briefly outlined in the following:

1.1.5.1 Housekeeping functions

Biogenesis of snRNPs

Small nuclear ribonucleoproteins (snRNPs) are actively participating within the splicing machinery of every cell. The role of the snRNPs is to recognize and remove introns from pre-mRNAs structures (Pellizzoni 2007). Members of the hnRNP family consists of small nuclear RNAs called U1 U2, U4 and U5, U11 and U12 and a protein part. The latter is made of a number of specific proteins that are unique for each snRNP and form a heptameric ring of Sm (Smith antigen) proteins (B/B', D1, D2, D3, E, F, and G) (Liu et al. 1997). This Sm ring is important for snRNP stability and function as well as for nuclear localization of snRNPs. The SMN complex facilitates addition of the Sm proteins onto the respective snRNA and catalyzes Sm ring closing (Lorson et al. 1998; Meister and Fischer 2002; Pellizzoni et al. 1999). SMN, GEMIN2–8 and UNR-interacting protein (UNRIP) together form the SMN complex (Gupta et al. 2015). The SMN protein unfolds its proper function only as an oligomer (Lorson et al. 1998; Pellizzoni et al. 1999). It has been shown to form higher-order complexes ranging from 20S to 80S. Several point mutations in *SMN1* have been shown to impair binding of SMN to the Sm proteins, thus leading to generalized splicing defects (Gabanella et al. 2007; Lorson et al. 1998; Pellizzoni 2007; Sun et al. 2005; Zhang et al. 2008).

Stress response

Exposure to stress factors such as heat, chemical compounds or UV irradiation activates a protective cellular process called stress response. While specific stress-induced genes e.g. the heat-shock-proteins (HSPs) are activated in response to stress, most other genes are silenced. During cell stress, mRNA transcripts are recruited and dynamically sorted into cytosolic compartments forming so called stress granules (SG) to protect mRNA transcripts from degradation or denaturation (Kedersha and Anderson 2009). SGs have been proven to serve as transient local storage compartment for mRNAs and only while recovering from stress exposure, SGs reassemble and mRNA transcripts are again available for further translation (Nover et al. 1989). Stress granules are formed by shuttling the RNA binding

proteins TIA-1(T-cell internal antigen-1) and TIA-R (TIA1-related protein) from the nucleus into the cytoplasm where these proteins self-aggregate and colocalize with poly (A) containing mRNA (Kedersha et al. 1999). However, it has been observed that SMN protein co-localizes and interacts with TIA-1 and TIAR, which accumulate in stress granules (Hua and Zhou 2004a, b). This finding suggests that SMN contributes to formation and function of SGs.

1.1.5.2   Neuron-specific functions

The modifying factor PLS3 positively influences axonal integrity and nerve connectivity in SMA mice at the level of the neuromuscular junction (Ackermann et al. 2013). Therefore, the particular focus of this chapter is on the function of SMN in axonal mRNA transport and translation, axonal growth, as well as NMJ maturation.

Axonal mRNA transport and translation

In the past, several different findings led to the assumption that SMN is involved in RNA transport along axons, as well as translational regulation. FMRP (Fragile mental retardation syndrome protein), which is crucial for mRNA transport and translation, was found to be a direct interactor of the SMN protein (Piazzon et al. 2008). Additionally, SMN granules that colocalize with RNAs were actively transported to the growth cones, indicating an involvement of SMN in axonal transport of mRNA and mRNA binding proteins (Zhang et al. 2003). Moreover, a reduction of ß-*Actin* mRNA at the growth cones of MNs derived from SMA mice and SMN-depleted PC12 cells, has been reported, additionally suggesting an involvement of SMN in mRNA transport along axons (Rossoll et al. 2003). hnRNP R, which controls ß-*Actin* localization (Rossoll et al. 2003) and directly interacts with the SMN protein, was found to be present at the presynapse of NMJs of pre- or neonatal mice, supporting a contribution of SMN beyond snRNP assembly (Dombert et al. 2014). Through live cell imaging it has been demonstrated that SMN granules traffic bidirectionally along neuronal compartments and to the growth cones of MNs (Zhang et al. 2006; Zhang et al. 2003). Taken together, these finding suggest that SMN is actively involved in recruitment and transport of axonal mRNAs along the axons and eventually to the axon terminals.

In the past it has already been discussed that SMN may have a specific function in regulating translation in neurons (Piazzon et al. 2008; Bardoni et al. 2001). Very recently it has been reported that in MNs derived from SMA mice SMN deficiency severely disrupts local protein synthesis within neuronal growth cones. These mice show reduced levels of cytoskeleton-associated growth-associated protein 43 (GAP43) mRNA and protein in axons and growth

cones. Most importantly, HuD and IMP1 overexpression, which are mRNA-binding proteins, restores GAP43 mRNA and protein levels in growth cones and rescues axon outgrowth defects in SMA neurons. These findings furthermore emphasize that SMN is an important player in the localization and local translation of mRNAs with important axonal functions (Fallini et al. 2016).

Neurite outgrowth

In previous studies, a novel, shorter isoform of SMN called aSMN (axonal SMN) has been identified, which was only found in axons of MNs. There it was found to trigger axonogenesis (Setola et al. 2007). Furthermore, SMN overexpression has been shown to induce neurite outgrowth and could rescue SMN knock-down effects in zebrafish and mice (Bowerman et al. 2009; Fan and Simard 2002; McWhorter et al. 2003; Oprea et al. 2008). Neurite outgrowth as well as neurite branching are both actin-dependent processes (Schmidt and Rathjen 2010). Reduction of the endogenous SMN altered the G-/F-actin ratio significantly, which further indicated SMN involvement in actin dynamics and microfilament metabolism in MN axons (van Bergeijk et al. 2007). The protective modifier PLS3 is an actin-bundling protein restoring disturbed G-/F-actin ratios in SMA patients (Oprea et al. 2008), as well as SMA mice (Ackermann et al. 2013). Therefore, the influence of actin on the MN integrity will be discussed in more detail in chapter 1.2.2. Furthermore, in zebrafish experiments the knock-down of Smn led to an earlier branching of axons, underlining the important role of Smn in motor axon-specific pathfinding and motor axon development (McWhorter et al. 2003).

Neuromuscular junction formation and maintenance (NMJ)

In fly, *Drosophila melanogaster*, developmental and motor behaviour deficits were observed due to reduced endplate currents and endplate disorganization (Chan et al. 2003). These findings led to the assumption of primary defects at the neuromuscular junction (NMJ) in SMA. NMJs are the connecting pieces between the axon terminal of a MN and the respective muscle. Histological inspection of SMA mice revealed that the maturation of NMJs was severely reduced and AChR (Acetylcholine Receptor) clusters did not form proper pretzel-like structures. Moreover, pre-terminal sprouting was also decreased (Kariya et al. 2008). Electrophysiological examinations showed that reduced SMN levels in mice indeed led to lower evoked endplate currents (EPC) due to reduced neurotransmitter release (Kong et al. 2009). Also in the vertebrate *Xenopus laevis*, motor neuron abnormalities with reduced axonal outgrowth and abnormal formation of branching extensions have been described (Ymlahi-Ouazzani et al. 2010). Severe SMA mice exhibit a significant reduction of axonal

inputs per endplate during synapse elimination process, also termed axonal pruning (Ackermann et al. 2013), in proximal TVA muscle (Murray et al. 2008). In addition, electrophysiological recordings of synaptic activity at the NMJ have shown a number of abnormalities in Smn depleted mice (Torres-Benito et al. 2011). Furthermore, also the distribution of vesicles in the presynapse appeared abnormal in SMA animals (Kariya et al. 2008). The functional defects observed in NMJs of SMA mice manifest also in altered morphological appearance of both pre- and postsynaptic structures. SMA presynapses occur with NF accumulations that participate in MN dysfunction, e.g. by slowing down the transport of components required for axonal and synaptic maturation and maintenance (Kariya et al. 2008; Kong et al. 2009; Ruiz et al. 2010; Torres-Benito et al. 2011). The defects observed at SMA postsynapses affect mainly the maturation process of Acetyl Choline receptor (AChR) clustering. While in wt oval AChR plaques are transformed into complex adult synapses with a so-called pretzel-like structure, SMA animals display small and still oval shaped endplates with almost no gutters of perforations and postsynaptic membrane folds fail to form (Torres-Benito et al. 2011; Sanes and Lichtman 1999). The NMJ pathology rather than axonal defects leads to characteristic disease features in SMA mice (Ackermann et al. 2013).

1.1.5.3   Peripheral organ-specific functions

Although SMA is primarily considered a neuromuscular disease mainly affecting the neuronal circuitry with NMJ pathology and loss of α-motor neurons, and only secondarily leading to muscles atrophy, a muscle specific role of SMN has also been discussed previously. After knock-down of *Smn* in C2C12 myoblast, severe defects in myoblast fusion and abnormal myotube morphology have been reported (Shafey et al. 2005). These defects are most likely due to Z-disc deficiency, as the entire SMN protein complex is localized to the sarcomeric Z-disc and SMN is a direct target of calpain-3-mediated proteolytic cleavage (Walker et al. 2008; Shafey et al. 2005).

Previous studies revealed that in absence of neuronal SMN, the muscle specific overexpression is not sufficient to improve the SMA phenotype in several SMA animal models. In contrary to that, neuron specific SMN expression alone significantly increased survival but did not completely rescue the SMA phenotype (Chan et al. 2003; Gavrilina et al. 2008). Therefore, the hypothesis that SMA might be caused by a muscle specific reduction of SMN was repelled.

As described in more detail in the following chapter, severely affected SMA mice die early as they do not only show defects within the neuronal circuitry and the affected muscle but also suffer from inner organ impairments such as heart, lung, liver and intestine (Schreml et al. 2013; Riessland et al. 2010; Shababi et al. 2014; Hayhurst et al. 2012; Shababi et al. 2012; Bevan et al. 2010; Heier et al. 2010; Butchbach et al. 2010; Bowerman et al. 2012b; Cifuentes-Diaz et al. 2001; Hua et al. 2011; Vitte et al. 2004). In consideration of our present work the so-called threshold theory may be of great importance. It suggests different susceptibility of certain cells to SMN depletion. When SMN amounts are only marginally reduced, MNs are already affected. As SMN levels further decrease or even completely vanish (Sleigh et al. 2011), heart, lung, liver, intestine and all other tissue types get affected eventually.

1.1.6 SMA mouse models

To investigate the pathomechanisms of SMA, many different SMA mouse models have been generated over the last two decades. In contrast to humans, where a second copy of *SMN1* is present, the *SMN1* orthologue in mouse, *Smn*, has been shown to exist as a single copy gene (DiDonato et al. 1999; DiDonato et al. 1997; Viollet et al. 1997). The homozygous knockout of *Smn* is embryonically lethal, indicating that Smn is indispensable throughout all cell types (Schrank et al. 1997; Hsieh-Li et al. 2000; Park et al. 2010). In the following, a variety of SMA mouse models will be presented. In 1997, the first classical knock-out of the murine *Smn* gene was described. The researches disrupted exons 2 - 4 of the *Smn* gene and reported an early embryonic lethality before implantation between day E2.5 and E3.5 (Schrank et al. 1997). In 2000, another group genetically replaced a 1.6 kb fragment of the *Smn* gene including exon 7 with a HPRT (hypoxanthine phosphoribosyl transferase) cassette and observed normally developing embryos at E3.5 but not at E6.5, indicating an essential role of Smn in the embryonic development (Hsieh-Li et al. 2000). Heterozygous $Smn^{KO/wt}$ mice showed no symptomatic muscle atrophy, but a ~50% reduction of the SMN protein level and a resulting degeneration of the α-motor neurons after 6 months of life (Jablonka et al. 2000). Due to the early embryonic lethality of homozygous knock-out mice, however, this SMA model was not useful to adequately study SMA pathomechanisms. For this reason and to more accurately mimic the human situation, the aberrantly spliced human *SMN2* (*hSMN2*) gene was introduced into the $Smn^{KO/KO}$ background as a genomic fragment (Hsieh-Li et al. 2000; Monani et al. 2000b; Park et al. 2010).

1.1.6.1   ‚Monani' SMA mouse model

Remarkably, already one or two copies of the *SMN2* transgene are sufficient to overcome the early embryonic lethality reported earlier. ‚Monani' SMA mice carry one copy of *hSMN2* per transgenic allele. Homozygous *Smn*^KO/KO;*hSMN2*^tg/tg mice (two *hSMN2* copies) are viable but develop severe symptoms including MN loss and motoric disability on P2 and die on P4 (Monani et al. 2000b). MNs were dramatically reduced during these first postnatal days and SMA animals dying so early resembled more or less a SMA type I. Similarly to humans, addition of more *SMN2* copies ameliorated the phenotype and eight *SMN2* copies resulted in a total rescue of these SMA mice, providing the first proof-of-concept study of the feasibility of modulating the *SMN2* gene for therapeutic purposes (Monani et al. 2000b; Park et al. 2010). Heterozygous *Smn*^KO/KO;*hSMN2*^tg/0 with a total of 1 *hSMN2* copy, however, are embryonically lethal. In addition, a mouse model resembling a milder form of SMA (SMA type III) is based on the already mentioned ‚Monani' SMA mouse model. A transgene carrying a missense (A2G) mutation in exon 1 of the *SMN* gene was introduced into the severe SMA genetic background. *Smn*^KO/KO;*SMN2*^tg/tg;*SMN*A2G^tg/0 mice exhibited many of the clinical and pathological characteristics of type III (mild) SMA (Monani et al. 2003). These mice suffer from MN degeneration, loss and sprouting, muscle atrophy, and abnormal EMG patterns.

1.1.6.2   Δ7 SMA mouse model

The most commonly used SMA model today is the so called SMNΔ7-mouse (Le et al. 2005). This line carries the Monani-*hSMN2* transgene (1 *hSMN2* copy per allele) and additionally *Δ7hSMN2 (a*n *SMN* cDNA lacking exon 7), each homozygously, on the *Smn* null background. In *Smn*^KO/KO;*hSMN2*^tg/tg;*Δ7hSMN2*^tg/tg mice a modest attenuation of the SMA phenotype was observed with a mean survival of 13.3 ± 0.3 days, demonstrating that also Δ7SMN2 is at least partially functional and does not, as was previously alleged, act deleterious through dominant-negative effects (Kerr et al. 2000; Le et al. 2005). This was an *in vivo* proof that the SMNΔ7-protein has the capability to associate with the SMN-protein and to stabilize the whole SMN-complex and that SMNΔ7 has no detrimental effect on the SMA animals (Le et al. 2005). Nonetheless, Δ7 SMA MNs show reduced proprioceptive reflexes that correlate with decreased number and function of synapses on MN somata and proximal dendrites (Mentis et al. 2011). Although the circuit and synaptic abnormalities that contribute to neurodegenerative diseases are complex, previous studies using the Δ7 SMA mouse model led to the following hypothesis: As primary afferents and motor neurons both

express SMN, it is possible that the phenotypes of sensory and motor neurons in SMA mice simply reflect cell-autonomous outcomes of SMN reduction (Mentis et al. 2011). Furthermore, the severe denervation in a series of head and trunk muscles in SMNΔ7 mice might compromise vital motor functions, which are clinically relevant to SMA patients (Ling et al. 2012).

1.1.6.3   Taiwanese SMA mouse model

In 2000, Hsieh-Li et al. generated another SMA mouse model, also termed Hung mice or Taiwanese SMA mice, by crossing an integrate of a BAC clone carrying 2 *hSMN2* copies onto the $Smn^{KO/KO}$ background. Several different founder lines were generated on a mixed background, exhibiting either a SMA type I, II or III phenotype. Heterozygous $Smn^{KO/KO};hSMN2^{tg/0}$ animals (2 *hSMN2* copies) show a background-dependent survival of ~10 (FVB/N, (Riessland et al. 2010)) to ~14 d (C57BL/6N, (Ackermann et al. 2013)) while homozygous mice of the genotype $Smn^{KO/KO};hSMN2^{tg/tg}$ (4 *hSMN2* copies) are fully viable and fertile but show necrosis of ears and tail. Previous studies revealed that the heterozygous $Smn^{KO/KO};hSMN2^{tg/0}$ animals (from here on called SMA mice) show a cardiac phenotype as well as dark red discolorations of the lungs compatible with atelectasis or pulmonary infarctions and the intestine appeared empty and string-like and opaque fluid was found in the abdomen of most late-stage SMA animals with histological changes in the small intestine consisted of reduced numbers of villi (Schreml et al. 2013). Some of the SMA mice showed so massive inner organ failure and therefore died unexpectedly early while apparently otherwise being in relatively good health and showing little or no motor deficits (Schreml et al. 2013). The Hung mouse model offers the big advantage of producing 50% of SMA and 50% of control mice within one litter. Since the Hung mouse model was used in this study to analyze the effect of *PLS3* overexpression on the intermediate SMA phenotype, this model including the breeding scheme for the production of SMA mice is described in chapter 4.1.2.

1.1.6.4 $Smn^{2B/KO}$ SMA mouse model

Furthermore, *Smn* exon 7 contains a critical AG-rich exonic splice enhancer sequence (ESE) analogous to the human ESE within *SMN* exon 7, and subtle mutations within the mESE caused a variation in *Smn* transcript levels. Specific mutations at the endogenous *Smn* locus lay the foundation for developing SMA animals that closely 'resemble' SMA patients (DiDonato et al. 2001). The $Smn^{2B/KO}$ mouse line, obtains a 3 bp substitution in the exon 7 exonic splicing enhancer (ESE) (Bowerman et al. 2009). With about 15% normal

level of SMN protein, $Smn^{2B/KO}$ mice display significant reduction in body weight, abnormalities in locomotion and gait, and a significant reduction in the number of MN cell bodies and axonal loss. These mice are phenotype-free until P10 with a median life expectancy of 28 days. They show neuromuscular junction (NMJ) pathology with an inter-muscular differential vulnerability and an association between pre- and post-synaptic defects (Bowerman et al. 2012a). The $Smn^{2B/KO}$ mice also display the SMA pathological hallmark of motor neuron loss in the brain stem and ventral horn region of the lumbar spinal cord (L1–L2). $Smn^{2B/2B}$ mice are phenotypically normal (Bowerman et al. 2012a).

1.1.6.5   Burgheron mouse model of SMA type II/III

In 2015, an intermediate SMA mouse model was generated that, in contrast to the intermediate $Smn^{2B/KO}$ SMA mouse model, contains the human *SMN2* transgene (Bogdanik et al. 2015). The mutants are compound heterozygous for the *Smn1^{tm1/Msd}* knockout of Smn (Schrank et al. 1997) and the *Smn1^{tm5}* allele (C-allele, made by Regeneron Pharmaceuticals) and carry a single copy of the human *SMN2^{89Ahmb}* transgene. This *SMN2* transgene consists of a 35.5-kb BamHI genomic fragment encoding the human *SMN2* promoter and gene (Monani et al. 2000b). The C-allele is a hybrid gene that contains a replacement of exon 7 and 8 from the mouse *Smn* locus by exons 7 and 8 of the human *SMN2* gene (1.3-kb fragment), and a full 42-kb copy of the human *SMN2* gene. The Burgheron mutants have a mean survival of 89 days and present with a cardiac phenotype as well as tail, limb and ear necrosis. They show a delay in the structural maturation of the NMJ. In most severe SMA models and type I and II SMA patients, peripheral axon loss has been observed, whereas in Burgheron mutants denervation and abnormal accumulation of neurofilament proteins in the nerve terminals did not occur.

1.1.7 Therapeutic strategies in SMA treatment

In the past, a lot of effort has been done to develop different therapy strategies to target SMA. Although a lot of knowledge has been gained through developing promising drug candidates, there is still no cure available for SMA. Since still around 10% of FL-*SMN* transcript are produced by *SMN2*, compounds, which target its transcription, seem to be promising drug candidates. Histone deacetylase inhibitors (HDACi) block the activity of histone deacetylases (HDAC) as they shift their modification to the acetylated state and thereby activating gene transcription. In SMA mouse models or cell culture experiments, HDACi such as Sodium butyrate, valproic acid (VPA), phenylbutyrate, Trichostatin A,

suberoylanilide hydroxamic acid (SAHA), M344 and LBH589 had been successfully tested to stimulate the *SMN2* transcription (Chang et al. 2001; Brichta et al. 2003; Sumner et al. 2003; Andreassi et al. 2004; Brahe et al. 2005; Brichta et al. 2006; Riessland et al. 2006; Avila et al. 2007; Tsai et al. 2008; Garbes et al. 2009; Hauke et al. 2009).

Additionally, instead of activating gene transcription another idea to increase SMN levels in SMA patients might be to stabilize remaining FL-SMN protein. Previous studies revealed that SMN is degraded via the ubiquitin/proteasome pathway (Chang et al. 2004; Garbes et al. 2009). Therefore, proteasome inhibitors might be an additional promising strategy to treat SMA. When tested in cell culture experiments, the proteasome inhibitor MG132 led to an increase in SMN protein.

Moreover, when neural stem cells had been transplanted into the spinal cord of Δ7 SMN mice, they differentiated not only into MN-like cells but also protected host MNs from degeneration. This stem cell therapy significantly increased survival and improved motoric abilities of these animals (Corti et al. 2010). Hence, stem cell therapy has a promising potential as a treatment strategy counteracting SMA pathology. The greatest challenge of this treatment form is to ensure that transplanted MNs will grow into the respective target muscle tissue. Therefore, it is inevitable to use neuroprotective compounds such as brain-derived neurotrophic factor (BDNF), neurotrophin-3 (NT3), neurotrophin-4/5 (NT4/5) and nerve growth factor (NGF) that are added to the donor cells (Ebert et al. 2009; Wyatt and Keirstead 2010; Corti et al. 2010).

Over the last five years, gene therapy as an additional strategy to target SMA, has been tested in mice. In three independent studies, researchers used the self-complementary adeno-associated virus 9 (scAAV9) for gene delivery into MNs of SMA mice by intravenous injection (Foust et al. 2010; Valori et al. 2010; Dominguez et al. 2011). In 2013, intramuscular scAAV9-SMN injection was successfully performed, mediating widespread gene delivery to the spinal cord and decreasing disease severity in SMA mice. The survival rate of these mice increased from 12 to 163 days (Benkhelifa-Ziyyat et al. 2013). Most strikingly, scAAV9-SMN was able to cross the blood brain barrier (BBB), highly efficiently transduced MNs in the lumbar region of the spinal cord as well as muscle tissue.

Last but not least, outstanding progress has been achieved in the development of using antisense oligonucleotides (ASOs) and morpholinos (Lim and Hertel 2001; Cartegni and Krainer 2003; Dickson et al. 2008). This strategy aims at the correction of the *SMN2* splicing pattern towards increased levels of FL-*SMN* transcripts. Elevating SMN levels in cell culture

and even when ASOs are injected into the brain of SMA mice (Passini et al. 2011; Hua et al. 2010; Hosseinibarkooie et al. 2016), delivery into the human CNS remains challenging and further clinical trials are indispensable to transfer our gained knowledge from animal models to the human SMA patient. As the ASO strategy is used in this study to establish an intermediate SMA mouse model some further information about the chemical structure and the mode of action of ASOs are highlighted in the following. Figure 4 depicts a variety of nucleotide analogues used in ASO drugs (Rigo et al. 2012).
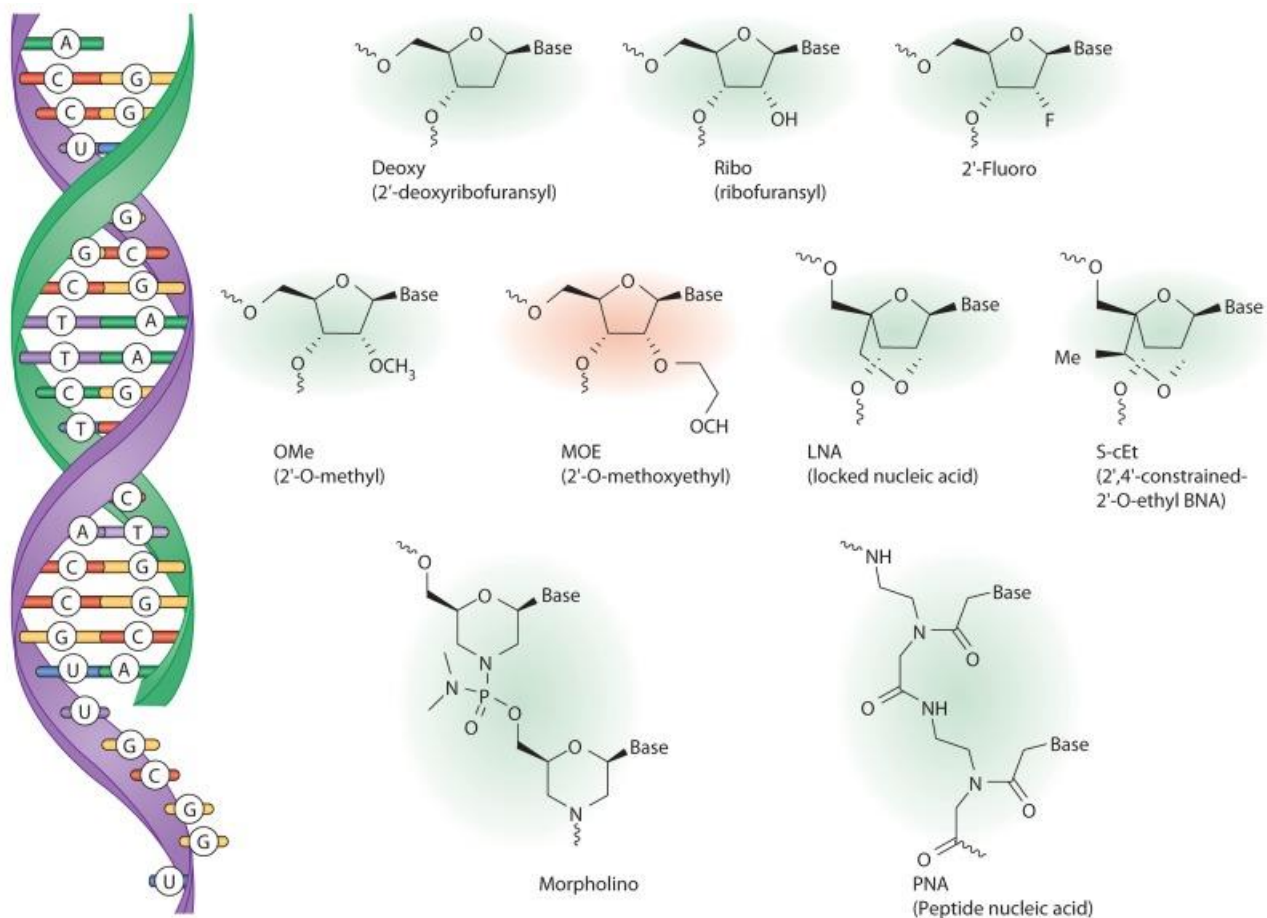
Figure 4: Nucleotide analogues used in antisense oligonucleotide drugs. Antisense oligonucleotides (green) bind to the target RNA (purple) by Watson-Crick base pairing (left). Chemical structures of various nucleotides or nucleotide analogues commonly used in antisense drugs are shown. The antisense oligonucleotide developed by (Rigo et al. 2012) to improve *SMN2* splicing has the 2′-MOE modification (red). Taken from (Rigo et al. 2012).

ASOs bind to RNA through Watson-Crick base paring (Figure 4). Once bound to the target RNA, there are multiple mechanisms by which antisense-based drugs alter its function, including promoting its degradation, interfering with pre-mRNA processing, blocking access to the RNA of specific proteins such as RNA-binding proteins and ribosome subunits, and

disrupting the secondary and tertiary structure of the RNA (Bennett and Swayze 2010). The mechanism by which an ASO elicits these effects is dependent upon the class of RNA, where on the RNA the ASO binds, and the chemical composition of the ASO.
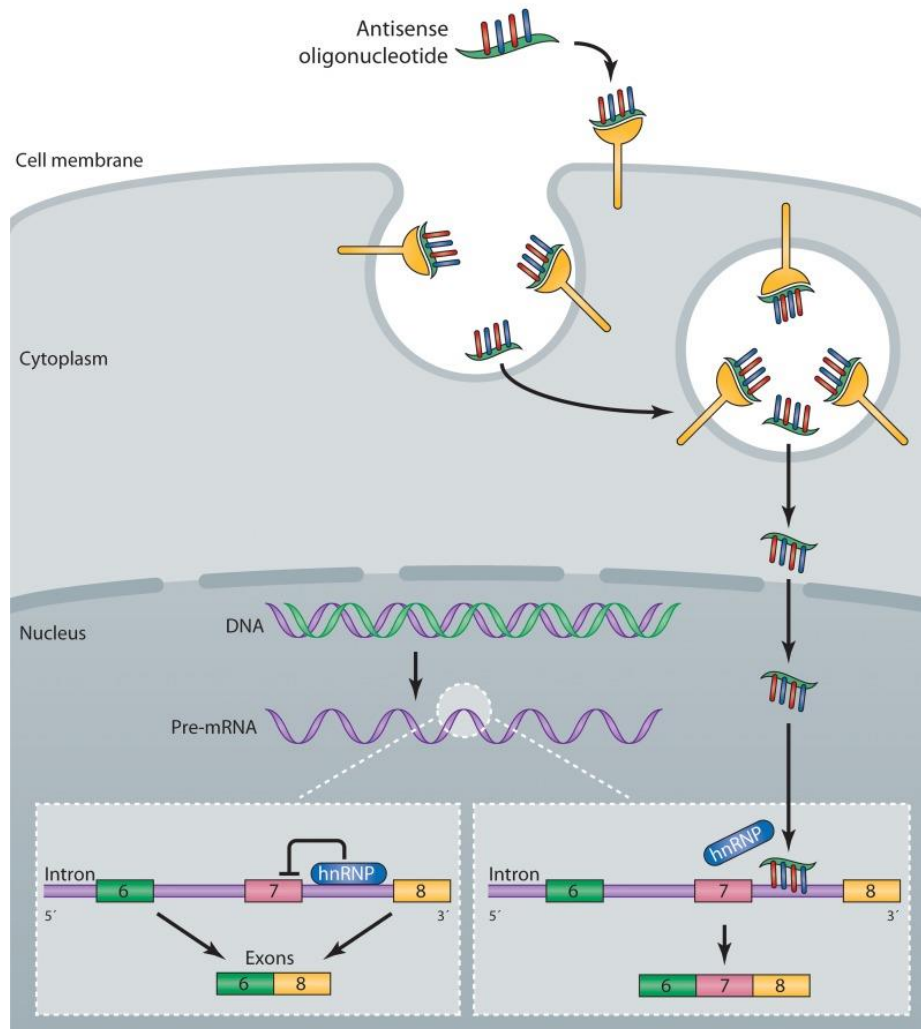
Figure 5: Mechanism of action of an antisense drug that modulates *SMN2* splicing. Single-stranded antisense oligonucleotides (ASO) are taken up into cells by an endocytic process via interaction with proteins expressed on the surface of cells (Koller et al. 2011). The ASOs escape the endosome and enter the nucleus, where they bind to the *SMN2* pre-mRNA. Binding of the ASO to the RNA displaces an hnRNP protein that normally represses splicing of exon 7, resulting in the production of a mature mRNA that includes exon 7, which is translated into the full-length *SMN* protein (Rigo et al. 2012). (Taken from (Rigo et al. 2012).)

The mechanism(s) by which ASOs enter cells include at least two endocytic uptake mechanisms (Figure 5; (Koller et al. 2011; Geary et al. 2009), but overall remains poorly understood. Binding of the ASO to the RNA displaces an hnRNP protein that normally represses splicing of exon 7, resulting in the production of a mature mRNA that includes exon 7, which is translated into the full-length SMN protein (Rigo et al. 2012).

Over the last decade, several groups tried to optimize the efficacy of ASO-treatments in order to make it more applicable and attractive for use in SMA therapy. Therefore, certain parameters needed to be taken in consideration: structure of the ASO drug molecule, delivery to the CNS by crossing the blood-brain barrier (BBB), and especially in mouse pre-clinical studies overcoming the known difficulties of multi-organ failure and diminishing tail and ear necrosis of the severely affected and most commonly used Δ7 and Taiwanese SMA mouse models (see also chapter 1.1.6). To achieve this, ASOs that block ISS-N1 (an intron 7 intronic splicing silencer in the human *SMN1/2* genes) and strongly enhance *SMN2* exon 7 inclusion in cultured patient fibroblasts (Singh et al. 2006) were systematically analyzed in cell-free splicing and in cultured cells (Hua et al. 2007; Hua et al. 2008). In 2009, a 2′-*O*-methyl (2′-OMe) phosphorothioate ASO (Figure 4) targeting ISS-N1 was directly delivered into the CNS by repeated neonatal intracerebroventricular (ICV) injections in the Δ7 SMA mouse model (Williams et al. 2009). They reported a small increase in SMN protein and full-length (FL) *SMN2* mRNA in the spinal cord, as well as improvements in weight gain and the righting response. However, only one dosing regimen was tested, an effect on survival was not assessed, and several ASO-treated and control mice died prematurely (Williams et al. 2009).

The lead ASO (2′-*O*-(2-methoxyethyl) (MOE) ASO (#10–27), Figure 4) promotes efficient *SMN2* exon 7 inclusion in the liver and kidneys of transgenic mice after systemic administration, but not in the spinal cord (Hua et al. 2008) owing to a lack of distribution across an intact BBB (Geary et al. 2003). Via ICV infusion in the CNS of adult type III SMA mice (Hsieh-Li et al. 2000) this MOE ASO had been characterized. In this study, they improved survival issues in mice with very short life spans, facilitated accurate measurements of mRNA splicing as well as long-term efficacy and metabolism of the ASO (Hua et al. 2010). The ASO promoted very efficiently expression of FL-*SMN2* mRNA and protein in the spinal cord, including MNs. Remarkably, the effect persisted for several months after ICV infusion for only seven days. Validation of the mechanism of action as well as pharmacokinetic and pharmacodynamic profiles of the ASO allowed them to test its therapeutic efficacy by using a single embryonic or neonate ICV injection in the mild SMA mouse model (Hua et al. 2010) and thereby showed that the ASO can successfully rescue the distal tissue necrosis phenotype in the type III mouse model. This demonstrates that this MOE ASO is a promising drug candidate for SMA therapy. Additional findings of these group revealed that ASO only delivered into the CNS, efficiently corrected *SMN2* exon 7 splicing in the spinal cord and led to a striking increase in SMN protein levels, but modestly extended

the median survival to 16 days, with a single pup surviving for one month (Hua et al. 2011). In marked contrast, systemic treatment with two subcutaneous injections resulted in a median survival of 108 days. Combining ICV and subcutaneous ASO injections further increased the median survival to 173 days; and additional subcutaneous injections at P5-P7, after the initial subcutaneous injections at P0-P3, extended the median survival to 137 days (Figure 6 and (Hua et al. 2011)). For the present study, we used these findings as a starting point for dosage optimization of the SMN-ASO to successfully generate an intermediate SMA mouse model by subcutaneously injecting suboptimal doses (10 – 50 µg) of this MOE SMN-ASO (see also 5.3).
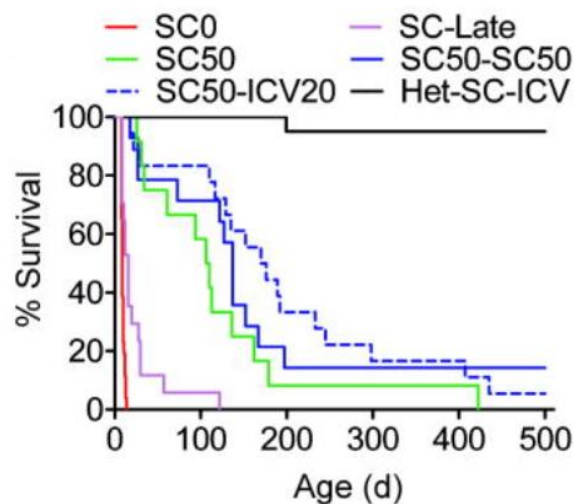
Figure 6: Systemic versus ICV ASO-10-27 injections in SMA mice. Survival curves after SC administration with saline (SC0, *n*=26) or ASO (SC50, *n*=12) twice between P0 and P3. SC50-SC50 (*n*=14) mice received two additional SC injections at P5-P7. Het-SC-ICV (*n*=13) and SC50-ICV20 (*n*=18) were heterozygous and SMA mice, respectively, that received combined P1 ICV and P0-P3 SC injections. Each SC injection dose was 50 µg/g. *P*<0.0001 for all groups versus SC0. *P*<0.0001 for all groups versus SC0. (Modified from (Hua et al. 2011).)

1.2   DEVELOPMENT OF THE NEUROMUSCULAR SYSTEM

As briefly mentioned in section 1.1.5.2, the neuromuscular junction (NMJ) is the connection between axon and muscle. The communication between nerve and muscle is ensured through neurotransmitter release from the presynaptic nerve terminal and receptor mediated signal transduction at the postsynapse. The most striking disease features in SMA mice are malformation and dysfunction of the NMJ. These defects are then followed by MN loss in the ventral horns of the spinal cord (Kariya et al. 2008; Kong et al. 2009). It has been reported that severely affected Taiwanese mice displayed no MN loss before P8 (Fayzullina

and Martin 2016). Nonetheless, as there is also evidence of MN loss starting at P4 in very severely affected Δ7 SMA mice (Mentis et al. 2011; Le et al. 2005), it still remains unclear whether this 'dying-back mechanism' should be considered as the only mechanism in SMA pathology or whether MN loss can proceed or occur in parallel to NMJ pathology. In SMA pathology, NMJ abnormalities include both pre- and postsynaptic alterations. Among these are abnormal neurofilament (NF) accumulation in the presynaptic nerve terminals, pronounced axon routing and arborization deficits (Rajendra et al. 2007), decreased amount of neurotransmitter released per action potential (quantum content, QC), reduced postsynaptic size with immature plaque-like AChRs (Kariya et al. 2008) and reduced post-synaptic currents (Torres-Benito et al. 2012). Therefore, an overview about fundamental processes driving axon growth and specification (axonal pruning) as well as NMJ development and refinement will be given below.

1.2.1 Axonal pruning and NMJ refinement

A delay of axon withdrawal from the NMJ during the process of axonal pruning in a PLS3 overexpressing SMA mouse has been described by (Ackermann et al. 2013). The underlying mechanism of this developmental process is briefly summarized below. Axonal pruning is a mechanism to selectively remove exuberant neuronal branches and connections during developmental stages of the nervous system to ensure structural of functional properties of the neuronal circuitry (Low and Cheng 2006). During NMJ development, numerous nerve terminals innervate individual AChR clusters. For proper axonal pruning, all but one presynaptic connection are removed, until every endplate gets innervated by only one single motor nerve ending (Lichtman and Colman 2000). There are two possible mechanisms, which have been described previously, to explain the process of axonal pruning. One of them is the so-called axon retraction, in which axonal contents are believed to be shuttled to other axon branches but so far, it has never been reported to occur at the neuromuscular junction (Bishop et al. 2004). Interestingly, NMJs in neonatal mice showing signs of abnormal ultrastructure were observed during the period of synapse elimination (Rosenthal and Taraskevich 1977). The second possible process is the classical Wallerian-type degeneration. During this kind of mechanism the entire axon arbor is removed rather than a subset of axons, which also has not been observed at the NMJ. Another concept of this process is termed axosome shedding (Bishop et al. 2004), in which axons are retreated and leave behind dismantled bulbs at their tips, which get removed as they get subdivided into

smaller remnants, termed axosomes. Previous findings of Schwann cells, which incorporated axosome material, support the idea of axosome shedding as they actively drive axonal recycling (Bishop et al. 2004). Nonetheless, on molecular level the process of axonal pruning is still poorly understood and further investigations are inevitable (Vanderhaeghen and Cheng 2010).

1.2.2 Influence of Actin on the Motor Neuron Integrity

Neurotransmitter release at the presynaptic terminals is a very complex process controlled by cytoskeletal dynamics. The actin cytoskeleton is important for cell shape, movement, signalling and transport of molecules into the cell (Blanchoin et al. 2014). Within the neuronal circuitry actin is involved in transport of synaptic vesicles (SVs) towards the active zone, as well as endocytic and exocytic pathways within the synapse. Overexpression of PLS3 – an actin-binding and -bundling protein – results in increased presynaptic nerve arborization and AChR clustering at the NMJ. Furthermore, PLS3 delays axonal pruning, indicating that PLS3 positively influences the axonal integrity (Ackermann et al. 2013). As PLS3 has an actin-binding and -bundling function, it is highly interesting to understand the connection between actin and the MN integrity, which in turn also highlights some of the physiological improvements of our mouse model (5.3 and 5.4).

Growth cones are the starting points of axonal outgrows. Actin polymerization is the main trigger for axonal outgrowth at the growth cones. Cofilin, which is also present at the growth cones has an actin destabilizing effect, as it localizes to the pointed (-) end of actin filaments, thereby depolymerizing actin (Pak et al. 2008). Previous studies have demonstrated, that axonal outgrowth is strongly dependent on the condensation state of the actin cytoskeleton at the growth cones. Indeed, less condensed actin supports axonal outgrowth (Bradke and Dotti 1999; Kunda et al. 2001). As already mentioned above (1.1.5.2), *β-actin* mRNA has been shown to be decreased in the growth cones of MNs derived from SMA mice and SMN-depleted PC12 cells (Rossoll et al. 2003). This indicates that the amount of actin molecules is significantly decreased in SMA growth cones, which are moreover significantly smaller compared to controls. Additionally, the connection between actin filaments, which can be mediated by additional proteins through actin-binding and -bundling abilities, can be important for cytoskeleton dynamics and thus for axonal growth. Besides the actin- bundling protein PLS3, there are several additional bundling proteins that are located in the growth cones including α-actinin, fascin, CamKII, Myosin, AbLIM, Filamin (Oprea et al. 2008; Dent

and Gertler 2003; Letourneau and Shattuck 1989; Okamoto et al. 2007). Therefore, the actin cytoskeleton and its network are fundamental for axonal outgrowth and maintenance.

1.3   PLS3 – A FULLY PROTECTIVE MODIFIER OF SMA

Phenotypical variability among patients with genetically caused diseases is very common. Extrinsic as well as intrinsic genetic factors might influence the severity of the genetic disease. Genetic modifying genes can have a huge impact on the outcome of the disease phenotype. Therefore, they also offer a great possibility to investigate and understand pathomechanisms of genetic diseases in more detail by analyzing common downstream pathways of the disease-causing gene and the modifier. For a long time, *SMN2* was the only known SMA-modifying gene with a strongly inverse correlation of *SMN2* copy number and SMA severity (Feldkotter et al. 2002). In most SMA families, high similarities were observed between the siblings with the same homozygous *SMN1*-deletion and identical *SMN2* copy number (Feldkotter et al. 2002; Rudnik-Schöneborn et al. 1994). However, so-called discordant families (Figure 7) with individuals having a homozygous deletion of *SMN1* have been reported to be completely healthy, whereas members of the same family carrying the identical genotype show SMA symptoms according to the *SMN2* copy number (Brahe et al. 1995; Cobben et al. 1995; Hahnen et al. 1995; Wang et al. 1996). Therefore, it has been speculated that other modifying factors might compensate for the loss of *SMN1* in unaffected siblings (Helmken and Wirth 2000; Helmken et al. 2003).

The actin-filament-bundling protein PLS3 was identified as the first *SMN*-independent SMA modifying protein besides SMN2 in a total of seven discordant families (Oprea et al. 2008; Heesen et al. 2016). By using transcriptome-wide differential gene expression analysis, PLS3, which is also named T-plastin, fimbrin or plastin 3 (Lin et al. 1988), was identified within these discordant families in nine fully asymptomatic females with homozygous deletion of *SMN1* and an identical number of *SMN2* copies as their affected siblings (mostly 3 – 4, reflecting SMA type III). This analysis was carried out with RNA from lymphoblastoid cell lines (Oprea et al. 2008).
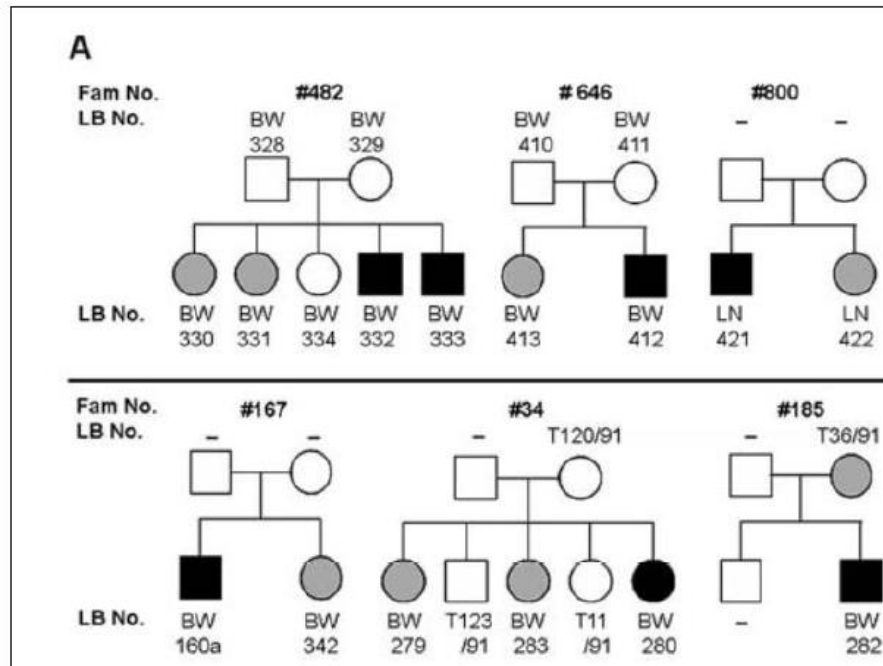
Figure 7: PLS3 overexpression in discordant families. Six discordant families in which PLS3 were shown to be upregulated at RNA and protein levels. PLS3 shows a sex dependent SMA rescue in these families. (Taken from (Oprea et al. 2008).)

PLS3 comprises of 16 exons and produces three mRNA transcript variants. Splice variants 1 and 2 encode for exactly the same 1893 bp transcript. Splice variant 3, uses a different in-frame splice site in the coding region, producing a transcript of 1812 bp in size. Besides PLS3, the human homologous genes L-plastin (PLS1) and I-plastin (PLS2) exist, which are located on chromosomes 3 and 13, respectively (Lin et al. 1993a; Lin et al. 1993b; Lin et al. 1994). All plastins are highly conserved from lower eukaryotes to humans, reflecting their importance in every cell type (Delanote et al. 2005). It has been revealed by pull-down experiment that SMN and PLS3 proteins do not show a direct interaction. This led to the conclusion that PLS3 does not exert its rescuing effect through the SMN protein but rather a downstream effect influencing the stabilization of the actin cytoskeleton in axons (Oprea et al. 2008).

The fact that all asymptomatic *SMN1*-deleted individuals were women might be explained by the location of *PLS3* on the X-chromosome (Xq23), making an incomplete X-inactivation a possible mechanism behind the PLS3 upregulation. Surprisingly, a few independent male SMA patients in this study revealed a similarly high PLS3 expression compared with the asymptomatic women but failed to be protected (Oprea et al. 2008). However, the location

of the *PLS3* gene on the X-chromosome and its gender specific rescuing effect suggest a possible hormone related regulatory mechanism. PLS3 was found to be overexpressed in asymptomatic *SMN1*-deleted individuals only in blood but not in fibroblasts, which suggests a tissue-specific regulation. Moreover, generation of induced pluripotent stem cells (IPSCs) from fibroblast cell lines allowed the differentiation into MNs and thus the analysis of PLS3 expression in the target cell type (Heesen et al. 2016). In cultures of these differentiated MNs, SMA III and asymptomatic siblings exhibited slightly higher but insignificant elevated SMN expression than control levels. This data excludes SMN levels as the reason for SMA protection in asymptomatic siblings. In contrast, PLS3 was significantly upregulated in mixed MN cultures from asymptomatic individuals pinpointing a tissue-specific regulation. Interestingly, PLS3 is abundant in growth cones of asymptomatic MN cultures as compared to SMA III siblings and controls. This implies an important role of PLS3 in neuromuscular synapse formation and maintenance and underlines the role of PLS3 as genuine protective modifier in SMA.

PLS3 is highly expressed in fetal and adult human spinal cord, as well as brain and muscle. Most strikingly, PLS3 overexpression led to a full rescue of axon defects in smn depleted zebrafish (*Danio rerio*) embryos (Oprea et al. 2008). In another study, behavioural analysis in smn mutant fish showed a reduced spontaneous swimming and truing. The transgenic overexpression of PLS3 in MNs was able to rescue the neuromuscular defect and corresponding movement phenotype in smn mutant fish (Hao le et al. 2012). Rescuing experiments with different parts of the PLS3 protein indicate that the Ca^{2+}-binding EF hand domain of PLS3 is able to rescue axonal phenotype in smn mutant fish ((Lyon et al. 2014) and Figure 8).

To further investigate the influence of the PLS3 overexpression on the SMA phenotype in the mammalian system, a conditional PLS3 overexpressing mouse model was generated (Ackermann et al. 2013). In these PLS3 transgenic SMA mice the motor axon inputs at the NMJ were significantly increased compared to endplates in SMA mice, which are only poorly or not at all innervated. During the process of axonal pruning, exuberant neuronal branches are removed and endplates become innervated by a single axon. Delayed axonal pruning in the PLS3 overexpressing mice finally leads to prolonged poly-innervation of endplates and maturation of NMJs. PLS3 overexpression improves neuromuscular connectivity as well as neurotransmitter release at the NMJ (Ackermann et al. 2013). Furthermore, PLS3 overexpression restores the disturbed F-Actin amount and the synaptic vesicle organization

in SMA mice (Ackermann et al. 2013). Despite all these improvements, PLS3 overexpression did not have a strong influence on the survival of these severely affected SMA mice, which can be due to multi-organ dysfunctions in this SMA mouse model (Ackermann et al. 2013; Schreml et al. 2013). Therefore, in the present study, we will focus on diminishing these inner organ defects and mimicking the situation of the asymptomatic *SMN1*-deleted individuals, to finally show the unrestricted PLS3 rescuing effect as described in chapter 2.

1.3.1 PLS3 protein

The PLS3 protein consists of 630 amino acids and is approximately 70 kDa in size. N-terminally and as already mentioned, PLS3 contains a calcium-binding domain consisting of a pair of EF hands with a helix-loop-helix structure. Additionally, it possesses a pair of actin binding domains (ABDs) composed out of two calponin homology (CH) domains (Figure 8) (Matsudaira 1994), which are located at the C-terminus.
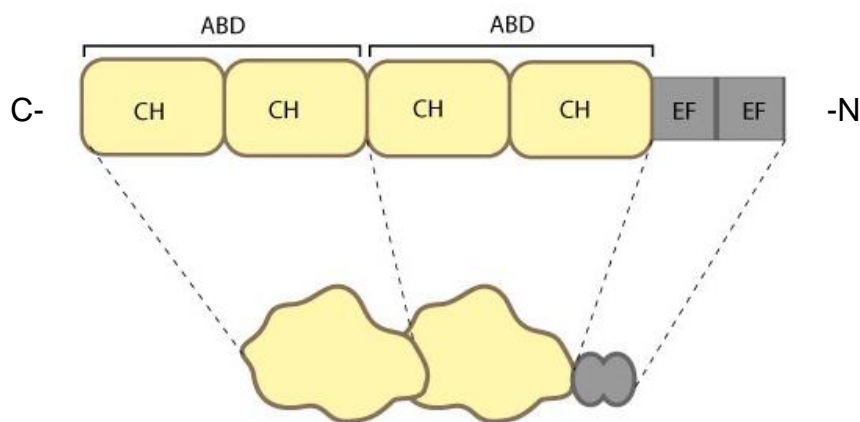
Figure 8: PLS3 protein structure: The 630 aa long protein has two N-terminal EF-hand domains followed by two actin binding domains (ABD1 and ABD2), each consisting of two calponin homology domains.

The EF-hand domain structure has high similarity with a spread thumb and forefinger of a hand. Calcium ions are coordinated by ligands within the loop and binding of Ca^{2+} to this motif might regulate PLS3 activity in actin bundling (Hanein et al. 1998). Ca^{2+} thereby acts as a negative regulator for PLS3 to interact with actin. Another study, using cryo-electron microscopy (EM) revealed the interaction of F-actin with the ABD2 domain of PLS2 (Galkin et al. 2008). Interestingly, PLS3 was found to interact with ataxin-2 (ATX2), suggesting a

possible role in regulation of RNA metabolism and translation. Noteworthy, ATX2 is known to interact with cytoplasmic poly(A)-binding protein (PABP), which is involved in translation initiation and mRNA decay regulation, as well as forming parts of stress granules (Ralser et al. 2005a).Overexpression of ATX2 increases PLS3 levels specifically in comparison to other plastins (Ralser et al. 2005b).

1.4 ENDOCYTOSIS – AN AFFECTED MECHANISM IN SMA

Because PLS3 knockout in yeast impairs endocytosis (Kubler and Riezman 1993), we hypothesized that disturbed endocytosis might be a key cellular mechanism underlying impaired neurotransmission and neuromuscular junction maintenance in SMA. Our recently published data as well as analyses done in the present study (see also chapter 5.13) demonstrate very nicely (*in vitro* and *in vivo)* how the process of endocytosis is disturbed in SMA (Hosseinibarkooie et al. 2016). As endocytosis is deeply connected to signalling, cell dynamics, growth, regulation, and defence, endocytic processes are linked to almost all aspects of cell life and disease. To better understand this very complex process and its regulations, an overview about endocytic pathways is given in the following. Endocytosis is the general term for energy-dependent internalization of fluid, solutes, macromolecules, plasma membrane components, and particles by the invagination of the plasma membrane and the formation of vesicles and vacuoles through membrane fission. By sorting, processing, recycling, storing, activating, silencing, and degrading incoming substances and receptors, endosomes are responsible for regulation and fine-tuning of numerous pathways in the cell (Huotari and Helenius 2011). Chemical synaptic transmission is mediated by neurotransmitters that are released by Ca^{2+}-triggered synaptic vesicle exocytosis (Deak et al. 2009). As many of the NSF attachment proteins (SNAPs) and SNAP receptors (SNAREs) are involved in both, endocytic and exocytic processes, the whole cycle should be considered as disturbed in SMA and further investigations are necessary to better understand the fine-tuning between those two processes. Interestingly, in this context is the role of Munc18-1-SNARE complexes that may create a central event in the priming reaction that makes docked synaptic vesicles readily releasable (Deak et al. 2009). To better understand the connecting mechanisms, Figure 9 illustrates several types of pathways by which nanoparticles can enter (endocytosis) and exit (exocytosis) the cell. The endocytosis pathways are classified into clathrin- and caveolae-mediated endocytosis, phagocytosis, macropinocytosis, and pinocytosis. Many types of cells use the clathrin- and caveolae-

mediated endocytosis pathways to internalize nanoscale materials, including viruses and nanoparticles (Pelkmans et al. 2001; Wang et al. 2009). Most importantly, nanoparticles are internalized by direct coating with the plasma proteins when exposed to physiological solutions. The phagocytosis pathway is used when phagocytic cells internalize foreign materials with sizes larger than 0.5 µm (Young 2006). The phagocytosis pathway is actin-dependent and restricted to specific phagocytes, such as macrophages, dendritic cells, and neutrophils. The macropinocytosis pathway is a non-specific process to internalize fluids and particles together into the cell, whereas the pinocytosis pathway absorbs biological fluids from the external environment of a cell (Geiser 2010). These pathways are very important to translocate single nanoparticles with sizes below 10 nm into the cell. The exocytosis pathways are classified into lysosome secretion, vesicle-related secretion, and non-vesicle-related secretion (Oh and Park 2014).
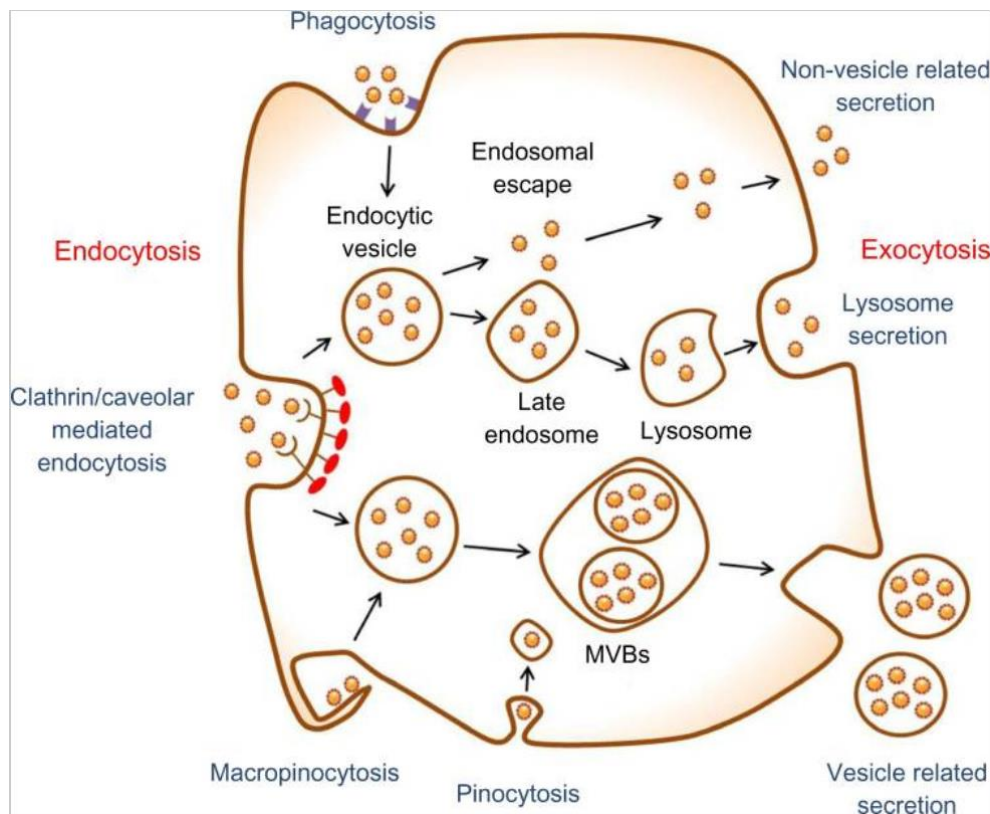
Figure 9: Schematic of endocytosis and exocytosis patterns of nanoparticles. Nanoparticles enter the cell via four types of pathway: clathrin/caveolar-mediated endocytosis, phagocytosis, macropinocytosis, and pinocytosis. Nanoparticles exit the cell via three types of pathway: lysosome secretion, vesicle-related secretion, and non-vesicle-related secretion. MVBs: multivesicular bodies. (Taken from (Oh and Park 2014).)

As mentioned above, endocytosis is actin-dependent and therefore a lot of research had been done on the role of actin as an important player in endocytosis. Actin is no longer

regarded as a passive barrier that must be removed to allow endocytosis to proceed but to assist the remodelling of the cell surface to allow inward movement of vesicles (Smythe and Ayscough 2006). Without the appropriate lipid environment, membrane curvature, which is crucial for vesicle formation, cannot occur. However, membrane lipids also regulate the activity of several actin-binding proteins, including capping protein (Amatruda and Cooper 1992). In this context, also the role of Plastin 3 and its rescuing effect on disturbed types of endocytosis (clathrin- and non-clathrin-mediated and activity-dependent bulk endocytosis) in SMA mice were further investigated in the present study ((5.13) and (Hosseinibarkooie et al. 2016)).

2. Aims

Spinal muscular atrophy (SMA) is an autosomal recessive neurodegenerative disorder characterized by the loss of α-motor neurons in the anterior horns of the spinal cord, thus leading to atrophy and paralysis of proximal symmetrical muscles. Patients suffering from SMA, in almost all cases, show homozygous deletion of the *survival of motor neuron 1 gene* (*SMN1*) and the severity of the disease is inversely correlated with the copy number of the *survival motor neuron 2 gene* (SMN2) the main SMA modifying gene.

Our group identified *Plastin 3* (*PLS3*) as a first independent of SMN protective SMA modifying gene, showing high expression in asymptomatic homozygously *SMN1*-deleted siblings of discordant SMA families. PLS3 has been found to be expressed at very high levels in human spinal cord. Cell culture experiments as well as *in vivo* SMA animal models (zebrafish and mouse) revealed that *PLS3* overexpression rescues the axonal outgrowth phenotype (Oprea et al. 2008). We subsequently generated a transgenic mouse model overexpressing PLS3. Severely affected SMA mice overexpressing PLS3 heterozygously showed improved motoric abilities as a consequence of increased neuromuscular junctions (NMJ) and muscle fibre size as well as an increase of proprioceptive input on motor neuron (MN) soma. Most importantly, PLS3 overexpression delayed axon pruning and improved connectivity of the presynapse to motor endplates. Nonetheless, survival was subtly extended by only a few days, as a result of massive inner organ impairment in SMA mice which was not rescued by PLS3 overexpression (Ackermann et al. 2013).

The major aim of this study is to conclusively confirm that PLS3 overexpression rescues survival and multi-organ dysfunction on a SMN-ASO-induced intermediate SMA mouse model and thereby increases NMJ size, number of proprioceptive inputs, MN soma size, endocytic uptake, and motoric ability (grip strength force and tube test) in the intermediate SMA mouse model.

To do so, we decided to use a combinatorial therapy with a suboptimal dose of SMN antisense oligonucleotide and PLS3 overexpression – a situation resembling the human condition in asymptomatic *SMN1*-deleted individuals.

The following steps were proposed:

1. Generation of two congenic SMA mouse models that will allow us to track back the effect of the modifier and exclude additional factors that might influence the SMA phenotype.

2. Generation and detailed analysis of SMA mice expressing PLS3 homozygously.

3. Development of an intermediate SMA mouse model by using different suboptimal doses of SMN-ASOs injected in the severe SMA mouse model. Two parameters, which may influence the outcome of the phenotype, postnatal day of injection and mode of ASO delivery, will be investigated, in order to identify the most appropriate combination.

4. Understanding the influence of low dose SMN-ASOs on the outcome of the SMA phenotype by using two different congenic strains: C57BL/6N and FVB/N.

5. Generation of SMA mice treated with suboptimal SMN-ASO doses and overexpressing PLS3 heterozygously and homozygously to analyse the impact of PLS3 in an intermediate SMA mouse model.

6. Detailed analysis of these mice including survival, weight progression, motoric abilities (tube test, righting reflex test, grip strength test) development of inner organs (heart, lung, intestine), analyses of MNs, NMJs and muscles by histological and immunofluorescent analyses, expression analysis of SMN and PLS3.

7. Analysis of endocytosis in SMA-PLS3 and SMA murine embryonic fibroblasts (MEFs).

3. Materials

3.1 DEVICES AND UTILITIES

Table 1: Devices and Utilities

Type of device	Designation	Manufacturer
Apotome	Apotome.2	Zeiss
Balance	EW	Kern
Balance	Adventurer	Ohaus
Balance (fine scale)	ARJ 120-4M	Kern
Bipolar electrode holder	MEW-F15B	Warner Instruments
Borosilicate glass tubes	GB150T-8P	Science Products GmbH
Centrifuge	Allegra X22-R	Beckmann Coulter
Centrifuge	Avanti J-20XPI	Beckmann Coulter
Centrifuge	5415R	Eppendorf
Centrifuge	5415D	Eppendorf
Centrifuge	Galaxy Mini	VWR
Electrophoresis chamber	E-H6	Febikon
Electrophoresis chamber	E-PB 0	Febikon
Electrophoresis chamber	Mini-Protean 3 cell	BioRad
Electrophoresis chamber	Mini-Protean Tetra System	BioRad
Fluorescence lamp	HXP 120 C	Zeiss
Freezer (-80°C)	HERA freeze	Heraeus
Gel documentation	ChemiDoc XRS	BioRad
Gel documentation	Gel Doc XR+	BioRad
Grip strength meter	303500	TSE Systems
Hamilton needle (30/30/4)	7803-07	Hamilton
Hamilton syringe RN 5 µL	HAMI7634-01	Hamilton
Heating block	DB 3D	Techno
Heating magnetic stirrer	MR3001	Heidolph
Homogenizer	T10 basic, Ultra Turrax	IKA
Homogenizer	Precellys 24	Peqlab
Ice machine	AF 80	Scotsman
Incubator	Innova 44	New Brunswick Scientific
Incubator	Innova 4230	New Brunswick Scientific
Incubator, tissue culture	HERA cell 150	Heraeus

Type of device	Designation	Manufacturer
Laminar airflow cabinet	HERA safe	Heraeus
Light source (Fibre optic)	KL 1500 LCD	Leica
Microplate reader	Safire^2	Tecan
Microscope (BF)	Axioshop 2	Zeiss
Microscope (Confocal)	Meta 510	Zeiss
Microscope (Fluorescence)	Imager M2	Zeiss
Microscope (stereo)	S8AP0	Leica
Microscope camera	AxioCam MRm	Zeiss
Microscope camera	AxioCam ICc 1	Zeiss
Microscope camera	AxioCam ERc 5s	Zeiss
Microtome	RM2255	Leica
Microwave	R-898(AL)-A	Sharp
Orbital Shaker	3015	GFL
pH meter	inoLab pH level 1	WTW
Photometer	BioPhotometer	Eppendorf
Photometer	NanoDrop 1000	Peqlab
Pipette	Research (2.5/10/20/100/ 200/1000/5000 µL)	Eppendorf
Pipette (automatic)	Research Pro (10/100 µL)	Eppendorf
Pipette (repetitive)	Multipette Plus	Eppendorf
Pipettor	Pipetboy acu	Integra biosciences
Power supply	PowerPac Basic	BioRad
Power supply	PowerPac HC	BioRad
Power Supply	252	Zeiss
Real-time Thermocycler	Light Cycler 1.5	Roche
Roll incubator	SRT9	Stuart
Roll incubator	SRT6D	Stuart
RotaRod	RotaRod advanced Systems	TSE Systems
Safety gas-burner	Fireboy Plus	IBS
Shaker + heating block	HLC	Ditabis
Speed Vac	Concentrator 5301	Eppendorf
Thermocycler	DNAengine Tetrad2	MJ Research
Thermocycler	DNAengine Dyad	MJ Research
Thermocycler	S1000	BioRad
Thermocycler	C1000 Touch	BioRad
Tissue processor	TP1028	Leica
Transfer System	Trans-Blot Turbo	BioRad
Ultrasonicator	Bioruptor	Diagenode

Type of device	Designation	Manufacturer
Universal digital stimulator	MS501	custom-made (Uni Köln)
Universal stimulus isolator	MI401	custom-made (Uni Köln)
Vacuum pump	PM12640-026.3	Biometra
Vortex	444-1372	VWR
Water bath	1083	GFL

3.2   CHEMICALS

Table 2: Chemicals

Chemical	Manufacturer
2-Mercaptoethanol (99%, p.a.)	AppliChem
2-Propanol (≥ 99.5%)	AppliChem
Acetic acid	AppliChem
Acetone	AppliChem
ADVASEP-7	Sigma
Agarose (low melting)	Biozym
Agarose for routine use	Sigma-Aldrich
Ammonium persulfate	AppliChem
Bovine serum albumin (BSA)	Sigma-Aldrich
Bromophenol blue	AppliChem
Chloroform	AppliChem
Citrate	AppliChem
Control-ASO 439272	IONIS Pharmaceuticals
Coomassie Brilliant Blue R-250	AppliChem
D-glucose	AppliChem
Dimethyl sulfoxide (DMSO)	Sigma-Aldrich
Disodium hydrogen phosphate (p.a.)	AppliChem
Dithiothreitol (DTT)	AppliChem
Ethanol (≥ 99.5%, p.a.)	AppliChem
Ethidium bromide (1% in H2O)	AppliChem
Ethylenediaminetetraacetic acid (EDTA)	AppliChem
FITC-Dextran	Sigma-Aldrich
FM1-43	Molecular Probes
Formaldehyde (37%, p.a.)	AppliChem
Glycerol (86%, p.a.)	AppliChem

Chemical	Manufacturer
Glycine	AppliChem
Hoechst	Life Technologies
Hydrochloric acid (37%, fuming)	AppliChem
Hydroxymethylaminoethane (Tris)	AppliChem
Isoamylalcohol	AppliChem
Methanol (≥ 99.9%, p.a.)	AppliChem
Milk powder (low fat)	AppliChem
Mowiol	Roth
Paraformaldehyde	Fluka
Phenol	AppliChem
SMN2-ASO 387954	IONIS Pharmaceuticals
Sodium acetate	AppliChem
Sodium chloride (p.a.)	AppliChem
Sodium dihydrogen phosphate dihydrate (p.a.)	AppliChem
Sodium dodecyl sulfate (SDS, 10% in H2O)	AppliChem
Sodium hydroxide	AppliChem
Tertramethylethylenediamine (TEMED)	AppliChem
Triton X-100	AppliChem
Trizma base	Sigma-Aldrich
Tween-20 (Polysorbate 20)	AppliChem
Water (HPLC grade)	Sigma-Aldrich
Xylene	AppliChem

3.3   KITS

Unless noted otherwise, all kit-related procedures have been performed according to the manufacturer's instructions.

Table 3: Kits

Name	Manufacturer
DNeasy Blood and Tissue Kit	Qiagen
gDNA Blood & Tissue Kit	Qiagen
Light Cycler Fast Start DNA Master SYBR green I	Roche
QIAshredder	Qiagen

Name	Manufacturer
Quant-iT RiboGreen RNA assay Kit	Life Technologies
QuantiTect Reverse Transcription Kit	Qiagen
RNeasy Mini Kit	Qiagen
Superscript II Reverse Transcription Kit	Life Technologies

3.4   REAGENTS AND EQUIPMENT

3.4.1   Reagents

Table 4: Reagents

Reagent	Manufacturer
Quick-Load® Purple 2-Log DNA Ladder	New England Biolabs
AquaPlus Mix 30% (29:1 Acrylamide/Bisacrylamide)	AppliChem
Bradford reagen	AppliChem
Complete Mini Protease Inhibitors	Roche
Eosin-Y solution	Sigma-Aldrich
Eukitt mounting medium	Fluka
Mayer's Hematoxylin	Sigma-Aldrich
OneTaq® Quick-Load 2X Master Mix with Std.-Buffer	New England Biolabs
Page Ruler Prestained Protein Ladder	Thermo
PBS (10x)	VWR
Ponceau S	Sigma Aldrich
QIAzol Lysis Reagent	Qiagen
Restore Western Blot Stripping Buffer	Thermo
Ripa buffer	Sigma-Aldrich
Super Signal West Pico ECL Substrate	Thermo
TBE (10x)	Sigma-Aldrich

3.4.2 Enzymes and growth factors

Table 5: Enzymes and growth factors

Type	Name	Manufacturer
Enzyme	DNAse I	AppliChem
Enzyme	Proteinase K	AppliChem
Enzyme	Recombinant Taq DNA Polymerase	Life Technologies
Enzyme	RNase A	Sigma-Aldrich
Growth factor	Murine GDNF	Pepro Tech
Growth factor	Human BDNF	Pepro Tech
Growth factor	Rat CNTF	Pepro Tech

3.4.3 Cell culture reagents and media

Table 6: Cell culture reagents and media

Type	Name	Manufacturer
Antibiotic	G418 (Geniticin)	Sigma-Aldrich
Antibiotic	Penicillin/Streptomycin	Life Technologies
Antibiotic	Zeocin	Life Technologies
Coating solution	Laminin	Thermo
Coating solution	Poly-D-lysine	Sigma-Aldrich
Fungicide	Amphotericin B	Promocell
Medium	DMEM	Life Technologies
Medium	DMEM transparent	Life Technologies
Medium	Glutamax	Life Technologies
Medium	HBSS	Life Technologies
Medium	PBS	Life Technologies
Medium	Neurobasal	Life Technologies
Medium	Opti-MEM	Life Technologies
Medium	Trypsin/EDTA	Life Technologies
Serum	Fetal Bovine Serum	Biochrom
Serum	Horse Serum	Biochrom
Supplement	B27	Life Technologies
Supplement	BSA	Sigma-Aldrich
Supplement	Glucose	AppliChem

Type	Name	Manufacturer
Supplement	Trypsin	AppliChem
Supplement	Trypsin Inhibitor	AppliChem

3.4.4 Equipment for laboratory mouse work

Table 7: Equipment for laboratory mouse work

Type	Name	Manufacturer
Cell strainer	Nylon mesh, 70 µm	BD Falcon
Ear tag applicator	1005-s1	National Band & Tag Co.
Ear tags	1005-1	National Band & Tag Co.
Forceps	DB047R	Aesculap
Forceps	Dumont #5 (11252-20)	Fine Science Tools
Forceps	Dumont #5/45 (11251-33)	Fine Science Tools
Forceps	Dumont #55 (11255-20)	Fine Science Tools
Forceps	FM002R	Aesculap
Pins	Minutien	Plano
Scissors	BC100R	Aesculap
Scissors	BC321R	Aesculap
Scissors	BC8641R	Aesculap
Silicone Elastomer	Silgard 184	Sigma-Aldrich

3.5 SOLUTIONS AND MEDIA

Table 8: Solutions and Media

Name	Composition
Citrate buffer	10 mM citrate; pH 6
DEPC H2O	0.1% (v/v) DEPC in H2O; stir over night; autoclave
DNA sample buffer, 10x	100 mM EDTA (pH 8); 1% (w/v) SDS; 50% (v/v) Glycerin; 0.1% (w/v) Bromophenol blue; 0.25% (w/v) Xylene cyanol
dNTP Mix (1.25 mM per dNTP)	5 µl dATP; 5 µl dCTP; 5 µl dGTP; 5 µl dTTP; 480 µl H2O
Lysis buffer (tissue)	200 mM NaCl; 100 mM Tris-HCl; 5 mM EDTA; 0.2% (w/v) SDS; pH 8.5; 200 µg/ml proteinase K (fresh)

Name	Composition
Paraformaldehyde (4%)	4% paraformaldehyde, dilute in 30 ml H2O at 60°C; add 1 M NaOH to clear the solution; cool down and filter; add 50 ml 2x PBS, pH 7.4
Resolving gel (SDS-PAGE), 12%	3.3 ml H2O; 4 ml 30% acrylamide mix; 2.5 ml 1.5 mM Tris pH 8.8; 100 µl 10% SDS; 100 µl 10% APS; 4 µl TEMED
SDS electrophoresis buffer, 10x	0.25 M Tris; 1.92 M Glycine; 1% (w/v) SDS; pH 8.3
SDS sample buffer (2x)	0.757 g Tris-base; 20 ml glycerol; 10 mg Bromophenol blue; 6 g SDS; ad 90 ml H2O; add 1/10 Vol. ß-ME before use
Stacking gel (SDS-PAGE), 4%	1.4 ml H2O; 330 µl 30% acrylamide mix; 250 ml 1.5 mM Tris pH 6.8; 20 µl 10% SDS; 20 µl 10% APS; 2 µl TEMED
TBST	0.5% (v/v) Tween-20 in TBS
TE buffer	10 mM Tris; 1 mM EDTA; pH 8
TE^{-4} buffer	10 mM Tris-HCl; 0.1 mM EDTA; pH 8
Transfer buffer (Western Blot)	15 mM Tris-base; 150 mM Glycine; 20% (v/v) Methanol

3.6   CELL CULTURE

3.6.1   Cell lines

The following cell lines were employed in this study:

- MEFs: Cells were derived from mouse embryos (E13.5) and isolated as described in section 4.2.1. The embryos had been obtained from breedings of the severe SMA mouse model (Taiwanese SMA mice (Hsieh-Li et al. 2000)) with and without the disease modifier PLS3 (Ackermann et al. 2013).

- MNs: Cells were derived from mouse embryos (E13.5) and isolated as described in section 4.2.2. The embryos had been obtained from breedings of the severe SMA mouse model (Taiwanese SMA mice (Hsieh-Li et al. 2000)) with and without the disease modifier PLS3 (Ackermann et al. 2013).

3.7 MOUSE INBREAD STRAINS

The PLS3V5 transgene mouse model (Ackermann et al. 2013) were cross-bred with the severly affected SMA mouse model (Taiwanese SMA mice (Hsieh-Li et al. 2000)) to study the influence of *PLS3* overexpression (OE) in SMA mice. For this purpose and using the *Cre/loxP* system, a *V5*-tagged version of human *PLS3* was targeted into the murine *Rosa26* locus in order to ubiquitously or tissue specific overexpress *PLS3*. All animals were maintained either on a congenic C57BL/6N or FVB/N background. At first, the Taiwanese SMA mouse model was only available on FVB/N background, therefore we needed this mouse line to be crossed back for at least eight times in order to receive a SMA mouse on pure C57BL/6N background. So far, these mice are crossed back more than 20 generations. In the beginning of this study, the generation of the SMA-PLS3hom and HET-PLS3hom mice was necessary, as in previous experiments only SMA-PLS3het and HET-PLS3het mice had been used (Ackermann et al. 2013).

3.8 ANTIBODIES

3.8.1 Primary antibodies

Table 9: Primary antibodies

Antibody	Host species	Block ing	Dilution	Incuba tion	Supplier	Product
α-β-actin	mouse, monoclonal	milk	WB: 1:30,000	1 hour	Sigma-Aldrich	A5316
α-ChAT	goat, polyclonal	BSA	IHC/ICC: 1:300	o. n.	Millipore	AB144P
α-NF	mouse, monoclonal	BSA	IHC/ICC: 1:100	o. n.	Hybridoma Bank	AB_2314897
α-PLS3	rabbit, monoclonal	milk	WB: 1:1,000	o. n.	produced by AG Wirth	N/A
α-SV2	mouse, monoclonal	BSA	IHC: 1:100	o. n.	Hybridoma Bank	AB_2315387
α-V5-HRP	mouse, monoclonal	milk	WB: 1:3000	o. n.	Life Technologies	46-0708
α-VGlut1	rabbit, polyclonal	BSA	IHC: 1:300	o. n.	Synaptic Systems	135303

3.8.2 Secondary antibodies

Table 10: Secondary antibodies

Antibody	Host species	Blocking	Dilution	Incubation	Supplier	Product
α-goat IgG Alexa fluor 568	donkey	BSA	1:750	2 hours	Life Technologies	A11057
α-mouse IgG Alexa fluor 488	donkey	BSA	1:500	2 hours	Life Technologies	A10667
α-mouse IgG (HRP conjugate)	goat	milk	1:5,000	1 hour	Immuno Research	N/A
α-rabbit IgG Alexa fluor 488	donkey	BSA	1:750	2 hours	Life Technologies	A21206
α-rabbit IgG (HRP conjugate)	goat	milk	1:5,000	1 hour	Cell signaling	7074S
Bungarotoxin (BTX)	None	none	10 µL stock/7 mL PBS	10 min	Life Technologies	B1601
Phalloidin Alexa fluor 568	none	none	1:40	1 hour	Life Technologies	A12380

3.9 OLIGONUCLEOTIDES AND PCR CONDITIONS

All oligonucleotides used and optimized in this study are listed below. *Amplicon* defines the target of the PCR. *Oligonucleotide* sequences are listed in 5' to 3' direction, while forward primers are designated as *fwd*, reverse primers as *rev*. The given *identification number* corresponds to the in house primer database. *Product* gives the length of the PCR product in base pair. The column *°C* indicates the optimal annealing temperature. For genotyping 35, for quantitative PRC 40 cycles had been used.

3.9.1 Oligonucleotides for genotyping

Genotyping of mice was performed as previously described using the following primers and conditions (Ackermann et al. 2013).

Table 11: Oligonucleotides for genotyping

Inbred strain	Amplicon		Oligonucleotide 5'>3'	ID#	Name	Annealing/ Amplicon length
SMA-Hung	WT *Smn*	fwd	ATAACACCACCACTCTTACTC	3370	HungSMA_mouse_ wt/Mut_fw_S1	59°C/ 1050 bp
		rev	GTAGCCGTGATGCCATTGTCA	3372	HungSMA_mouse_ wt_rev_H1	
	Hung KO	fwd	AGCCTGAAGAACGAGATCAGC	3371	HungSMA_mouse_ wt_rev_S2	59°C/ 950 bp
		rev	ATAACACCACCACTCTTACTC	3370	HungSMA_mouse_ wt/Mut_fw_S1	
	hSMN2 tg	fwd	CGAATCACTTGAGGGCAGGAGTTTG	3375	HungSMA_mouse_t g*hSMN2*_fw_2F	59°C/ 479 bp
		rev	AACTGGTGGACATGGCTGTTCATTG	3376	HungSMA_mouse_t g*hSMN2*_rev_2B	
PLS3V5	*PLS3V5* rec	fwd	AAAGTCGCTCTGAGTTGTTATC	3650	Typ_forw	56°C/
PLS3V5	*PLS3V5* rec	rev	GATATGAAGTACTGGGCTCTT	3649	Typ_rev_wt	380 bp
	PLS3V5 wt	fwd	AAAGTCGCTCTGAGTTGTTATC	3650	Typ_forw	56°C/ 576 bp
		rev	TGTCGCAAATTAACTGTGAATC	3648	TYP_rev_CAGS	

3.9.2 *Oligonucleotides for quantitative PCR*

Primer usage for quantitative real-time PCR on the *Roche Light Cycler 1.5.* Quantitative real-time PCR was performed as previously described using the following primers and conditions (Riessland et al. 2010).

Table 12: Oligonucleotides for quantitative PCR

Name	Oligonucleotide 5'>3'	Product [bp]	°C	ID#
SMN-FL-Δ7-fwd	CCACCACCCCACTTACTATCA	236	62	1449
SMN-FL-rev	GCTCTATGCCAGCATTTCTCCT	236	62	3054
SMN-FL-Δ7-fwd	CCACCACCCCACTTACTATCA	236	61	1449
SMN-Δ7	GCTCTATGCCAGCATTTCCATA	182	61	1450
Gapdh	GGCTGCCCAGAACATCATCC	169	63	3999
Gapdh	GTCATCATACTTGGCAGGTTTCTC	169	63	4000

3.10 SOFTWARE, WEB APPLICATIONS AND DATABASES

3.10.1 Software

Table 13: Software

Name	Purpose	Manufacturer
AutoStitch 2.2	Image processing (panoramic assembly)	University of British Columbia
EndNote X7	Reference management	Thomson Reuters
Excel 2007/2013	Plots, charts, data processing, statistics	Microsoft
Image J (Fiji)	Image processing, Z-stacks, densitometric analysis	NIH
Mausoleum	Laboratory mouse management	Dr. Hanns-Eugen Stöffler
Prism 7	Plots, charts, data processing, statistics	GraphPad Software
Pyrat	Laboratory mouse management	Scionics
Light Cycler Software	Quantitative real-time PCR analysis	Roche
Power Point 2007/2013	Image illustration	Microsoft
Quantity One 4.5.1	Densitometric analysis	BioRad
Word 2007/2013	Word processing	Microsoft
ZEN 2	Fluorescence imaging and analysis	Zeiss

3.10.2 Databases and web applications

Table 14: Databases und web applications

Name	URL
BfR	http://www.animaltestinfo.de/antragsteller
Ensembl	http://www.ensembl.org/index.html
Genecards	http://www.genecards.org/
Ingenuity Systems	http://www.ingenuity.com/
NCBI	http://www.ncbi.nlm.nih.gov/
OligoCalc	http://basic.northwestern.edu/biotools/OligoCalc.html
Pubmed	http://www.ncbi.nlm.nih.gov/pubmed
UniProt	http://www.uniprot.org/

4. Methods

4.1 WORKING WITH LABORATORY MICE

4.1.1 Mouse experiments

All procedures involving laboratory animals were performed according to the German laws of animal welfare and were approved by the '*Landesamt fuer Natur, Umwelt und Verbraucherschutz NRW*' under the reference numbers 84-02.05.20.12.120, 84-02.04.2014.A006 and 84-02.04.2015.A378. Animals used in this study were kept in the animal facility of the Institute for Genetics at the University of Cologne.

4.1.2 Breeding of SMA-PLS3 and control mice

The Taiwanese SMA mouse model FVB.Cg-Tg (SMN2)2Hung Smn1tm1Hung/J, stock number 005058 (here named $Smn^{KO/KO};SMN2^{tg/tg}$) was purchased from Jackson Laboratory. In our laboratory, we backcrossed these mice for more than seven generations to obtain a congenic C57BL/6N background. We maintained the breeding colony by crossing $Smn^{KO/KO};SMN2^{tg/tg}$ mice and $Smn^{KO/WT}$ mice with WT mice. PLS3-overexpressing transgenic animals were used for generating $Smn^{KO/KO};SMN2^{tg/0};PLS3^{tg/0}$ (SMA-*PLS3*het) and $Smn^{KO/KO};SMN2^{tg/0};PLS3^{tg/tg}$ (SMA-*PLS3*hom) mice as well as HET-*PLS3*het and HET-*PLS3*hom mice as shown in Figure 10, and animals were genotyped as described in 4.1.3.

PARENTS

$Smn^{KO/KO};SMN2^{tg/tg};PLS3^{tg/0}$ **X** $Smn^{WT/KO};PLS3^{tg/0}$

OFFSPRING

12.5%	$Smn^{KO/KO};SMN2^{tg/0};PLS3^{tg/tg}$	SMA-*PLS3*hom
25%	$Smn^{KO/KO};SMN2^{tg/0};PLS3^{tg/0}$	SMA-*PLS3*het
12.5%	$Smn^{KO/KO};SMN2^{tg/0}$	SMA
12.5%	$Smn^{WT/KO};SMN2^{tg/0};PLS3^{tg/tg}$	HET-*PLS3*hom
25%	$Smn^{WT/KO};SMN2^{tg/0};PLS3^{tg/0}$	HET-*PLS3*het
12.5%	$Smn^{WT/KO};SMN2^{tg/0}$	HET

Figure 10: Breeding scheme: Generation of SMA, SMA-*PLS3*het, SMA-*PLS3*hom, HET, HET-*PLS3*het and HET-*PLS3*hom genotypes.

4.1.3 Tagging and genotyping

Offspring of a breeding was weaned 3 weeks after birth and animals were separated by sex. To allow accurate animal management each animal was tagged with a numbered ear tag. For genotyping purposes a biopsy of the tail tip was taken (approx. 3 mm) according to the German laws for animal welfare (TierSchG §6). Oligonucleotides and genotyping conditions are listed in 3.9.1.

4.1.4 Timed breeding

The generation of MEFs (4.2.1) and MNs (4.2.2) requires precise knowledge about the developmental stage of the analyzed embryo. For this purpose controlled timed matings were performed. Two nonpregnant females were mated with one male (o. n). The following morning females were surveyed for the presence of a vaginal plug indicative of copulation during the night. Vaginal plugs are remnants of the male ejaculate that can be present up to 24 hours after mating. Positively tested females were isolated and were considered to carry embryos at the stage of 0.5 dpc assuming fecundation in the middle of the night.

4.1.5 Isolation of prenatal mouse embryos

Mouse embryos were prepared following a timed breeding (4.1.4). The pregnant mother was sacrificed at the desired developmental stage by CO_2 gas. The uterus harboring embryos was fully transferred to PBS. Embryos were prepared from the uterus and the head was removed for genotyping purposes. Isolated embryos were either used for the isolation and generation of MEFs (4.2.1) or MNs (4.2.2).

4.1.6 Subcutaneous injection of ASOs

The SMN-ASO and Ctrl-ASO (IONIS Pharmaceuticals, (Hua et al. 2011)) were diluted in sterile PBS, and the concentration of 10 mg/mL (working solution) was calculated with photometric density (AD260). The subcutaneous injections (10–50 mg) were performed on postnatal days 2 and 3 (P2 and P3) with a MICROLITER Syringe (Hamilton) as reported (Hua et al. 2011). All pups of each litter were double blindly injected.

4.1.7 Righting reflex and tube test

The righting reflex test is a method to examine muscle strength. For this test, animals were placed on their back on a flat surface. The time to reposition themselves was measured over a 30 sec period. The righting times were related to a score in the following manner: < 1 sec = 0, 1 – 2 sec = 1, 3 – 4 sec = 2, 5 – 6 sec = 3, 7 – 8 sec = 4, 9 – 10 sec = 5, > 10 sec = 6 (El-Khodor et al. 2008). Via the tube test, the proximal hind limb muscle strength, weakness, and fatigue in neonates was assessed. The test is performed in two consecutive trials, in which the animal is placed head down into a 50 mL Falcon tube so that the animal hangs by its hind limbs (Figure 11). Then, the hind limb score (HLS) is evaluated on the basis of the positioning of the hind limbs toward each other (El-Khodor et al. 2008).
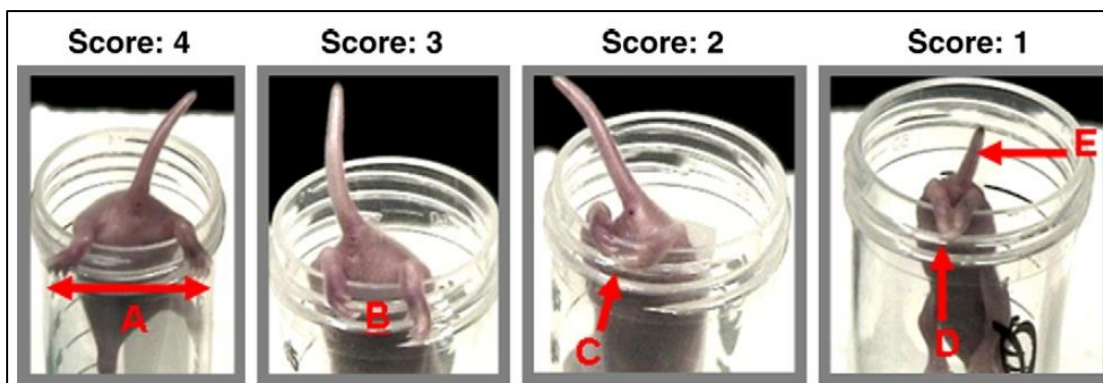
Figure 11: Tube test (El-Khodor et al. 2008): Hind limb scores (HLS) and respective leg positions for motoric ability assessment

4.1.8 Grip strength test

The Grip Strength Meter (TSE Systems) is a system for determining the gripping strength of small laboratory animals (such as rats and mice). The animal pulls a special height-adjustable grip (with two paws) that is mounted on a high-precision force sensor, and muscle force is recorded in pounds (Passini et al. 2010). The grip strength test was performed at P36 and P108.

4.2 EUKARYOTIC CELL CULTURE

All cell culture procedures were performed under sterile conditions using a laminar flow workbench. To prevent contamination with bacteria or fungi the growth medium was

complemented with penicillin, streptomycin and amphotericin B unless noted otherwise. Eukaryotic cells were grown in sterile incubators at 37°C, 5% CO_2 and 95% relative humidity.

4.2.1 Generation of murine embryonic fibroblasts (MEFs)

MEFs were isolated from 13.5 dpc mouse embryos. Mice of the desired genotype were cross-bred in a timed breeding (4.1.4) to determine the progression of pregnancy. Pregnant female mice were sacrificed by CO_2 gas and embryos were prepared from the uterus under sterile conditions and washed in PBS. Visible organs like heart and liver were removed from the embryos. The heads were used for the isolation of DNA (4.3.1.3) for genotyping purposes. The embryo was ground in a 70 µm nylon cell filter using a plunger of a 20 mL syringe. The ground material was flushed through the cell filter with 25 mL of cell culture medium freshly complemented with antibiotics. Cells were pelleted by spinning for 5 min at 1200 rpm. Cells were resuspended in 6 mL of culture medium and plated into a 6 cm tissue culture plate. After 24 h cells were three times carefully washed in PBS to remove cellular debris. Cells were expanded while providing fresh culture medium daily. This protocol was adapted from (Ackermann et al. 2013).

4.2.2 Generation of murine embryonic motor neurons (MNs)

MNs were isolated from 13 dpc mouse embryos. Mice of the desired genotype were cross-bred in a timed breeding (4.1.4) to determine the progression of pregnancy. Pregnant female mice were sacrificed by CO_2 gas and embryos were prepared from the uterus under sterile conditions and washed in PBS on ice. Coverslips in 12-well plates were coated with poly-D-lysine in PBS (1:100) for one hour. After the incubation time, cover slips needed to be washed three times in sterile PBS and left to dry. Then they were coated with laminin. 700 µL PBS was put in eppendorf tubes for collecting spinal cords from mouse embryos after they had been isolated from them. Therefore, embryos needed to be fixed with four minutien pins on silgard dishes filled with PBS. The heads were cut off in advanced and used for the isolation of DNA (4.3.1.3) for genotyping purposes. Embryos were fixed with their back in upside position. First, the skin was gently torn away on the back of the embryo, then the spinal cord (s. c.) was removed by cutting with minutien pins on each side of the spine. Afterwards, fine science forceps were slid under to carefully loosen the s. c.. The surrounding meninges including ganglia cells were removed as completely as possible. The collected s. c. were stored in PBS on ice for some time until the isolation of all s. c. was

finished. All further steps were carried out under the sterile hood. The s. c. were centrifuged for 10 min at 1000 x g and 4°C. Afterwards the supernatant was removed and discarded. In the meanwhile a trypsin solution (1:20) was prepared. 500 µL of this solution was added to each tube, samples were mixed and centrifuged for 10 min at 1000 x g and 4°C. During that time the plating medium was prepared and sterile filtered (50 mL: 45.5 mL DMEM, 2.5 mL FBS, 1.5 mL 20% glucose, 0.25 mL penicillin, 0.25 mL streptomycin, 0.5 mL amphotericin B). The trypsin was pipetted off and the trypsinization reaction was stopped with 500 µL plating medium containing DNAse I (1:20). Spinal cords were resuspended with by very carefully pipetting up and down. Then more plating medium was added to adjust the volume. Tubes were left for 2 min for bigger debris to stay at the bottom. The upper fraction was taken of the solution without touching the tube's bottom with the tip and transferred to interim plates for 30 min. Afterwards, the cell suspension was taken to a tube, cells were counted (70.000 cells/cover slip) and incubated o. n. at 37°C. On the next day, the medium was changed to Neurobals Medium (10 mL: 200 µL B27, 20% glucose, 200 µL horse serum, 10 µL mGDNF, 10 µL hBDNF, 10 µL rCNTF). Cells were cultured for 7 days. This protocol was adapted from (Oprea et al. 2008).

4.2.3 Cultivation of eukaryotic cells

Murine embryonic fibroblasts (MEFs) were cultivated in DMEM (*Dulbeccos's Modified Eagle Medium*) complemented with 10% fetal bovine serum. Routinely, cells were cultivated in 75 cm² or 25 cm² tissue culture flasks and split into new flasks when reaching confluence state. Cells were washed with 1x PBS without Mg^{2+} and Ca^{2+} and trypsinized using Trypsin-EDTA until cells detached from the surface. Trypsinization was stopped with at least 1 volume of culture medium. The cell suspension was homogenized and evenly distributed to new tissue culture flasks. Depending on the proliferation rate cells were distributed at different density. In general, MEFs were split 1:5. MNs were cultivated in plating medium o. n. (first day after isolation) and Neurobasal medium (+B27, +20% glucose) from the second day on as described in section 4.2.2. MNs were never cultured for longer time periods. Therefore no cell splitting was necessary. They were always harvested after one week for further experiments.

4.2.4   Counting cells using a Neubauer cytometer

Some applications required defined cell numbers and growth densities to work optimally. To determine the number of cells in a suspension, a Neubauer counting chamber was used. After trypsinization of cells (4.2.1) cells were well homogenized in excess of culture medium. 30 µL of the homogenized suspension were applied to the counting chamber. Under a standard microscope the cell number was determined in 4 quadrants of the counting chamber and the mean was calculated. The cell concentration in the cell suspension is mean of determined cells in 4 quadrants x 10^4 cells/ml.

4.2.5   Treatment of cells with FITC-Dextran

MEFs were plated cover slips in 12-well plates (100.000 cells/well) in 1 mL normal DMEM growth medium and kept o. n. to attach and grow. At the next day a 10x FITC-dextran stock solution (50 mg/mL) was prepared in sterile PBS. Then the growth medium was removed from the cells. To each well 500 µL of starvation medium was added (DMEM transparent, +2% FBS). MEFs were incubated for 10 min at 37°C. During the incubation time 1x FITC-dextran working solution was prepared (5 mg/mL) in starvation medium. The starvation medium was removed from the cells and 500 µL of 1x FITC-dextran was added per well. MEFs had been incubated for 0, 10 and 20 min at 37°C (in tripletts). Afterwards the solution was removed and the cells were placed on ice and washed three times with icecold PBS. Phalloidin was added to each well and incubated for one hour at room temperature (RT), then washed three times with PBS and stained with Hoechst (3 min). Finally, MEFs were washed again three times with PBS, rinsed in sterile water and mounted in Mowiol.

4.2.6   Immunostaining procedures for MNs

Cover slips with cultured MNs upon were fixed with 4% PFA for 15 min after being transfered to a new 12-well plate. Next, they were washed three times with PBS for 5 min. In the following step they were permeabilized in PBS containing 0.2% Triton X-100 for 5 min and then blocked in PBS containing 5% BSA and 5% horse serum for approx. one hour, followed by the incubation with the first antibody (o. n.) in PBS containing 5% BSA and 5% horse serum (α-ChAT, α-NF: both 1:100 (Table 9)). On the next day, the MNs were washed three times for 10 min with PBS and afterwards incubated with the secondary antibody (two hours) in PBS containing 5% BSA (α-goat IgG Alexa fluor 568, α-rabbit IgG Alexa fluor 488: both

1:500 (Table 10)). Again the cells needed to be washed three times for 10 min with PBS and afterwards stained with Hoechst (3 min). Finally, MNs were washed for 5 min in PBS, rinsed in sterile water and mounted in Mowiol.

4.2.7 Cryoconservation of cells

Confluent cell layers were detached from the surface by trypsinization (4.2.1). Cells were pelleted by centrifugation at 200 x g for 5 min and resuspended in cryo-medium containing DMSO as a cryoprotective agent. For MEFs a cryomedium containing 10% DMSO in FBS was applicable. Cells from a growth area of 25 cm² were resuspended in 1 ml of cryo-medium and transferred to a cryo-tube. These were frozen to -80°C using an isopropanol-based freezing aid which allowed controlled cool down rates of approx. 1°C/min. For long term storage cells were transferred to liquid nitrogen storage. To take back frozen cells to culture, the frozen cryo-tube was quickly thawed in a 37°C water bath. The thawed cell suspension was transferred to pre-warmed culture medium and immediately plated to a 25 cm² tissue culture flask.

4.3 MOLECULAR BIOLOGY METHODS

4.3.1 Isolation of DNA

In the following chapter different methods of DNA purification will be explained. All methods vary in the obtained purity of DNA and the method of DNA isolation was chosen according to the downstream application. All isolated DNAs were stored at -20°C.

4.3.1.1 Isolation of genomic DNA from murine tail biopsies

A single tail biopsy sample was lysed in 493 µL tissue lysis buffer (3.5) complemented with 7 µL Proteinase K (200 µg/mL) at 55°C in a shaking heating block at approx. 900 rpm. Hair and insoluble debris were removed by 10 min centrifugation at 13200 rpm. The supernatant was mixed with 500 µL isopropanol in a new reaction tube to precipitate the DNA. Precipitation was continued for 2 min at RT. DNA was pelleted for 10 min at 13200 rpm and washed with 500 µL of EtOH. After centrifugation for 5 min at 13200 rpm the EtOH was discarded and the DNA was dried in a 37°C heated cabinet or in the Concentrator device.

At last the pellet was resuspended in 100 µL TE^{-4} (3.5) containing 50 µg/mL RNase A to degrade possible RNA contamination.

4.3.1.2   Isolation of genomic DNA from tissues

To obtain DNA of good purity from cells and animal tissues the gDNA Blood & Tissue kit (Qiagen) was used according to the manufacturer's instructions. For routine use, genomic DNA from pelleted cells and small amounts of tissue was isolated as previously described for tail biopsies (4.3.1.1). Depending on the tissue size the lysis step was increased in length. To improve DNA purity the lysate was optionally subjected to phenol-chloroform extraction (4.3.1.3).

4.3.1.3   Isolation of genomic DNA from tissues (Phenol-Chloroform)

Following tissue lysis in lysis buffer with proteinase K cellular debris was pelleted for 20 min at 13200 rpm. To minimize material loss during phenol-chloroform extraction a gel-based phase separating system was employed. Phase Lock Gel Heavy (5 Prime) tubes were prepared by spinning 1 min at 13200 rpm. The cleared lysate was transferred to the Phase Lock tube. 1 volume phenol-chloroform was added (i.e. ½ vol. phenol + ½ vol. chloroform/isoamylalcohol (24:1) and mixed by vortexing. The Phase Lock tube was rotated for 5 min and then spun for 5 min at 13200 rpm. The upper aqueous phase was transferred to a fresh Phase Lock tube and previous steps were repeated with 1 vol. of phenol-chloroform. The procedure was finally repeated with 1 vol. of pure chloroform/isoamylalcohol. After centrifugation the aqueous phase was mixed with 3 volumes of ice cold 100% EtOH and 0.1 vol. of 3M NaAc (pH 5.2). DNA was precipitated o. n. at -20°C and afterwards pelleted for 20 min at 13200 rpm. DNA was washed in 70% EtOH and repeatedly centrifuged. After drying in a heating cabinet, the pellet was resuspended in TE^{-4} with 50 µg/mL RNase A.

4.3.1.4   Isolation of genomic DNA concentration via spectrometry

Concentrations of DNA solutions were determined using a *NanoDrop ND-1000 spectrophotometer* (*Peqlab*). From the measured absorption at the wavelengths of 260 nm and 280 nm the software calculated the DNA concentration and determined the 260 nm/280 nm ratio which is an indicator for DNA purity. A value of 1.8 is indicative of high purity. Lower values point to possible remnants of ethanol, while higher values indicate the presence of RNA.

4.3.2   Isolation of RNA

RNA was handled under RNase-free conditions including appropriately treated reaction tubes and stuffed pipette tips. RNA in aqueous solution was always kept on ice and was stored at -80°C.

4.3.2.1   Isolation of RNA from tissues

Isolation of RNA from liver and s. c. was performed using the RNeasy Mini Kit (Qiagen) and QiaShredder (Qiagen) according to the manufacturer's instructions. To ensure optimal breakup of organ tissue, specimens were homogenized using a rotor-stator homogenizer (Ultra Turrax, IKA) before proceeding with the RNA extraction. The on-column RNase-free DNAse digestion was performed in all RNA isolations to prevent contamination with genomic DNA interfering with downstream applications. RNA was eluted in RNase-free ddH$_2$O.

4.3.2.2   Determination of RNA concentration via spectrophotometry

Concentrations of RNA solutions were initially determined using a NanoDrop ND-1000 spectrophotometer (Peqlab). From the measured absorption at the wavelengths of 260 nm and 280 nm the software calculated the RNA concentration and determined the 260 nm/280 nm ratio which is an indicator for RNA purity. A value of 2.0 is indicative of high purity. The determination of RNA concentrations with a standard spectrophotometer is insufficiently precise to allow reliable quantification of transcripts via real-time PCR. For quantitative downstream applications RNA concentrations need to be determined more accurately (4.3.2.3).

4.3.2.3   Determination of RNA concentration (Ribo-Green method)

Accurate determination of RNA concentrations was performed using the Quant-IT RiboGreen RNA assay (Life Technologies) as described in the manufacturer's instructions. This technique is based on the RiboGreen dye, which increases its fluorescence when bound to RNA. This allows RNA quantification that is unbiased by compounds absorbing at similar wavelengths. The assay was carried out in dark 96-well plates (#655076, Greiner) on a Safire² microplate reader (Tecan). RiboGreen allows absolute RNA quantification using an included RNA standard series ranging from 0 to 100 ng/µL. Therefore, the measured samples were prediluted to match the standard range. By fluorescence measurement of the standard series a standard curve was established by linear regression. The linear equation was used to determine absolute concentrations from fluorescence values obtained from samples.

4.3.3 Polymerase chain reaction

The polymerase chain reaction (PCR) was developed by Kary Banks Mullis in 1983 (Mullis KB 1986). PCR utilizes thermostable DNA polymerases to extend 3'-OH ends of DNA oligonucleotides specifically binding to a DNA matrix molecule. Primer extension leads to cyclic amplification of the template, as each extension product serves as a new template in the subsequent cycle. In this study PCR was a fundamental tool that many applications were based on. PCR was used for the genotyping of mice and for the quantification of transcripts from single stranded cDNA.

4.3.3.1 The standard PCR

For standard PCR, as applied for genotyping purposes the OneTaq® Quick-Load 2X Master Mix with Std.-Buffer (New England Biolabs) was used. A typical PCR setup on a 25 µL scale is shown in Table 15.

Table 15: Typical PCR setup: PCRs using the OneTaq® Quick-Load 2X Master Mix with Std.-Buffer (New England Biolabs) were routinely performed in a 25 µL scale.

component	amount
H_2O (ad 25 µL)	4.5 µL
fwd oligonucleotide (10 µM)	3 µL
rev1 oligonucleotide (10 µM)	2 µL
rev2 oligonucleotide (10 µM)	2 µL
OneTaq® Quick-Load	12.5 µL
template (2 – 200 ng)	1 µL

A starting point to assess performance of a PCR included $MgCl_2$ concentrations of 1.5 mM and primer concentrations of 0.4 µM. Amplification of targets that were difficult to amplify or that yielded unspecific products was enhanced by adaption of PCR conditions. Increasing the $MgCl_2$ concentration boosts polymerase performance on cost of primer binding specificity. Decreasing the $MgCl_2$ concentration can make primer binding very specific, but the amplification reaction might become very ineffective. Similar effects can be achieved by adjustment of the annealing temperature. Low temperatures cause primers to effectively bind the template but allow unspecific primer binding. High temperatures increase binding specificity but might also reduce the number of primers binding the template, thus decreasing PCR efficiency. The annealing temperature of a PCR program should be

adjusted according to the oligonucleotide properties. Melting temperatures of oligonucleotides were calculated using the OligoCalc web application as listed in 3.10.2. A typical PCR program is shown in Table 16.

Table 16: Standard PCR program: The usual PCR begins with an initial denaturation step melting the double stranded DNA template followed by 38 cycles of denaturation, annealing and extension. Finally, incomplete product are complemented for 10 min at 72°C. The annealing temperature varies between PCRs and depends on the oligonucleotide properties. The extension temperature is chosen according to the enzymes optimum temperature (i.e. 72°C for Taq polymerase) which may vary between enzymes. Extension time depends on the amplicon length and processing speed of the polymerase.

initial denaturation	5 min	95°C	
denaturation	30 sec	95°C	
annealing	30 sec	50 – 68°C	40 cycles
extension	~1 min/kb	72°C	
final extension	10 min	72°C	

4.3.3.2   Reverse Transcription

cDNA synthesis was performed using the QuantiTect Reverse Transcription kit (Qiagen) according to the manufacturers instructions. For quantitative real-time PCR the QuantiTect kit (Qiagen) was used exclusively. Prior to cDNA synthesis the RNA concentration was determined by the RiboGreen method (4.3.2.3). For quantitative real-time PCR 150 ng of RNA was reversely transcribed in a 10 µL setup. For generation of a standard series 600 ng of RNA was used in 20 µL.

4.3.3.3   Quantitative real-time PCR

Quantitative real-time PCR (qPCR) overcomes the limitations of semi-quantitative RT-PCRs. Even though it underlies the same reaction kinetics as any other PCR, template amounts can be robustly determined. In contrast to the semi-quantitative PCR, qPCR measures product amplification as it happens during exponential phase. In this study qPCRs were performed on the *Roche Light Cycler 1.5* using the *Light Cycler Fast Start DNA Master SYBR green I kit* (*Roche*) according to the manufacturer's instructions. The *SYBRgreen* I dye preferentially binds to DNA but also to RNA. Its absorption maximum is at 494 nm (blue). When excited *SYBRgreen* emits green light (521 nm). The fluorescence is strongest when bound to double stranded DNA but is much weaker when bound to single stranded DNA or RNA. After each primer extension step of a qPCR, *SYBRgreen* fluorescence is measured

at 80°C. At this temperature double stranded DNA caused by primer dimmers or cDNA hairpins is denatured but longer PCR products are stable allowing a precise determination of PCR product amounts in every PCR cycle. As *SYBRgreen* binds double stranded DNA independently of the sequence, all PCR products including unspecific side products are measured. Therefore, specific product amplification is vital for *SYBRgreen*-based systems. Product specificity was surveyed by dissociation curve analysis and subsequent agarose gel electrophoresis. All qPCR primers used in this study amplify their target specifically at the indicated conditions (3.9.2). For use as a template for qPCR, cDNA was produced as described in 4.3.3.2. The template solution was generated by diluting cDNA 1:5 in TE^{-4} buffer (e.g 8 µL of cDNA (from 150 ng RNA in 10 µL) + 32 µL of TE^{-4}). A standard series was generated from a 600 ng RNA reverse transcription reaction as shown in Table 17.

Table 17: Dilution of a cDNA standard series for qPCR: cDNA was diluted 1:2.5 in TE^{-4} buffer to generate templates with different concentrations ranging from 64 (i.e. 64/64) to 1 (i.e. 1/64 of the starting cDNA concentration)

Standard sample	cDNA	diluent
standard 64 (1:2.5)	16 µL cDNA (from 600 ng RNA in 20 µL)	24 µL TE^{-4}
standard 32 (1:5)	20 µL standard 64	20 µL TE^{-4}
standard 16 (1:10)	20 µL standard 32	20 µL TE^{-4}
standard 8 (1:20)	20 µL standard 16	20 µL TE^{-4}
standard 4 (1:40)	20 µL standard 8	20 µL TE^{-4}
standard 2 (1:80)	20 µL standard 4	20 µL TE^{-4}
standard 1 (1:160)	20 µL standard 2	20 µL TE^{-4}

The cycle threshold of each standard concentration was plotted against the concentraton (log) and the standard curve was extrapolated by linear regression. This curve was then reversely used to calculate the concentrations of samples from their respective cycle threshold value. Samples were measured as duplicates and averaged using the arithmetic mean. For a 10 µL qPCR setup 3 µL of template solution were used. The composition of a typical qPCR is shown in Table 18.

Table 18: Typical qPCR setup for the Roche LightCycler 1.5.: qPCRs in Roche Light Cycler 1.5 using the SYBRgreen I Master Mix were performed in a 10 µL scale. H_2O, $MgCl_2$ solution, SYBRgreen Master Mix and Fast Start enzyme were provided in the kit. A $MgCl_2$ concentration of 3 mM was suitable for all applications.

component	amount
H_2O (ad 10 µL)	2.8 µL
$MgCl_2$ (25 mM)	1.2 µL (3 mM)
fwd oligonucleotide (10 µM)	1 µL
rev oligonucleotide (10 µM)	1 µL
SYBRgreen Master Mix	0.833 µL
LC Fast Start Enzyme	0.166 µL
diluted cDNA template	3 µL

4.3.4 Agarose gel electrophoresis

DNA fragments of different sizes were separated by agarose gel-electrophoresis for analytical purposes. Different concentrations of agarose (e.g. 1% – 2%) were used according to the size of DNA fragments to analyze. Before loading, the gel was chilled to 4°C to become fully solid. For preparation agarose was melted in TBE buffer and supplemented with ethidium bromide (1:10,000). This allowed visualization of DNA when exposed to UV-light. DNA samples were transferred to the gel and separated at 100 to 125 Volts depending on the gel size and agarose concentration. Results were documented using the *ChemiDoc XRS* documentation system (*BioRAD*).

4.4 PROTEINBIOCHEMISTRY

4.4.1 Extraction of proteins

Proteins were generally isolated in RIPA buffer (*Sigma-Aldrich*) containing a mix of

protease inhibitors (*Complete Mini Protease Inhibitors, Roche*). One tablet of protease inhibitors was resolved in 10 mL of RIPA buffer. All isolation steps were carried out at 4°C and proteins were stored at -80°C.

4.4.1.1   Extraction of proteins from tissues

Lysis and protein extraction from animal tissues requires additional steps for efficient tissue break up and lysis. To obtain protein from organs (e.g. brain, liver, lung, spinal cord or TVA

muscle) the tissue was homogenized in RIPA buffer containing protease inhibitors using a homogenizer (Precellys 24, Peqlab, program 4). Depending on tissue size 200 to 400 µL of RIPA buffer was used. Tissues with high protein content (e.g. brain) generally required a larger lysis volume. For effective lysis the homogenate was incubated on ice for 10 min. Next, the samples were centrifuged for 20 min at 13200 rpm and 4°C to remove cell debris and the supernatant was transferred to new Eppendorf tubes. For further homogenation, the lysates were put into a ultrasonic bath for additional 5 min. Afterwards the samples were again centrifuged for 20 min at 13200 rpm and 4°C and transferred to new Eppendorf tubes. Isolated proteins were snap-frozen in liquid nitrogen and stored at -80°C.

4.4.1.2   Determination of protein concentration via Bradford protein assay

Protein concentrations were determined using the protein assay according to Bradford (Compton and Jones 1985). The Bradford reagent contains the dye Coomassie-Brilliant-Blue G-250, which forms complexes with cationic and nonpolar amino acids in acidic environment. This stabilizes the dye in its non protonated form which causes a shift of light absorbance maximum from 470 to 595 nm. 1 µL of protein lysate was mixed with 499 µL of Bradford reagent (*Applichem*) and incubated at room temperature for 10 min. The concentration was determined by measuring the absorption at 595 nm on a standard spectrophotometer (*Eppendorf*) using a standard of 0.5 to 5.0 µg of BSA for calibration.

4.4.2 Discontinuous SDS-Page

During SDS-PAGE (*sodium dodecyl sulfate polyacrylamide gel-electrophoresis*) proteins are resolved according to their molecular weight within an electric field. Proteins of different size or molecular weight proceed through the polyacrylamide gel with different velocities. Furthermore, the anionic detergent SDS is applied which adapts the mass to charge ratio of proteins. Proteins become negatively charged and their speed in the gel is almost exclusively determined by their mass. SDS also denatures secondary and tertiary structures. Thus proteins of similar mass proceed towards the anode at same velocities without being impaired by their innate conformation. Hydrogen- and disulfide-bonds are severed due to boiling in presence of reducing compounds like dithiothreitol or β-Mercaptoethanol (Laemmli 1970). In this study discontinuous SDS-PAGEs were carried out with 4% stacking gel and a 12% resolving gel used to separate most target proteins. Discontinuous SDS-PAGE allows proteins to focus in a sharp band within the stacking gel and to simultaneously start resolving in the resolving gel. This effect is based on a discontinuous buffer system with low pH of 6.8

in the stacking gel and higher pH of 8.8 in the resolving gel. Proteins traveling through the stacking gel have the same charge and their speed is hardly biased by their size, as the gel matrix is insufficiently dense (4%). In the stacking gel proteins are focused between two ion fronts: The quickly moving Cl$^-$ and the slowly moving glycine which has its isoelectric point *pI* at 5.97 and therefore close to pH 6.8. As the ion front approaches the resolving gel (pH 8.8) glycin overtakes the proteins which are then no longer focused and resolve according to their size caused by interaction effects with the dense gel matrix. SDS gels were prepared between two vertical glass plates. First, the resolving gel (3.5) was prepared and isopropanol was pipetted on top to produce a sharp edge. After polymerization was complete, isopropanol was removed and the stacking gel (3.5) was poured on top. The total protein concentration of lysates was determined according to Bradford (4.4.1.2). 10 to 20 µg of total protein were supplemented with 1 volume of 2x SDS sample buffer and boiled for 5 min before being loaded onto the gel. As a protein ladder 10 µL of the *PageRuler™ Prestained Protein Ladder* (*Thermo*) were loaded. Electrophoresis was performed at low initial voltage of 80 Volts while proteins were moving through the stacking gel. Voltage was increased up to 180 Volts while resolving.

4.4.3 Transfer of proteins to PVDF blotting membranes

Proteins that have been resolved by SDS-PAGE (4.4.2) were electrophoretically transferred to PVDF (polyvinylidene fluoride) blotting-membranes. All transfers have been performed via wet-blot (tank–blot) according to Towbin (Towbin et al. 1979). Protein transfer was carried out at 4°C for 2 h at 100 Volts or over night at 30 Volts. Successful transfer of proteins could be recognized due to pre-stained protein ladders that were visible on the blotting membrane.

4.4.4 Immunostaining of proteins on PVDF membranes

The immunoblot or Western Blot utilizes antibodies to specifically detect proteins. Primary antibodies specifically bind epitopes of the target protein. The primary antibody is then detected by secondary antibodies which are conjugated to HRP (horseradish peroxidase). The desired protein can finally be detected by chemiluminescence using *Super Signal West Pico ECL Substrate* (*Thermo*). This substrate contains H_2O_2 and luminol. As HRP cleaves H_2O_2, luminol will luminesce. After blotting (4.4.3) the membrane was shortly washed in TBST and blocked with 6% milk powder in TBST at 4°C for 2 h or o. n.. Primary antibodies

were applied in TBST with 2% milk powder and incubated at 4°C. Concentration and the duration of incubation time for each antibody are stated in 3.8.1. The membrane was washed 5 times for 5 min in TBST to remove non-bound antibodies. The secondary antibody was applied in TBST with 2% milk powder at concentrations indicated in 3.8.2. All secondary antibodies used for immunoblots were HRP-conjugates. To remove non-bound secondary antibody the membrane was washed 5 times for 5 min in TBST. To visualize the protein of interest the membrane was incubated for 5 min in chemiluminiscence substrate. Results were recorded using the *ChemiDoc XRS* system (*BioRAD*). Densitometric analysis was performed using the *QuantityOne* Software (*BioRAD*) or *ImageJ* (3.10.1).

4.4.5 Restoring of PVDF membranes for re-blotting

For repeated immunological detection of proteins on previously used PVDF membranes bound antibodies were removed by shaking the membrane for 7 to 15 min in *Restore Western Blot Stripping Buffer* (*Thermo*). Afterwards, the membrane was washed twice in TBST before proceeding with a new immunostaining.

4.5   HISTOLOGICAL METHODS

In this study hearts, intestine, lung, TVA muscle and s. c. of SMA, SMA-*PLS3*het, SMA-*PLS3*hom, HET, HET-*PLS3*het, HET-PLS3hom and WT mice were histologically analyzed at various developmental stages.

4.5.1 Histological preparation of animal tissues

4.5.1.1   Paraffin-embedding of mouse tissues

Hearts, lungs and intestines were isolated from mice at P21. Preparation of the specimen for micro-dissection included fully automated dehydration and paraffin embedding using a tissue processor (*TP1028, Leica*). After micro-dissection, paraffin sections were flattened in a water bath and dried o. n. at 37°C. The following Haematoxylin/Eosin staining is described in section 4.5.2.

4.5.1.2   Cryo-embedding of mouse tissues

For proprioceptive input staining, the spinal cords of P21 mice were dissected from euthanized mice and fixed in 4% paraformaldehyde (PFA)/PBS for 1 day. The lumbar L4 – L5 region was quickly rinsed in PBS, embedded in tissue-freezing medium (Jung) after cryoprotection (first day – 20% sucrose; second day – 30% sucrose) and sliced into 40-mm-thick sections (cryostat, Leica). The following immunostaining is described in section 4.5.3.

4.5.2   *Haematoxylin/Eosin staining of paraffin-embedded slices*

HE staining (haematoxylin and eosin staining) was used as an initial standard staining procedure to allow gross histological analysis. Upon HE staining nuclei are stained dark blue while most parts of the cytoplasm (i.e. proteins) are stained red to pink. Paraffin-embedded sections were first deparaffinized for 2 x 15 min in xylene and rehydrated in a series of EtOH solutions of decreasing concentrations (each 2 min in 100% EtOH, 96% EtOH, and 70% EtOH). Sections were shortly washed in PBS and H_2O. Staining with haematoxylin was performed for 6 min. Specimens were shortly rinsed in water and then washed for 15 min in fresh water. Finally, sections were shortly rinsed in ddH_2O. Eosin staining was performed for 1 min before shortly washing in H_2O. At the end specimens were dehydrated with an EtOH series of increasing concentration (each 1 min in 70% EtOH, 96% EtOH and 100% EtOH). For sample preparation sections were incubated for 1 min in xylene and mounted with *Eukitt* mounting medium.

4.5.3   *Immunostaining of NMJs from TVA and cryo-embedded spinal cord sections*

For NMJ staining, TVA muscle was fixed in 4% PFA for 20 min. The tissue was rinsed three times in PBS for 10 min so that excess PFA would be removed. From this step on, the staining protocol followed the procedure described below for MN staining. Primary antibody dilutions were mouse α-SV2 together with mouse α-NF. The secondary antibody was donkey α-mouse Alexa fluor 488. To outline endplates in muscle tissue, BTX conjugated with Rhodamine (1.5 ng/mL, Invitrogen) was used. Samples were permeabilized and blocked in PBS containing 4% BSA, 1% Triton X-100, and PBS for 1 h. Finally, samples were incubated with goat α-ChAT and rabbit α-VGLUT1 antibodies or goat α-Plexin and mouse α-Smi32 (o. n.). Samples were washed and incubated with secondary antibodies (donkey α-rabbit Alexa fluor 488 and donkey α-goat Alexa fluor 568). Samples were

mounted in Mowiol (Kuraray) for further analysis. All dilution and conditions for primary and secondary antibodies are listed in section 3.8.1 and 3.8.2.

4.5.4 Microscopy

Paraffin-embedded organ sections were microscopically analyzed. Images were recorded on a Zeiss AXIO microscope and the Zeiss M2 imaging system using the ZEN software (Zeiss, Jena, Germany). Routinely, whole mount overview images were taken using 1.25x magnification. For high resolution analysis multiple images have been taken to finally cover the whole sample using 10x magnification. Images were merged and blended using the Demo version of the Autostitch software. Overlap of image recording at the microscope allowed perfect panoramic assembly of single images. Images used for organ analysis that are shown in this work are high resolution panoramic assemblies consisting of multiple 10x magnification shots. Imaging of NMJs was performed with a Zeiss microscope (Axio Imager.M2) with the Apotome.2 system to mimic confocality together with a 40x and 63x oil immersion objective lens with 1.4 NA. Images of MN soma and proprioceptive inputs were taken with the META 510 confocal microscope (Zeiss). Z-stacks of 50 – 60 slices at a 0.5 µm interval were created with ZEN software (Zeiss). Proprioceptive input numbers on MNs and MN soma size were quantified with ImageJ (Fiji) software. By creating 3D regions of interest (ROIs) of the selected MN soma the macro 'CountAxonalInputsV21.ijm' is able to measure the exact soma size and in addition detects and quantifies the proprioceptive inputs per MN. Each image was split into two channels: one for ChAT positive MN soma and another for VGlut1 positive inputs and ensured that voxels were isometric. Subsequently, both single-channel images were smoothed: in the MN soma image each pixel was replaced with the median of its 6x6x4 neighborhood and an optional automatic background removal was performed by Li's Minimum Cross Entropy thresholding method (Li and Tam 1998). In the VGlut1 positive image each pixel was replaced with the median of its 16x16x16 neighborhood. In the smoothed VGlut1 positive image the inputs were automatically segmented using the 3D simple segmentation function of the 3D ImageJ Suite (Ollion et al. 2013) under the following criteria: the intensity threshold was obtained from Otsu's threshold clustering algorithm applied to the stack histogram (Otsu 1979) and 20 voxel were used as a minimum size criterion. In smoothed ChAT positive images the experimenter draws the smallest possible cuboids around non-overlapping MN soma. Within the cuboid further segmentation was performed automatically using the Otsu method to obtain input values for

a 3D hysteresis thresholding (3D ImageJ suite). The resulting mask was dilated by 4 voxels and finally holes in the mask were filled. Once all suitable MN somas within an image were selected, the macro processed each 3D selection, again using functions of the 3D ImageJ suite, so that it first quantified all VGlut1 inputs within the selection and then calculated only those relevant for a given MN soma within 2 µm distance. Additionally, the area of each MN soma was determined. More detailed functions and information of the macro are given in the appendix. All experiments were double blinded.

4.6 ELECTROPHYSIOLOGICAL ANALYSES (PERFORMED BY DR. LAURA TORRES BENITO)

4.6.1 FM1-43 Endocytosis Experiments

TVA was dissected in HBSS solution (14025, GIBCO) and afterwards incubated for 20 min in external physiological solution containing the following (mM): 145 NaCl, 5 KCl, 10 HEPES, 2 $CaCl_2$, 1 $MgCl_2$, and 10 glucose. The N. intercostalis innervating the TVA muscle was stimulated via a suction electrode pulled from borosilicate glass tubes and mounted in a bipolar electrode holder connected to a universal stimulus isolator and a universal digital stimulator. Contraction of the muscles upon nerve stimulation was checked visually under the microscope. After incubation with 3 mM FM1-43, we applied a current pulse train either at 20 Hz or 5 Hz for 1 s (1 mA amplitude, 0.5 ms pulse duration) to load the endocyted synaptic vesicles. Subsequently, we washed muscles with external solution that did not contain $CaCl_2$ or 3 mM $MgCl_2$ but did contain ADVASEP-7 to efficiently remove the non-internalized FM1-43, and we fixed the muscles with 4% PFA. We also incubated TVA muscles with BTX- 647 (1 ng/mL; B-35450, Life Technologies) to stain postsynaptic terminals and easily localize the NMJs, then mounted them on slides. We used three animals per genotype and stimulation set. Imaging was performed as described in section 4.5.4. All imaging processes and analyses were blinded. We analyzed images with Fiji on a macro setting and applied the Li threshold method to the postsynaptic terminals to delineate the area of interest in the presynaptic site. Because at P10 the distribution of vesicles is quite homogenous along the NMJ, we quantified the mean intensity of the FM1-43 dye at the presynaptic terminal, which excluded possible variability due to the size.

4.7 STATISTICAL ANALYSES

Data obtained in this study was generally undertaken to statistical evaluation to analyze the technical error of a measurement or to determine the significant difference between groups of biological replicates. All statistical analyses were carried out using *Excel 2010/2013* (Microsoft) and GraphPad Prism (GraphPad Software). Some measurements were recorded as duplicates (e.g. qRT-PCR, Light Cycler 1.5, n = 2) or triplicates (RiboGreen method of determining the RNA concentration, n = 3) to allow calculation of the mean to minimize the technical error caused by device inaccuracies or inaccurate pipetting. To assess biologically significant differences, groups of biological replicates (e.g. mice, organs or cells of a specific genotype) were compared to each other. N gives the number of biological replicates; i.e. the number of individuals per group observed. The average of each group was calculated by the arithmetic mean, while the dispersion of readout values within a group was represented by the standard error of the mean (SEM). Error bars within bar charts represent the SEM unless indicated otherwise. *Student's t-Test* was employed to determine the statistical significant difference between groups. The probabilities for data points belonging to different groups are 0.05 (*), 0.01 (**) or 0.001 (***). Lok-rank (Mantel-Cox) test was performed for survival statistics.

5. Results

Previous data of our laboratory have shown that ubiquitous overexpression of one PLS3 transgenic allele in the severe Taiwanese SMA mouse model restores MN and NMJ function as well as motoric abilities but fails to rescue survival, most likely because of a dramatic multi-organ dysfunction that could not be rescued by PLS3 overexpression (Ackermann et al. 2013). Therefore the major aim of this study was to generate a SMN-ASO-induced milder SMA mouse model to confirm the beneficial impact of PLS3 as observed in humans.

5.1 ANALYSES OF UNINJECTED SMA-*PLS3*HOM MICE

First, the PLS3 transgenic allele (Ackermann et al. 2013) was crossed into the Taiwanese SMA mouse strain (Riessland et al. 2010). Next, a SMA mouse ($Smn^{KO/KO}$;$SMN2^{tg/0}$) overexpressing PLS3 (here named SMA-*PLS3*het for $Smn^{KO/KO}$;$SMN2^{tg/0}$;$PLS3^{tg/0}$ and SMA-*PLS3*hom for $Smn^{KO/KO}$;$SMN2^{tg/0}$;$PLS3^{tg/tg}$) was generated, as well as Smn heterozygous mice (here named HET for $Smn^{KO/WT}$;$SMN2^{tg/0}$) overexpressing PLS3 (HET-*PLS3*het for $Smn^{KO/WT}$;$SMN2^{tg/0}$;$PLS3^{tg/0}$ and HET-*PLS3*hom for $Smn^{KO/WT}$;$SMN2^{tg/0}$;$PLS3^{tg/tg}$). HET mice were used as controls. The breeding scheme is shown in Figure 10 (Material and Metods: Chapter 4.1.2). To better understand whether the amount of PLS3 that is overexpressed in SMA mice influences the survival rate, weight progression, and motoric abilities in SMA mice (C57BL/6N), uninjected SMA-*PLS3*het and SMA-*PLS3*hom mice were compared in a first approach. This experiment was performed to verify whether homozygous PLS3 may act as a protective modifier and rescues the mouse phenotype including the survival rate in comparison to uninjected SMA and SMA-*PLS3*het mice (Ackermann et al. 2013). HET-*PLS3*het and HET-*PLS3*hom mice were used as internal control groups for this study.

5.1.1 Survival rate and weight progression

The comparison of the survival rate of SMA-*PLS3*hom mice (12.95 ± 3.26 days) with SMA-*PLS3*het mice (11.67 ± 3.78 days) showed no significant difference (Figure 12). The same was true for their weight progression (Figure 13). We thus concluded that elevated PLS3

expression alone on the severe SMA background is unable to overcome the multi-organ impairment found in the severe SMA mouse model (Ackermann et al. 2013).
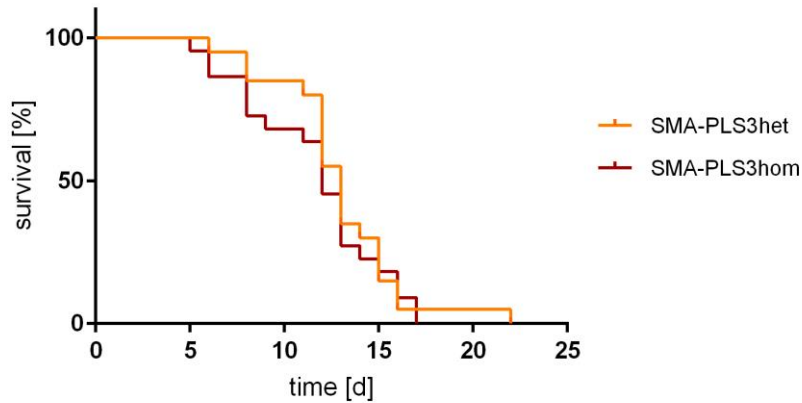
Figure 12: Kaplan-Meier curves show the survival rate of untreated SMA-*PLS3*het and SMA-*PLS3*hom mice. There is no significant difference in the survival between these two groups: 12.95 ± 3.26 days for SMA-*PLS3*het (n = 20) and 11.67 ± 3.78 days for SMA-*PLS3*hom mice (n = 22). A log-rank (Mantel-Cox) test was used.
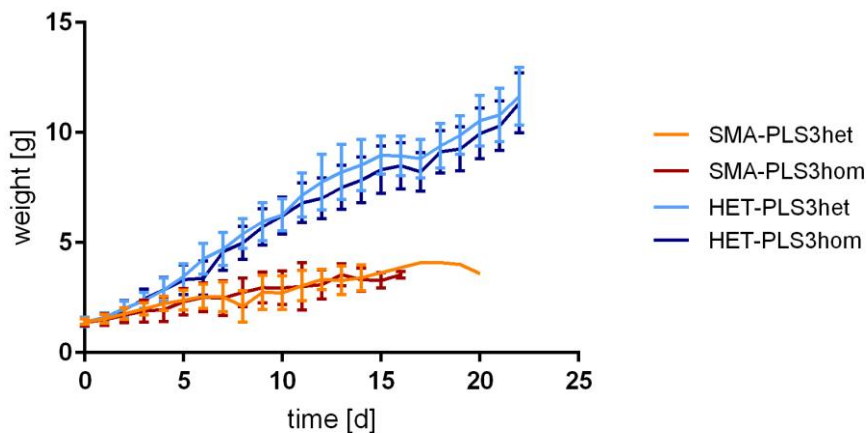
Figure 13: Weight progression of uninjected SMA and HET mice overexpressing PLS3 on C57BL/6N background: SMA-*PLS3*het (n = 20) and SMA-*PLS3*hom (n = 22) mice in comparison to HET-*PLS3*het (n = 32) and HET-*PLS3*hom mice (n = 26).

5.1.2 *Motoric ability*

To investigate whether the homozygous PLS3 overexpression led to any improvements considering the motoric functions of these severely affected SMA mice, tube and righting tests were performed. Unfortunately, also the motoric ability of SMA-*PLS3*hom vs. SMA-*PLS3*het mice did not show any significant difference in the tube test (Figure 14) or in the righting reflex test (Figure 15). The two motoric tests were carried out as reported in section 4.1.7.
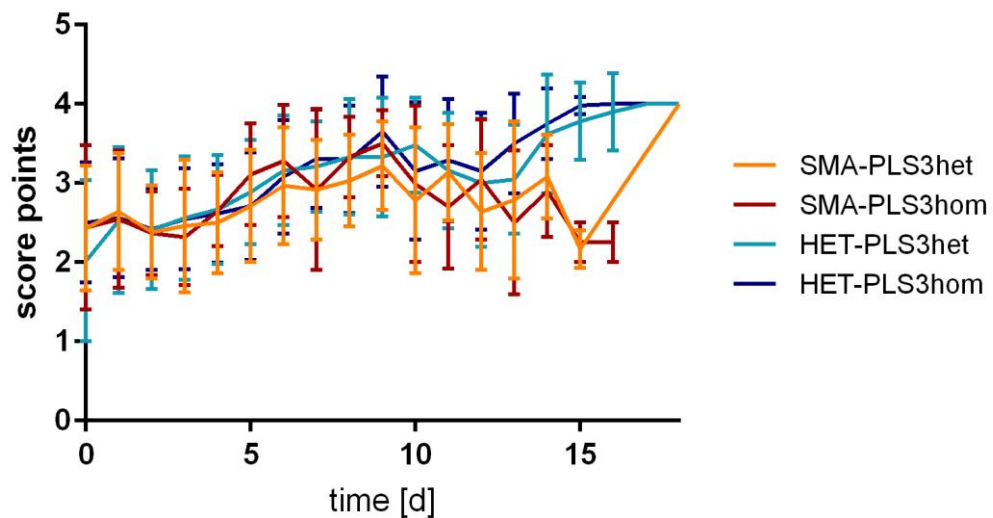
Figure 14: Tube test of SMA and HET mice overexpressing PLS3 on C57BL/6N background. SMA-*PLS3*hom (n = 22) mice show no significant difference to SMA-*PLS3*het mice (n = 20) in performance.
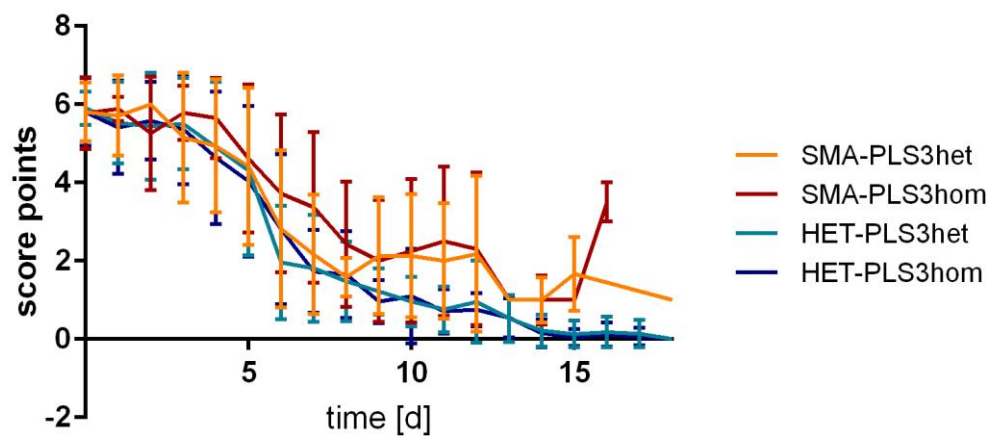
Figure 15: Righting reflex test of SMA and HET mice overexpressing PLS3 on C57BL/6N background. SMA-*PLS3*hom (n = 22) mice show no significant difference to SMA-*PLS3*het mice (n = 20) in performance.

These findings induced the idea to generate and establish an intermediate SMA mouse model which resembles more the human condition in asymptomatic *SMN1*-deleted individuals overexpressing PLS3 (Oprea et al. 2008) as the severely affected Taiwanese SMA mouse model is suffering from intense multi-organ dysfunction that was not rescued by increased PLS3 overexpression and therefore the protective role of this disease modifier could neither lead to a survival rescue nor to fully restored motoric abilities in SMA-*PLS3*hom mice. We therefore decided to generate a milder SMA model that reflects the human situation in asymptomatic discordant families in order to finally prove that PLS3 overexpression has beneficial effects, including prolonged survival. For this, a combinatorial therapy of low-dose SMN antisense oligonucleotide (ASO) and PLS3 overexpression was applied.

5.2 PROTEIN EXPRESSION STUDIES IN SMA-*PLS3*HET VS. SMA-*PLS3*HOM UNINJECTED MICE

To verify the expression of PLS3, Western blot analyses of spinal cord, brain, gastrocnemius, transverse abdominis, lung and skin were performed in HET-*PLS3*het and HET-*PLS3*hom mice. The isolation of the organs was done at P10 as described in section 4.4.1. In all analysed tissues there was a significant increase in the PLS3 overexpression in HET-*PLS3*hom mice with spinal cord, brain and gastrocnemius having the highest increases (Figure 16 and Figure 17). The WB analyses were performed as described in section 4.4.2 to 4.4.4. The PLS3 overexpression increase in HET-*PLS3*hom relative to expression levels in HET-*PLS3*het is as followed: spinal cord: 51.14%; brain: 47.11%; gastrocnemius: 57.37%; transverse abdominis: 42.92%; lung: 45.07% and skin: 38.11%.
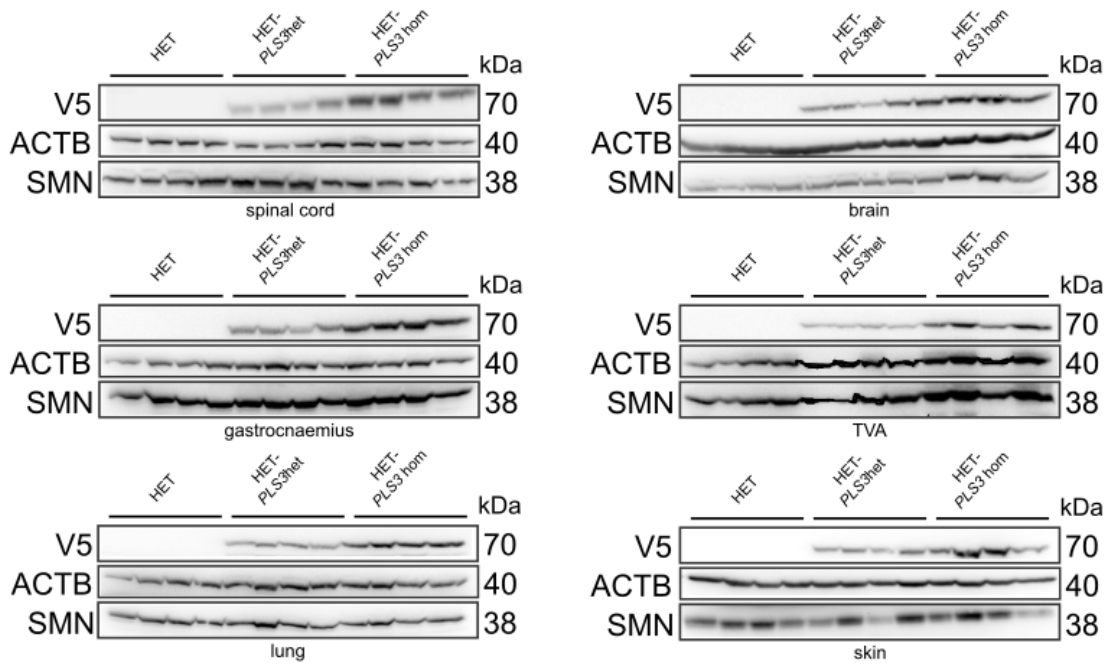
Figure 16: WB analyses of PLS3 transgene expression of P10 mouse protein lysates of spinal cord, brain, gastrocnemius, transverse abdominis, lung and skin of uninjected HET-*PLS3*het and HET-*PLS3*hom mice (N = 4). V5 staining labels only PLS3 transgene. ACTB was used as a loading control.
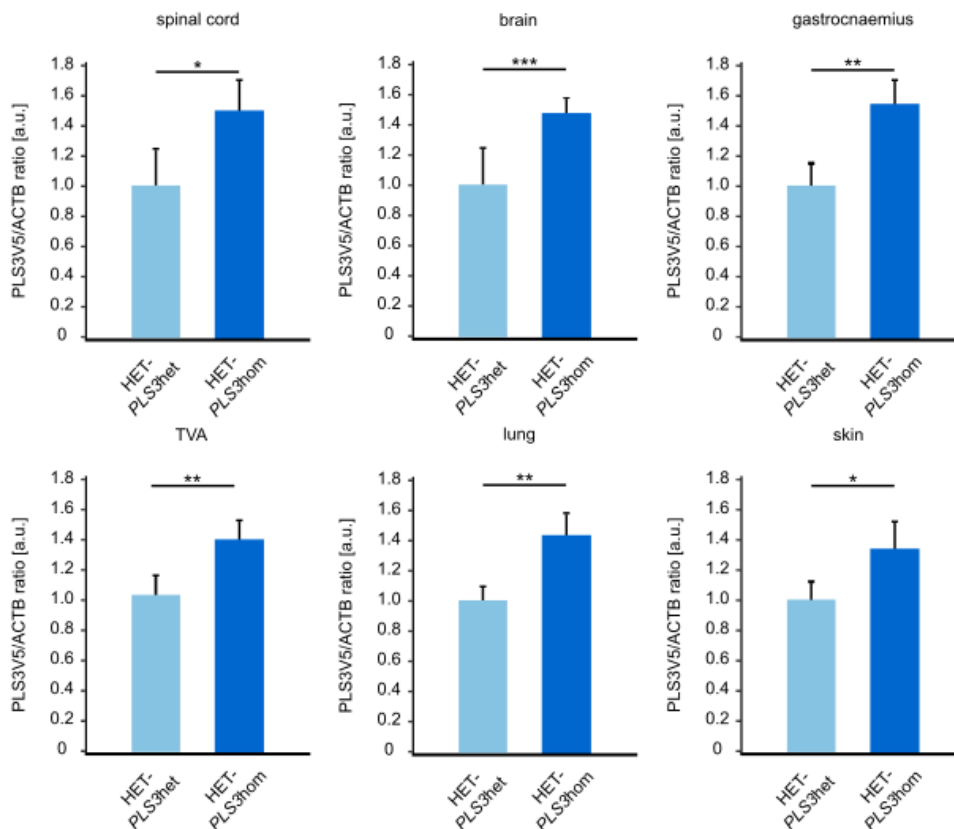
Figure 17: Quantification of PLS3 transgene expression in heterogenous and homogenous P10 mice. Increase of PLS3 in HET-*PLS3*hom relative to expression levels in HET-*PLS3*het mice: spinal cord.: 51.14%; brain: 47.11%; gastrocnaemius: 57.37%; TVA: 42.92%. lung: 45.07%; skin: 38.11%; N = 4; * p < 0.05; ** p < 0.01; *** p < 0.001, two-tailed Student's t test. Error bars represent SD.

5.3   OPTIMIZATION AND DOSAGE FINDING OF SMN-ASO INJECTION

SMN-ASOs correct *SMN2* splicing by blocking an intronic splice silencer and thus prevent binding of the splice factor hnRNPA1 which promotes exon 7 skipping (Rigo et al. 2012). Consequently, SMN-ASOs facilitate exon 7 inclusion and are stable up to 6 months. Pre-symptomatic intracerebroventricularly (ICV) and subcutaneously (s.c.) injection of high doses of ASO (up to 160 µg twice) fully rescues the SMA phenotype (Hua et al. 2011). Accordingly, we decided to subcutaneously inject low doses of 10 – 50 µg of SMN-ASO on P2 and P3 in SMA mice on a congenic FVB/N background in order to produce an intermediate SMA mouse model. The observed survival rate varied quiet dramatically at each dose (Figure 18), making an efficient analysis of the modifier later one rather problematic. Instead, using the same injection scheme in SMA mice on a congenic C57BL/6N background turned out to vary by far less (Figure 19). Because 40 and 50 µg were shown to prolong survival too much, the analysis was restricted to SMA mice injected with 10, 20, and 30 µg SMN-ASO and survival was compared to that of uninjected and control (ctrl)-ASO-injected mice (Figure 19). Injection of 30 µg SMN-ASO on P2 and P3 was chosen as an adequate dosage for generating of an intermediate SMA mouse model surviving approximately four weeks (26 ± 9.48 days). This observation emphasizes the relevance of the genetic background influencing the disease phenotype.
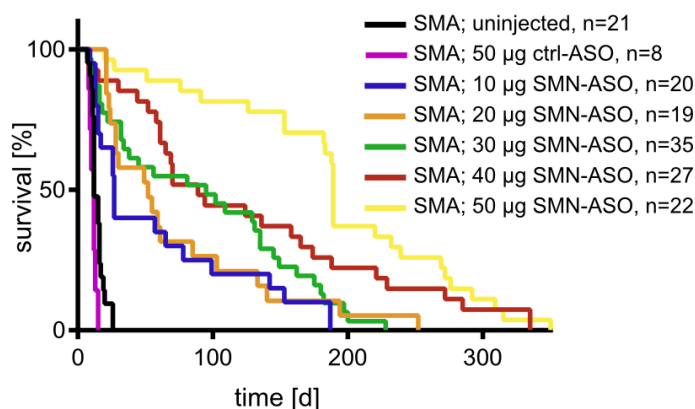
Figure 18: Optimization and dosage finding of SMN-ASO injection in SMA mice on a congenic FVB/N background: Kaplan-Meier curves show survival in SMA mice injected subcutaneously with 10 to 50 µg of SMN-ASO or 50 µg ctrl-ASO at P2 and P3. Notably is the large variability in survival in comparison to SMA mice of the same genotype on C57BL/6N congenic background (Figure 19). The mean age of survival was: 59.80 ± 60.79 days, n = 20 for 10 µg; 72.58 ± 65.15 days, n = 19 for 20 µg; 102.41 ± 73.91 days, n = 35 for 30 µg; 126.52 ± 98.58 days, n = 27 for 40 µg and 192.05 ± 97.50 days, n = 22 for 50 µg SMN-ASO in comparison to 14.57 ± 4.99 days, n = 21 uninjected and 11.13 ± 2.30 days, n = 8 ctrl-ASO injected mice. (Taken from (Hosseinibarkooie et al. 2016).)
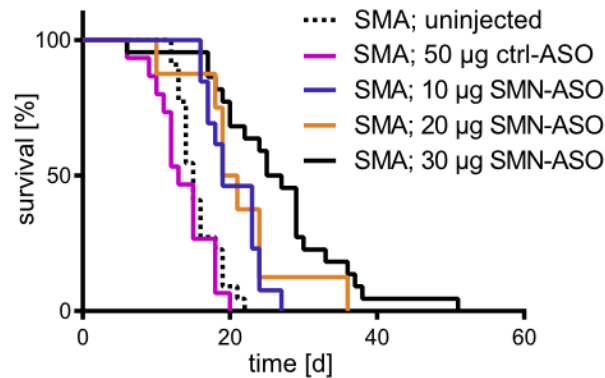
Figure 19: Optimization and dosage finding of SMN-ASO injection in SMA mice on a congenic C57BL/6N background: Kaplan-Meier curves show the survival rate of SMA mice injected at P2 and P3 with different SMN-ASO doses. Uninjected: 16 ± 2.85 days, n =22. 50 µg ctrl-ASO: 14 ± 3.89 days, n = 15. 10 µg SMN-ASO: 21 ± 3.95 days, n = 11. 20 µg SMN-ASO: 21 ± 7.37 days, n = 8. 30 µg SMN-ASO: 26 ± 9.48 days, n = 22. (Taken from (Hosseinibarkooie et al. 2016).)

Only some phenotypic analyses were carried out with mice on FVB background. These include: survival, weight progression, tube and righting test and showed large variability and too strong improvement under SMN-ASO therapy and therefore we doubted that the effect of PLS3 will be reliably seen. Therefore all main experiments of this study were performed with SMA mice on a C57BL/6N background to reliably dissect the modifying effect of PLS3. All pups were injected subcutaneously with 30 µg SMN-ASO at P2 and P3.

5.4   PLS3 OVEREXPRESSION RESCUES SURVIVAL ON A SMN-ASO INDUCED INTERMEDIATE SMA MOUSE MODEL

Strikingly, more than 60% of SMA-*PLS3*hom mice survived >250 days, and 30% were still alive at >400 days (mean survival: 219 ± 176.78 days). SMA*PLS3*het mice showed a less prolonged survival (169 ± 176.11 days), reflecting a PLS3-dependent dosage effect (Figure 20).
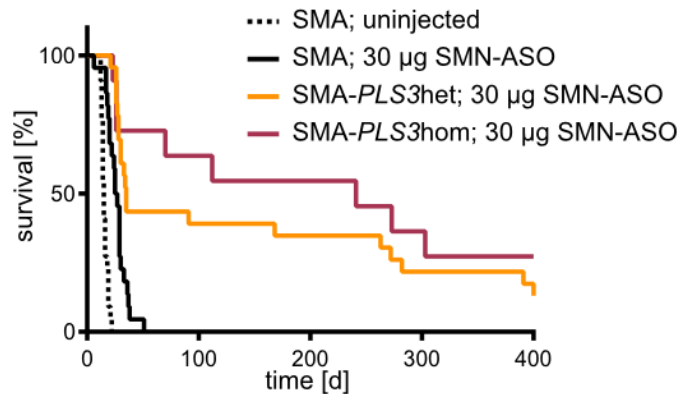
Figure 20: Kaplan-Meier curves show the survival rate of PLS3-overexpressing or –non-overexpressing SMA mice treated with 30 µg of SMN-ASO at P2 and P3. PLS3 overexpression drastically increased the survival to 169 ± 176.11 days (n = 23) for SMA-*PLS3*het and to 219 ± 176.78 days (n = 11) for SMA-*PLS3*hom in comparison to SMA mice without PLS3 overexpression. A log-rank (Mantel-Cox) test was used. The four groups of mice differ from each other highly significantly (p value < 0.001). (Taken from (Hosseinibarkooie et al. 2016).)

SMA-*PLS3*het and SMA-*PLS3*hom mice developed ear and tail necrosis over time, starting from one month of age (Figure 21, right part), in similarity to Smn[KO/KO];SMN2[tg/tg] mice (Hsieh-Li et al. 2000). Additionally, these animals showed normal behaviour in feeding and grooming.
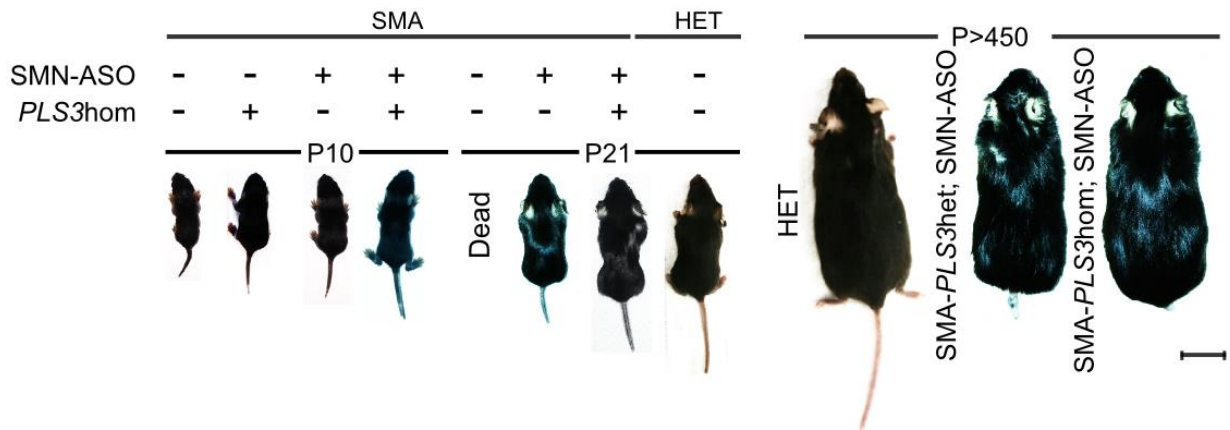
Figure 21: PLS3 overexpression improved phenotypical development in the intermediate SMA mouse model, similar to results for HET mice. The scale bar represents 2 cm. (Taken from (Hosseinibarkooie et al. 2016).)

5.5 WEIGHT PROGRESSION STUDIES

SMA-*PLS3*het and SMA-*PLS3*hom mice on C57BL/6N background continuously gained weight within the observed period of time (Figure 22). Although SMA-*PLS3*hom mice were slightly heavier than SMA-*PLS3*het mice, they did not reach the body weight of HET mice.
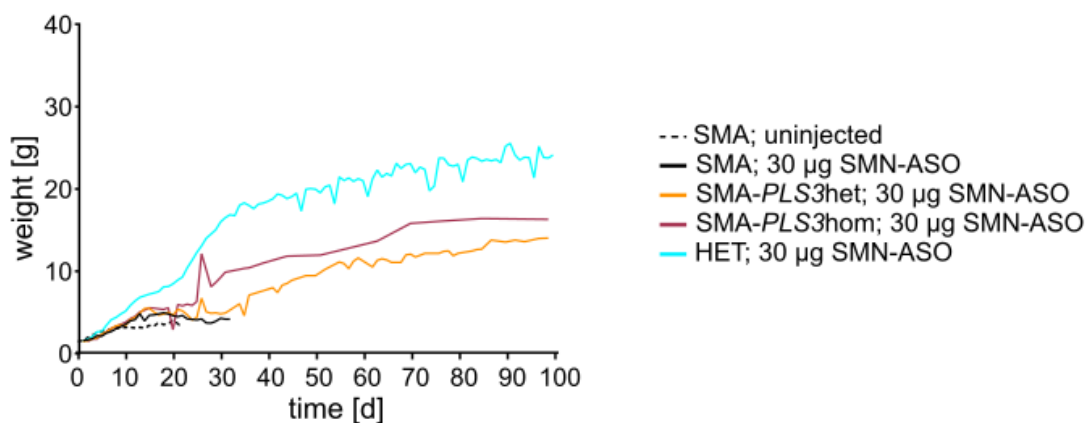
Figure 22: Weight progression (C57BL/6N) of SMA (uninjected, n = 22), and SMN-ASO injected SMA (n = 19), SMA-*PLS3*het (n = 10) and SMA-*PLS3*hom (n = 11) mice in comparison to HET (n = 18) mice (Modified from (Hosseinibarkooie et al. 2016)).

In comparison to the weight progression on C57BL/6N background, the mice on FVB/N background lived much longer after being injected with 30 µg SMN-ASO at P2 and P3. The

weight progression analysis (Figure 23) showed no significant difference between SMA and SMA-*PLS3*het mice and was more similar to the control groups (HET and HET-*PLS3*het).
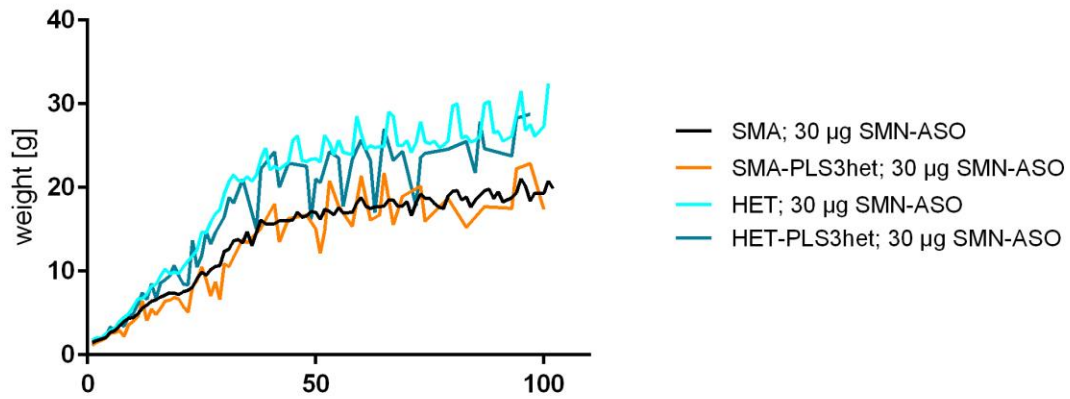
Figure 23: Weight progression (FVB/N) of SMN-ASO treated SMA (n = 29), SMA-*PLS3*het (n = 12), HET (n = 26), and HET-*PLS3*het (n = 11) mice.

5.6   Motoric Ability in the Intermediate SMA Mouse Model

We next analyzed the impact of PLS3 overexpression in the intermediate SMN-ASO-injected SMA mouse model by testing the motoric performance using the tube test and righting reflex test in neonates and the grip strength test for mice after they were separated from their parents. Tube test and righting reflex test were performed for both background strains (C57BL/6N and FVB/N) and described in the following section. Performance and score point criteria for both tests are listed in section 4.1.7. In C57BL/6N mice, there was no significant difference in tube test performance between SMA, SMA-*PLS3*het, SMA-*PLS3*hom, and HET mice at very early postnatal time-points. In contrast, at P13 a significant difference between SMA and HET mice was observed and was partially rescued by heterozygous and homozygous PLS3 overexpression (Figure 24). Similar as observed in the weight progression of FVB/N mice (5.5) their ability to perform the tube test showed no significant differences between SMA and SMA-PLS3het and is comparable to the ones of HET and HET-PLS3het (Figure 25). The SMN-ASO injected FVB/N SMA mice are by far too healthy to be described as a real intermediate SMA mouse model. All further histological analyses, cell cultures and immunostainings exclusively were only done with mice on C57BL/6N background in order to work with an appropriate intermediate SMA phenotype.
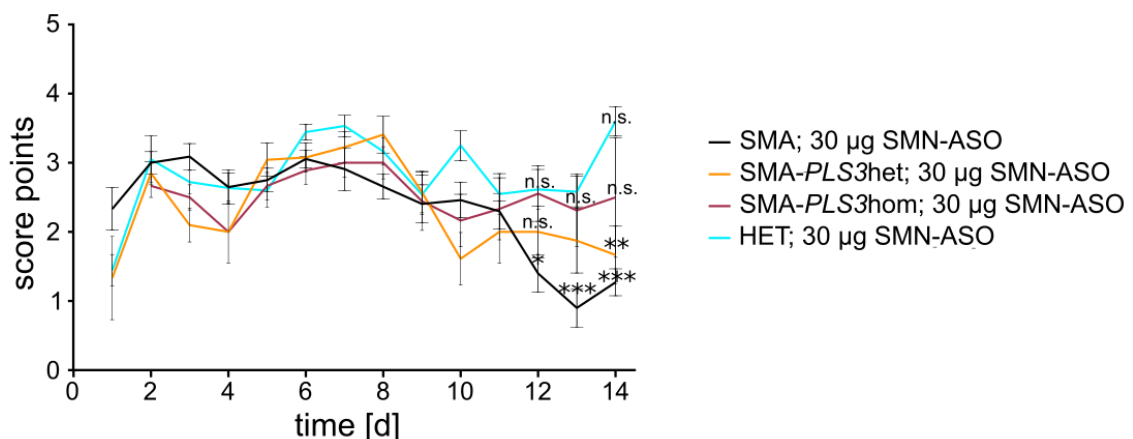
Figure 24: Tube test of neonatal SMN-ASO-injected mice (C57BL/6N) (P1 – P14). SMA-*PLS3*het and SMA-*PLS3*hom mice, but not SMA mice, show an improvement in performance (P12 – P14) (n ≥ 10). (Modified from (Hosseinibarkooie et al. 2016).)
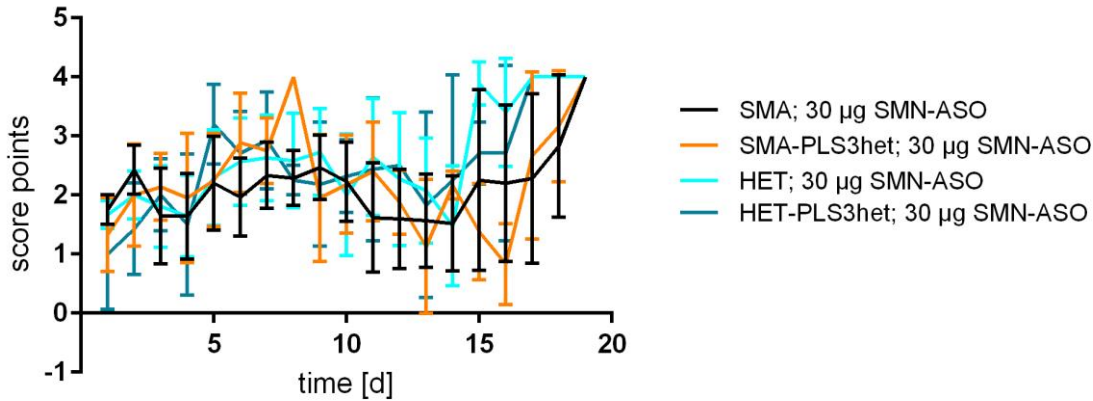
Figure 25: Tube test of neonatal SMN-ASO-injected mice (FVB/N). There is no significant difference in tube test performance between SMA and SMA-*PLS3*het (n ≥ 10).

In a last set of tests for neonatal motoric function the righting reflex test was performed on animals of both backgrounds (C57BL/6N and FVB/N). As in the tube test the error bars indicate the larger variability amongst animals within a group. Different to the tube test, on C57BL/6N background there were no significant differences between SMA + ASO, SMA-PLS3het + ASO and SMA-PLS3hom + ASO detectable at any measured time point (Figure 26). This is also true for the animals on FVB/N background that performed that test (Figure 27).
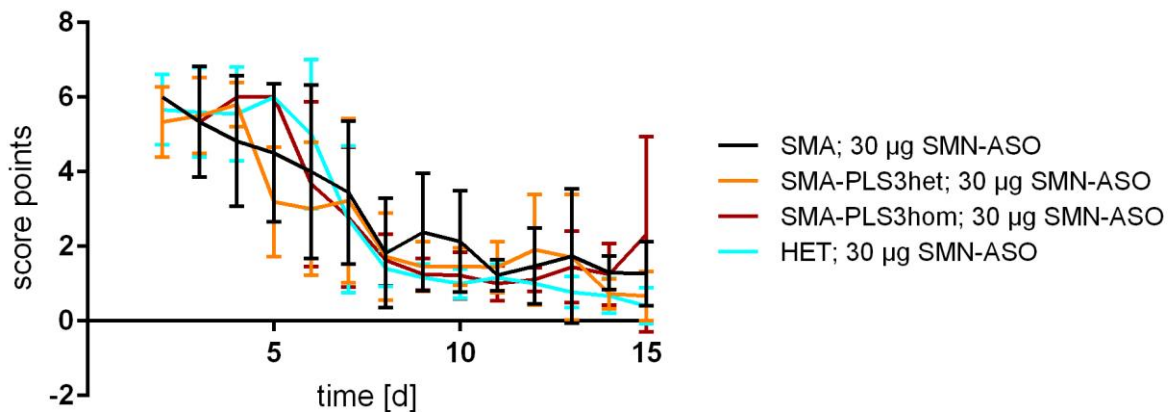
Figure 26: Righting reflex test of neonatal SMN-ASO-injected mice (C57BL/6N). There is no significant difference in tube test performance between SMA and SMA-*PLS3*het (n ≥ 10).
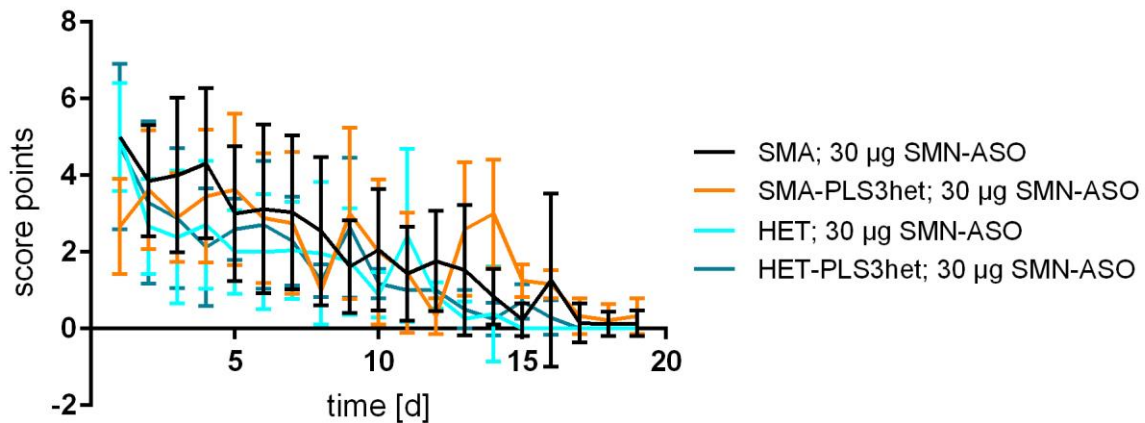
Figure 27: Righting reflex test of neonatal SMN-ASO-injected mice (FVB/N). There is no significant difference in tube test performance between SMA and SMA-*PLS3*het (n ≥ 10).

In addition, the grip strength at P36 and P108 was measured and observed that although SMN-ASO-injected SMA-*PLS3*het and SMA-*PLS3*hom mice at P36 performed the test with diminished grip strength in comparison to the corresponding control group (HET, HET-*PLS3*het and HET-*PLS3*hom), this parameter significantly improved in SMA-PLS3hom mice at P108 (Figure 28). SMA-*PLS3*het or SMA-*PLS3*hom mice that survived >250 days did not show any abnormal motoric movement or paralysis. Performance criteria for this test are mentioned in section 4.1.8.
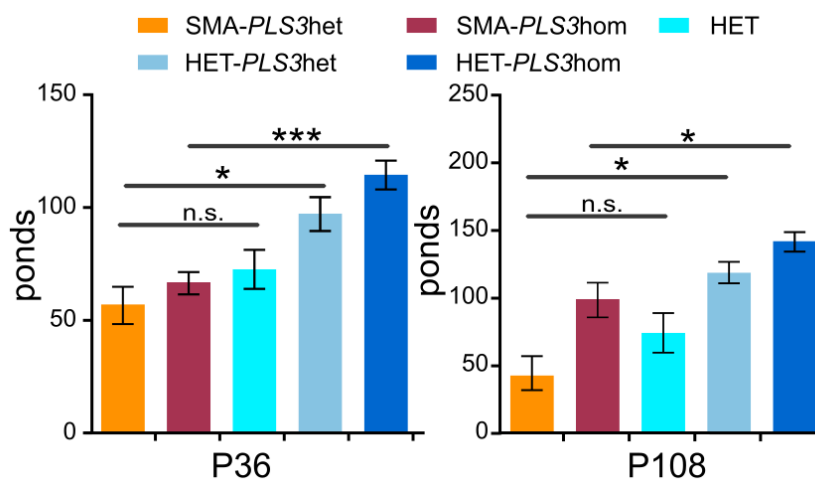
Figure 28: Grip strength test of SMN-ASO-injected mice at P36 and P108. At P108 grip strength force was fully restored in SMA-*PLS3*hom mice, reaching levels comparable to HET and HET-*PLS3*het mice (n ≥ 8). (Modified from (Hosseinibarkooie et al. 2016) by increasing the total number of analyzed animals).

5.7 TISSUE SPECIFIC SMN EXPRESSION AFTER SMN-ASO INJECTION

Interestingly, SMN-ASO injection produced very little increase in SMN amount in the brain (Figure 29A), spinal cord (Figure 29B) or lung (Figure 29C), whereas the liver (Figure 29D) of the same animals clearly showed increased SMN expression. This result suggests that SMN-ASOs have a low blood-brain penetration and that the phenotypic improvements have to be mainly due to an inner organ rescue, which will be shown later (5.9).
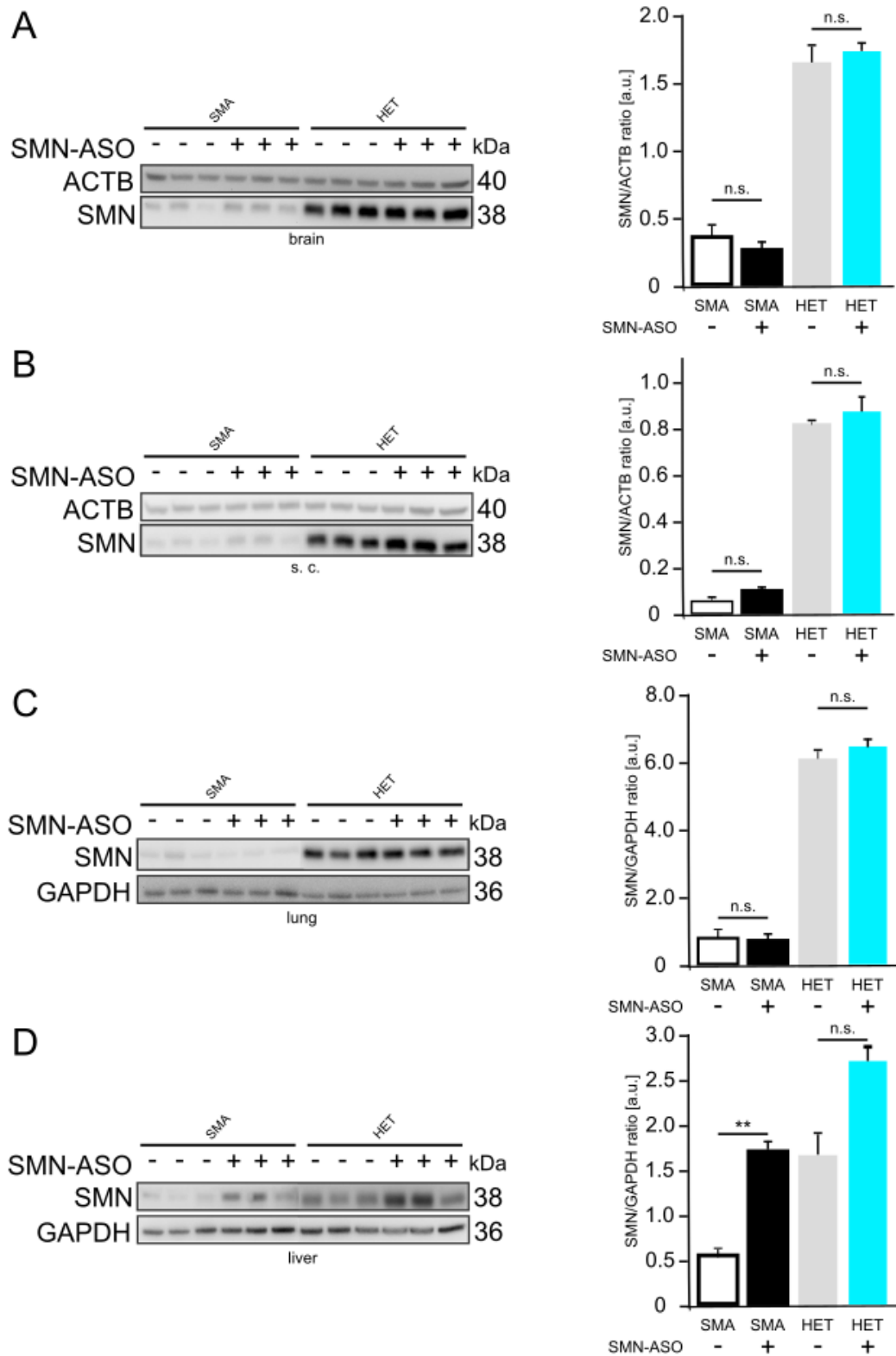
Figure 29: Immunoblot analysis of brain, spinal cord, lung and liver lysates from uninjected and SMN-ASO-treated SMA and HET mice. Notably is that the SMN-ASO only very slightly increased the SMN amount in brain, spinal cord and lung (N = 3). n. s., non-significant, ** $p < 0.01$, 2-tailed Student's t test. Error bars represent SEM.
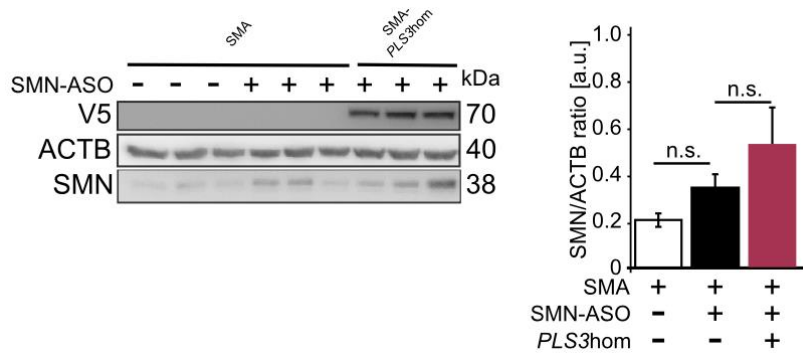
Figure 30: Immunoblot of spinal-cord lysates shows that PLS3 overexpression does not induce significant SMN elevation (N = 3) but a mild augmentation. n. s., non-significant by a two-tailed Student's t test. Error bars represent SEM. (Taken from (Hosseinibarkooie et al. 2016))
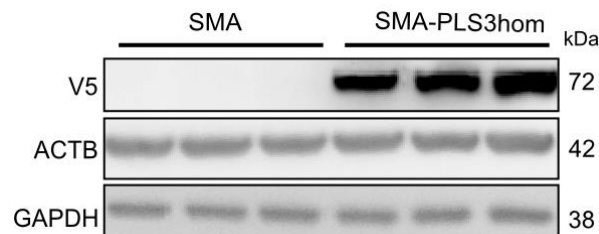
Figure 31: ACTB and GAPDH protein expression upon PLS3 overexpression (V5 staining) does not alter. ACTB and GAPDH were used as housekeeping proteins and loading controls in this study.

5.8   *SMN2* RNA EXPRESSION LEVELS OF SMN-ASO TREATED MICE

To address the question how the SMN-ASO effects the expression level of *SMN2 in vivo*, the total amount of both *SMN2* transcripts, FL-*SMN2* and Δ7-*SMN2*, was quantified. *Gapdh* was used as a internal control. To do so, the RNAs extracted from spinal cord and liver of the untreated SMA and HET as well as the SMN-ASO treated SMA and HET mice were quantified using the RiboGreen® dye (4.3.2.3). Afterwards 150 ng RNA was subjected to reverse transcription. The interpretation of the real-time RT-PCR revealed a substantial effect of the SMN-ASO regiment on the *SMN2* transgene expression. The used primer for the real-time PCR were previously designed in our laboratory to detect only the FL- or the Δ7-*SMN2* transcript, which was derived from the human *SMN2* transgene. The quantitative real-time PCR was performed as described in section 4.3.3.3. The results show a highly significant increase of FL-*SMN2* in spinal cord from P10 SMN-ASO injected mice (Figure

32). This is not only true for SMA mice (SMA; uninjected and SMA; 30 µg SMN-ASO) but also for the corresponding control groups (HET; uninjected and HET; 30 µg SMN-ASO). In contrary to these findings, there were no significant differences of FL-*SMN2* transcript levels after SMN-ASO injection in liver; neither in SMA mice nor in the control group (Figure 32). On the other hand a tendency but not yet significant decrease of Δ7-*SMN2* transcript was observed in this highly metabolic organ after SMN-ASO injection in both the SMA and the HET mice, which supports the results of the protein expression in this organ (Figure 29D). This effect was not observed in spinal cord. At first sight these data seem very contradictory to the protein expression analyses of spinal cord and liver (chapter 5.7). Due to the fact that all performed transcript measurements only refer to the human *SMN2* transgene, small changes in transcript expression were detected that could have only been influenced by the SMN-ASO injection as this ASO is especially designed to correct the splicing defect of *SMN2*, whereas in protein expression studies in HET mice the antibody also detects SMN protein derived from the endogenous mouse *Smn* gene. Therefore, on protein level these small changes may be within the error range and thus not detectable. In addition, we need to take in consideration that there could be cell type specific regulations that influence the SMN-ASO stability. Posttranscriptional regulations and posttranslational modifications can alter the mRNA and protein stability, respectively.
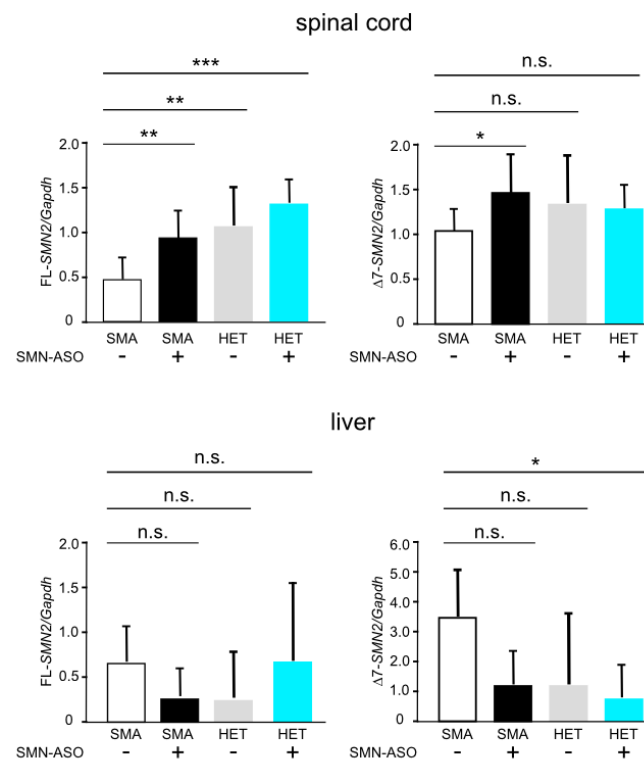
Figure 32: FL- and Δ7 *SMN2* levels in s. c. and liver in P10 SMA and HET (ctrl) mice with and without SMN-ASO injection (N=3 per genotype; n=2 quantitative real-time PCR measurements per animal). n. s. non-significant; * $p < 0.05$; ** $p < 0.01$; *** $p < 0.001$, 2-tailed Student's t test. Error bars represent SD.

5.9   HISTOLOGY OF INTESTINE, LUNG AND HEART IN THE INTERMEDIATE SMA MOUSE MODEL

PLS3 overexpression did not have a strong influence on the survival of the severely affected SMA mice (Ackermann et al. 2013), which we hypothesize could be due to multi-organ dysfunctions in this animal model (Ackermann et al. 2013; Schreml et al. 2013). We next did histological analyses of intestine, lung and heart, to better understand how the SMN-ASO injection affects the inner organ development of these mice. Subsequently, intestine, lung and heart tissues of SMN-ASO-injected P10 mice were collected and a Haematoxylin/Eosin staining of paraffin-embedded slices of these organs was performed. In addition, the weight of hearts of uninjected mice and ones treated with SMN-ASO were compared to each other. SMA-*PLS3*het and SMA-*PLS3*hom mice showed a tendency toward increased heart size in comparison to SMA mice (normalized to body weight) (Figure 33 and Figure 34). SMN-ASO injection ameliorated the multi-organ dysfunction of the lung, heart, and intestine in all SMA mice compared to ctrl-ASO injected mice (Figure 34). Especially the stably structured intestinal epithelium with more intact villi and the reorganizing secretory cells within it as well as the diminished emphysema with ruptured alveolar septa and enlarged alveolar spaces in the lung are noteworthy. Furthermore, these data show that a combinatorial therapy involving SMN-ASO and PLS3 overexpression has a highly beneficial ability to counteract SMA, as already demonstrated by natural protection in human asymptomatic *SMN1*-deleted siblings.
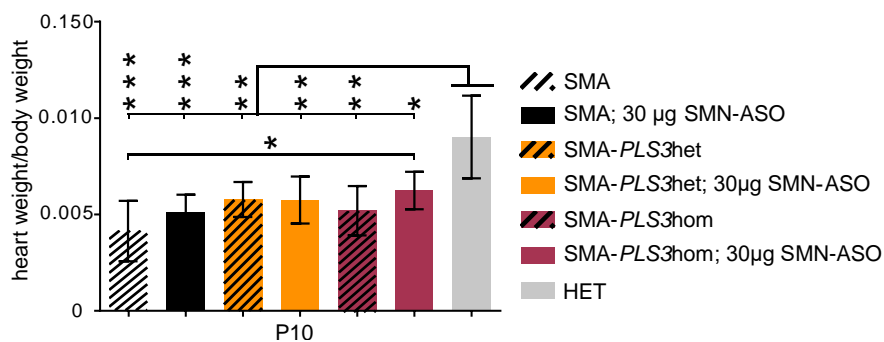
Figure 33: An accumulative effect on the heart size was observed in SMN-ASO-injected SMA mice. The size further increased when PLS3 was overexpressed (N ≥ 3 per genotype). * $p < 0.05$; two-tailed Student's t test. Error bars represent SEM. (Taken from (Hosseinibarkooie et al. 2016).)
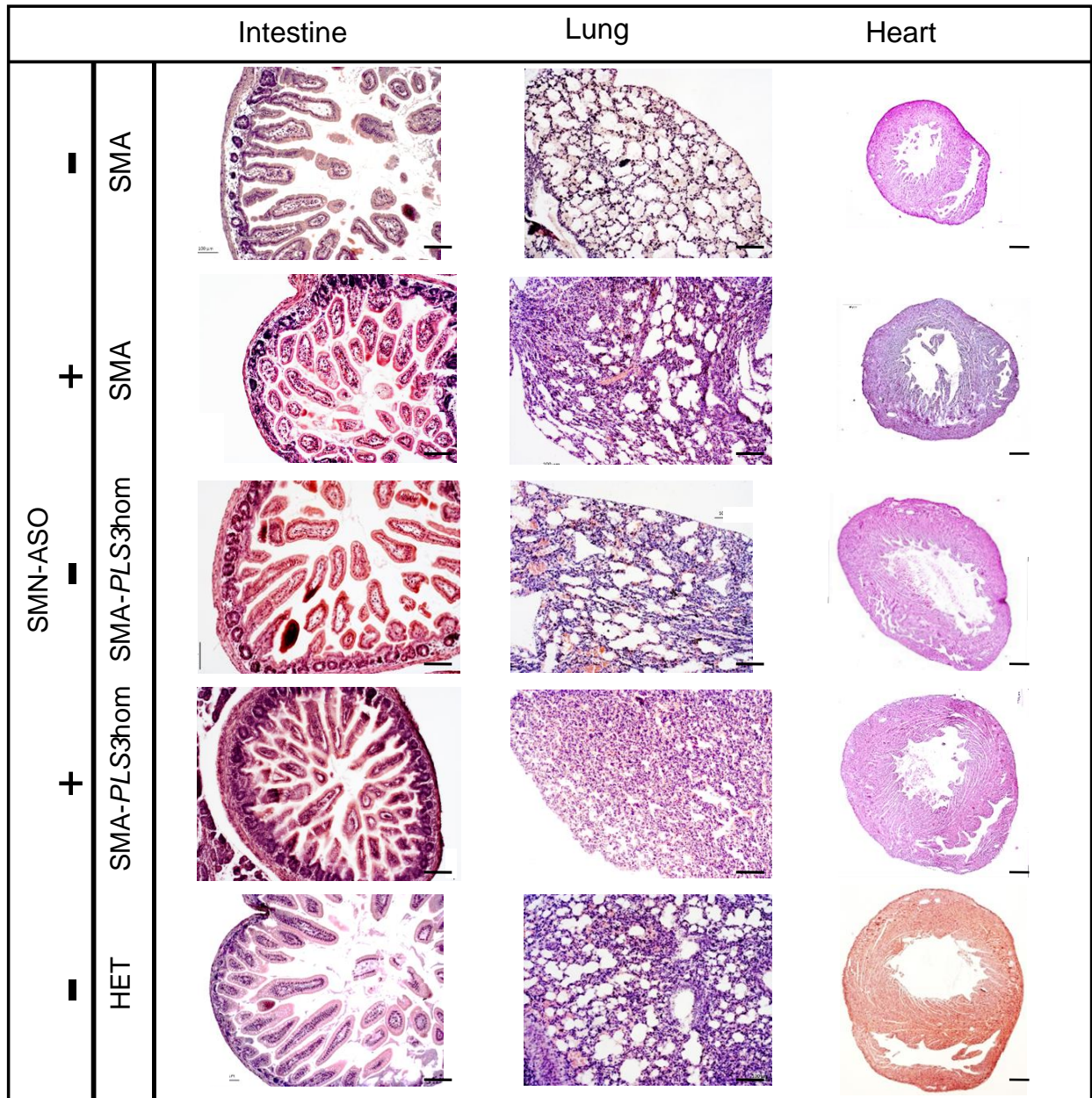
Figure 34: Representative pictures of histological sections from intestine, lung, and heart (P10): Injection of SMN-ASO and PLS3 overexpression improved intestine, lung, and heart phenotypes in SMA mice. An increased number of intact intestinal villi as well as a better organization of the secretory cells, less emphysema with ruptured alveolar septa, enlarged alveolar spaces in the lung, and an increased heart size can be observed. The scale bar represents 100 μm. (Taken from (Hosseinibarkooie et al. 2016).)

5.10 PLS3 OVEREXPRESSION INCREASED NMJ SIZE

To clarify whether the SMN-ASO injection combined with *PLS3*hom overexpression has a direct influence on the postsynaptic site, TVA muscle tissue was collected from all genotypes that are represented in Figure 35 and NMJ size was measured after bungarotoxin staining. Analysis of the NMJ structures revealed that injection of SMN-ASO significantly increased the NMJ size in both SMA and HET mice (Figure 35). An accumulative effect of SMN-ASO and PLS3 overexpression on NMJ size was observed at P10, and this effect was consistent with our previous findings regarding the role of PLS3 in NMJ structure and function (Ackermann et al. 2013).
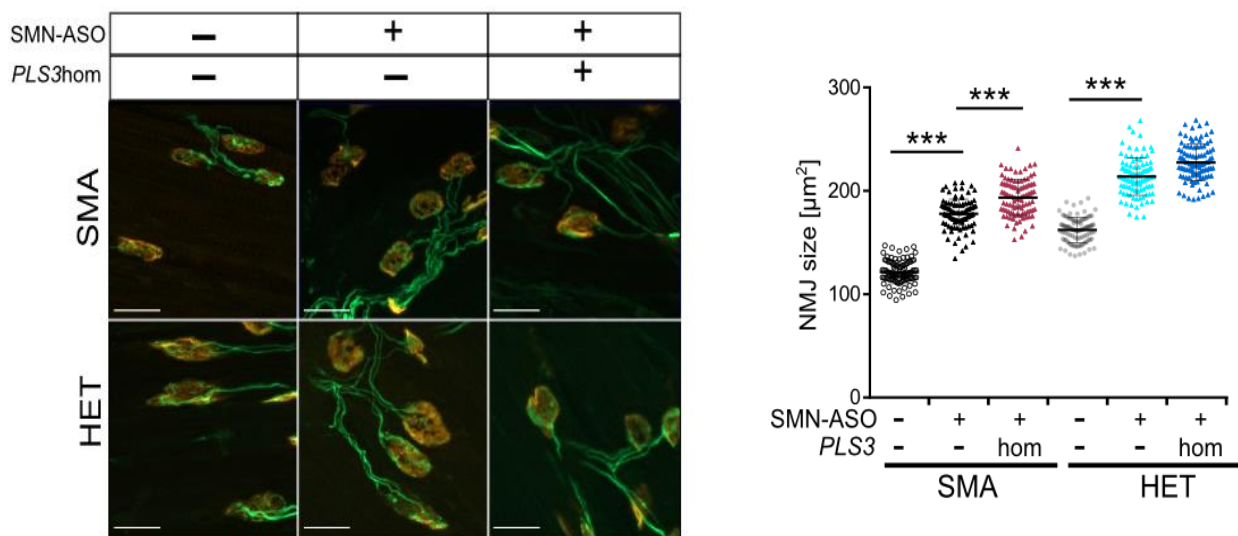
Figure 35: Representative pictures of NMJ (P10) stained with SV2 and NF (green) for the neuronal part and bungarotoxin (red) for the postsynaptic part and quantification shows that injection of SMN-ASO significantly increased the NMJ size in comparison to that of NMJs of untreated SMA mice at P10. Upon PLS3 overexpression, an accumulated effect of SMN-ASO and PLS3 overexpression was observed at the NMJ level (n = 5 per genotype, 100 NMJs measured per animal). The scale bar represents 20 µm. (Taken from (Hosseinibarkooie et al. 2016).

5.11 PLS3 OVEREXPRESSION INCREASED THE NUMBER OF PROPRIOCEPTIVE INPUTS

SMA mice emerge with poorly developed connectivity between primary proprioceptive afferents and MN cell bodies (Mentis et al. 2011). To investigate the influence of PLS3 in this context, the lumbar L4–L5 spinal region of SMN-ASO-injected mice was immunostained with vesicular glutamate transporter 1 (VGlut1), a well-described marker for proprioceptive primary afferents, and choline acetyltransferase (ChAT), a MN marker. Furthermore, quantification of the VGLUT1 puncta on the MN soma revealed an increased number of proprioceptive inputs and MN soma volume upon SMN-ASO injection. Overexpression of PLS3 together with SMN-ASO has an additive effect and is able to restore the reduced number of proprioceptive inputs on MN soma (Figure 36).
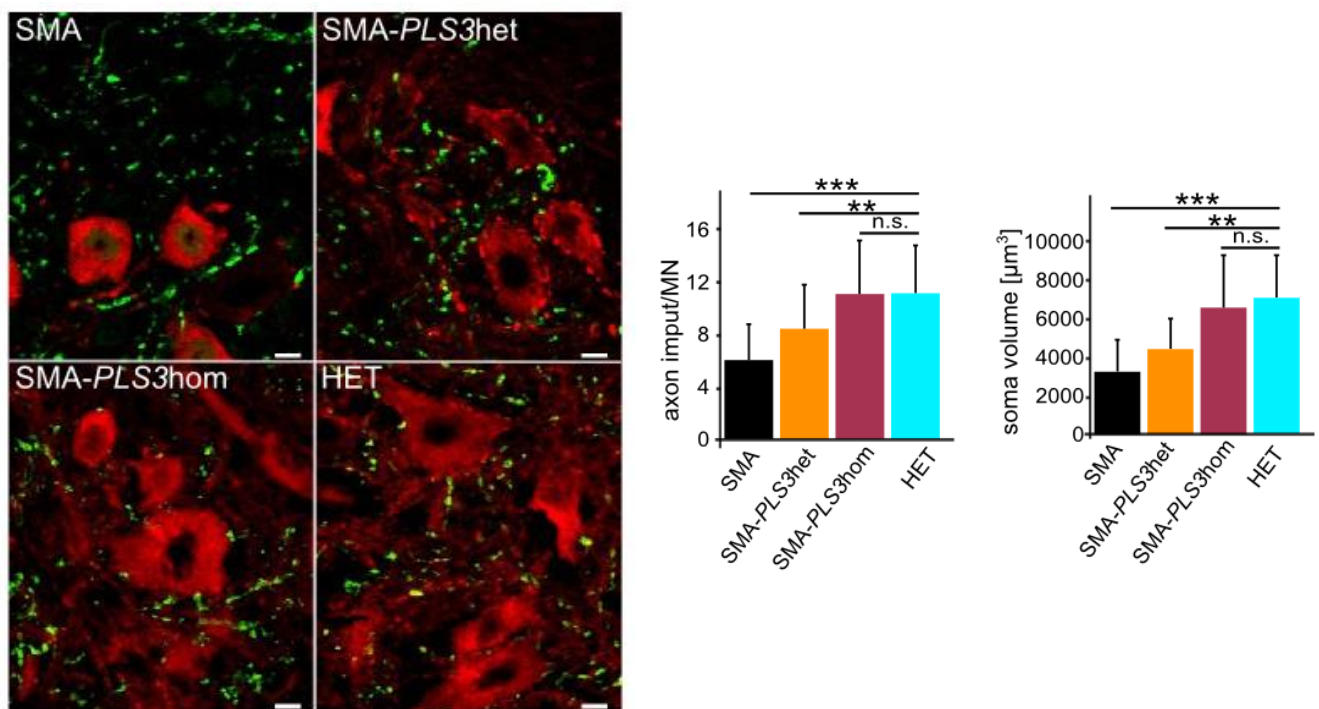
Figure 36: Representative pictures of MN soma (ChAT, red) and proprioceptive input (VGLUT1, green) derived from SMN-ASO-injected mice (P21). Quantification shows that SMN-ASO injection and PLS3 overexpression significantly improved the number of proprioceptive inputs on the MN soma (n ≥ 70). n. s., non-significant; * p < 0.05; ** p < 0.01; *** p < 0.001, two-tailed Student's t test. Error bars represent SEM. The scale bar represents 10 µm. (Taken from (Hosseinibarkooie et al. 2016).)

5.12 AXON LENGTH IS RESCUED BY PLS3 OVEREXPRESSION

Previous work in SMN-deficient MN cultures from SMA mice or MN–like cells showed severe reduction in axonal length. Moreover, the main phenotype in *smn*-deficient zebrafish, is an aberrant growth of motor axons (Oprea et al. 2008). Therefore, we investigate the influence of PLS3 on the axon length of cultured primary murine MNs. The MN cultures were generated as described in section 4.2.2 and immunostained with α-ChAT and α-NF (3.8.1) to measure axon outgrowth of MNs (4.2.6). Figure 37 show representative pictures of MNs derived from SMA, SMA-PLS3het, SMA-PLS3hom, HET, HET-PLS3het, and HET-PLS3hom mouse embryos. The quantification shown in Figure 38 demonstrates the rescuing effect of PLS3 on the axon length of MNs in the Taiwanese SMA mouse model.
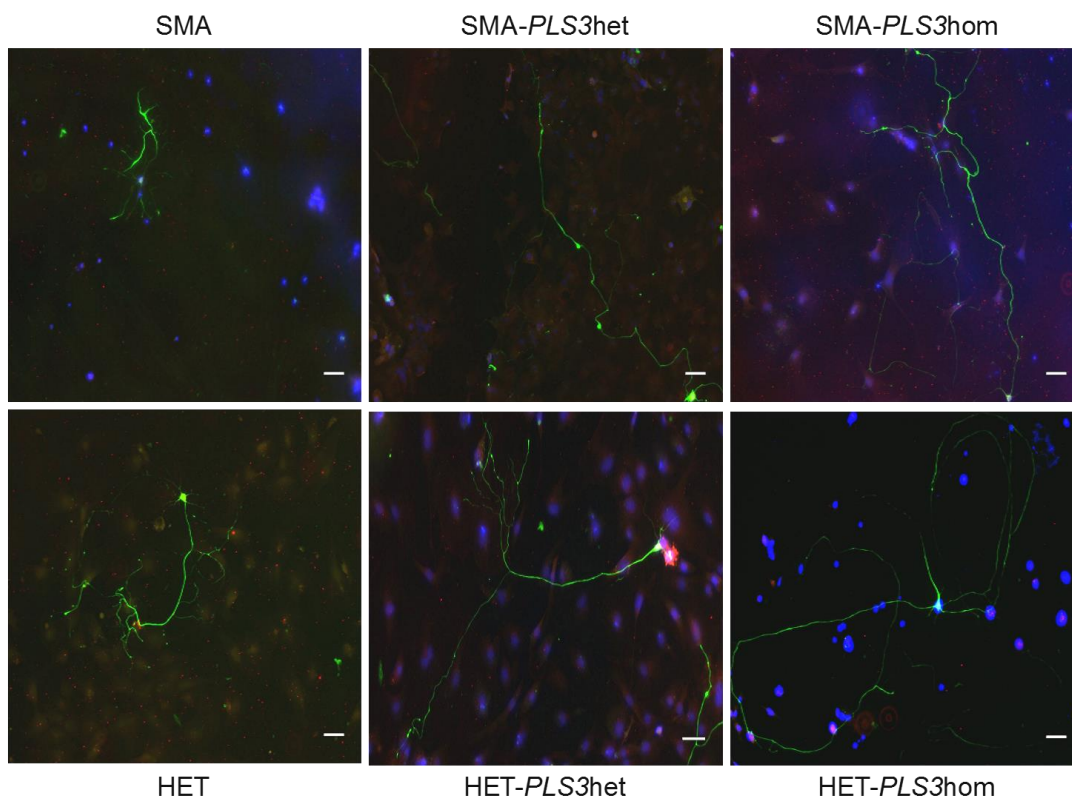
Figure 37: Representative pictures of MNs: nucleus (Hoechst, blue), MNs (ChAT, red) and axons (NF, green) derived from SMA, SMA-*PLS3*het, SMA-*PLS3*hom, HET, HET-*PLS3*het, and HET-*PLS3*hom mouse embryos (E13.5). The scale bar represents 50 µm.
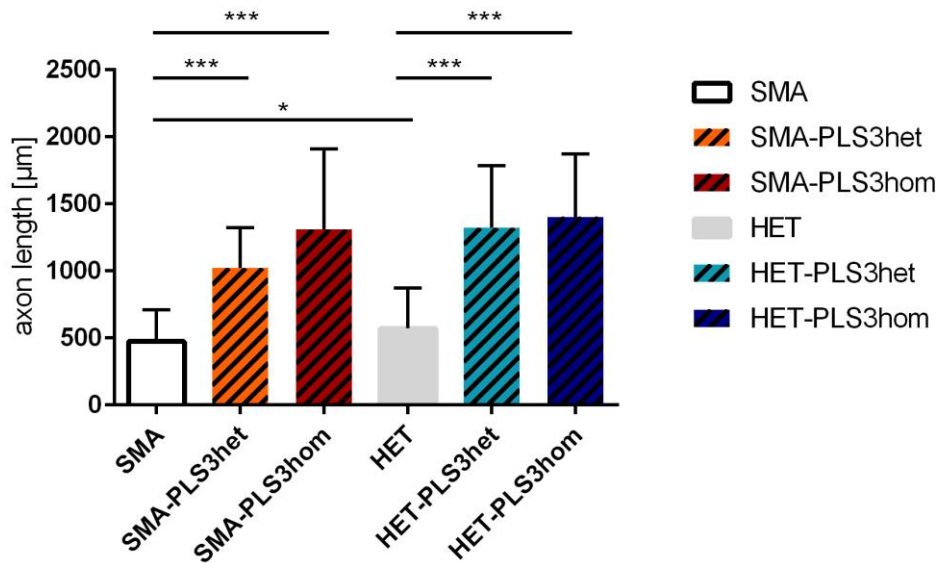
Figure 38: PLS3 overexpression rescues axon length in MNs: Quantification of axon length in MNs: N = 3 per genotype, 100 cells measured per cell line. The axon length in SMA-*PLS3*het and SMA-*PLS3*hom versus SMA MNs was significantly different. * p < 0.05; *** p < 0.001, 2-tailed Student's t test. Error bars represent SD.

5.13 SMA IMPAIRS ENDOCYTOSIS, WHICH IS RESCUED BY PLS3 OVEREXPRESSION

PLS3 is an F-actin-binding and -bundling protein that is involved in many cellular processes (Delanote et al. 2005; Pollard and Borisy 2003). Knockdown of Sac6p, the ortholog of PLS3 in yeast, leads to disturbed endocytosis (Kubler and Riezman 1993). Moreover, F-actin, which is important for all types of endocytosis (Engqvist-Goldstein and Drubin 2003; Doherty and McMahon 2009), has been shown to be disturbed in SMA (Ackermann et al. 2013; Francesca et al. 2016; Bowerman et al. 2007). Therefore, in our laboratory we hypothesized that reduced SMN amount might impair endocytosis and can be rescued by PLS3 overexpression.

5.13.1 FITC-Dextran uptake in murine embryonic fibroblasts

To verify this theory, first the uptake of fluorescently labeled dextran (FITC-Dex) by fluid-phase endocytosis (Doherty and McMahon 2009) was measured in murine embryonic fibroblast cell lines (MEFs) derived from SMA, SMA-*PLS3*het, HET, and HET-*PLS3*het mice. Fluorescence microscopy imaging was used to quantify FITC-Dex uptake in cells fixed at

different time points. A strong reduction in endocytic uptake of FITC-Dex was observed in SMA compared to HET MEFs (Figure 39), but uptake was significantly restored by PLS3 overexpression (Figure 40).
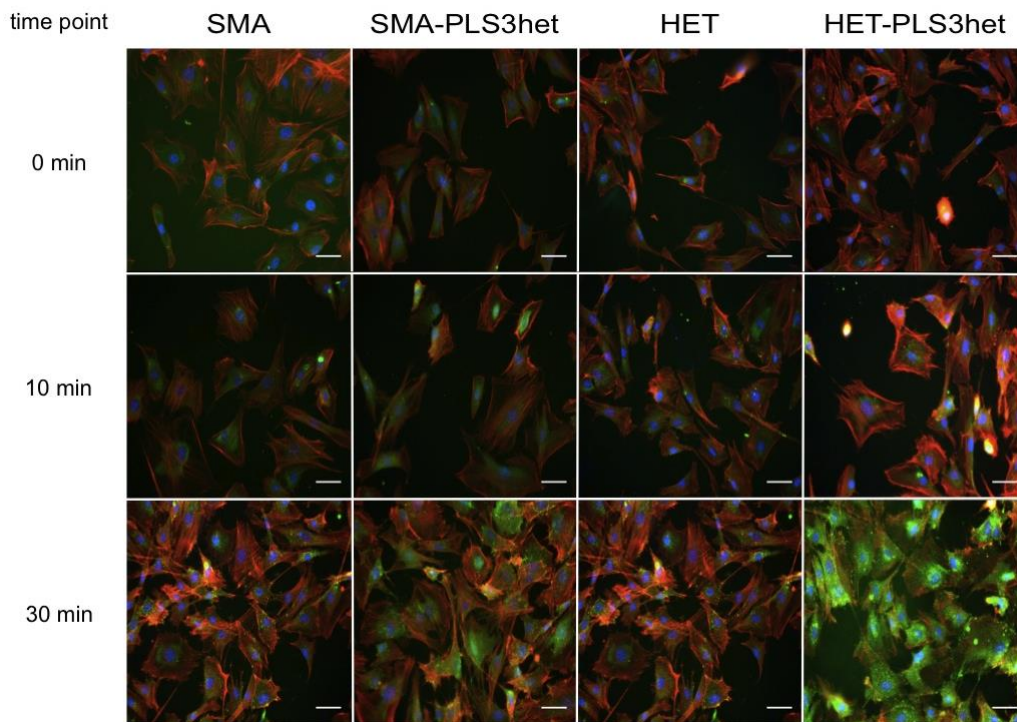
Figure 39: Representative pictures of MEFs: nucleus (Hoechst, blue), actin filaments (Phalloidin, red) and FITC-Dextran uptake (green) derived from SMA, SMA-*PLS3*het, HET, and HET-*PLS3*het mouse embryos (E13.5). The scale bar represents 50 µm.
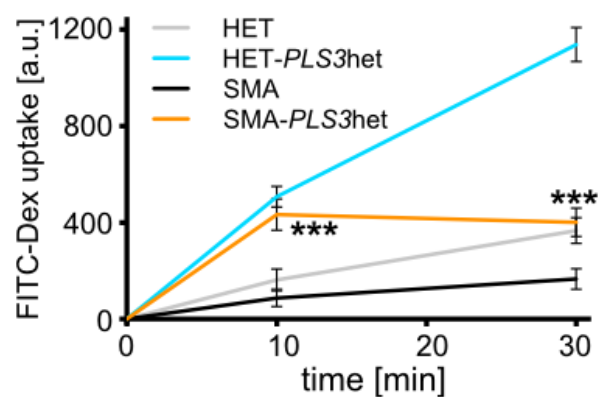
Figure 40: PLS3 Overexpression Rescues Impaired Endocytosis in MEFs: Quantification of FITC-Dex uptake in MEFs was performed via fluorescence-intensity analysis (N = 3 per genotype and time point, 100 cells measured per cell line). The amount of uptake in SMA versus SMA-*PLS3*het mice was significantly different at 10 and 30 min. (Taken from (Hosseinibarkooie et al. 2016).)

5.13.2 FM1-43 Endocytosis Experiment

Additionally, we performed an electrophysiological experiment, using ex vivo preparations of TVA muscle dissected from P10 mice. Muscles were kept in physiological solutions to maintain alive. All electrophysiological experiment were performed by Dr. Laura Torres-Benito, who is an expert on the field. Electrical stimulation of the N. intercostalis innervating the TVA muscle (see sketch Figure 41A) was performed in two independent sets: a low-frequency set at 5 Hz and a high-frequency set at 20 Hz for analysis of FM1-43 uptake. As previously shown in a study performed in hippocampal neurons, low-frequency stimulation mainly triggers clathrin-mediated endocytosis (CME), whereas high-frequency stimulation activates clathrin-independent endocytosis (CIE) or activity-dependent bulk endocytosis (ADBE) (Kononenko et al. 2014). Postsynaptic sites were stained with bungarotoxin conjugated with Alexa647 (BTX-Alexa647). Through delimitation of these areas, the mean intensity of the FM1-43 at the presynaptic terminals could be quantified Figure 41B. At low-frequency stimulation, FM1-43 intensity was significantly reduced in SMA compared to HET mice (Figure 41B and Figure 41C), whereas in SMA-*PLS3*het and SMA-*PLS3*hom NMJs, endocytosis was restored to HET levels upon 5 Hz stimulation (Figure 41C).
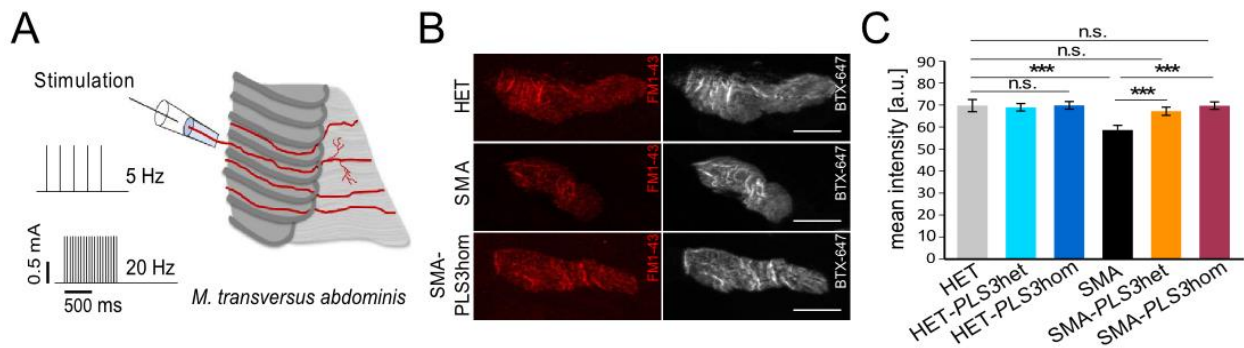
Figure 41: PLS3 overexpression rescues impaired endocytosis at presynaptic sites of NMJs in SMA mice. (**A**) Experimental setup for stimulation of the N. intercostalis innervating the TVA muscle. (**B**) Representative pictures of NMJs from HET, SMA, and SMA-*PLS3*hom muscles. Staining of postsynaptic receptors (BTX-Alexa647, gray) helped to define the area in which FM1-43 uptake (red) at the presynaptic terminals was analyzed (n = 3 per genotype, ~100 NMJs measured per genotype). The scale bar represents 10 mm. (**C**) Quantification of the FM1-43 mean intensity at the presynaptic terminals at P10 in TVA muscles without ASO injection under low frequency stimulation (5 Hz, 1 s). n.s., non-significant; ***p < 0.001, two-tailed Student's t test. Error bars represent SEM. (Modified from (Hosseinibarkooie et al. 2016).)

Presynaptic uptake of FM1-43 dye without electrical stimulation was excluded Figure 42A. NMJs of TVA from SMA mice are reported to be smaller (Torres-Benito et al. 2011; Murray et al. 2008). FM1-43-intensity was correlated to NMJ size to confirm that these two

parameters do not correlate Figure 42C. At a high-frequency stimulation of 20 Hz, endocytosis was also decreased in SMA compared to HET mice. PLS3 overexpression in both, SMA-*PLS3*het and SMA-*PLS3*hom NMJ, rescued the impaired phenotype Figure 42B. These experiments underline how PLS3 counteracts the disturbances within the endocytosis pathway that occur in SMA pathology at the NMJ.
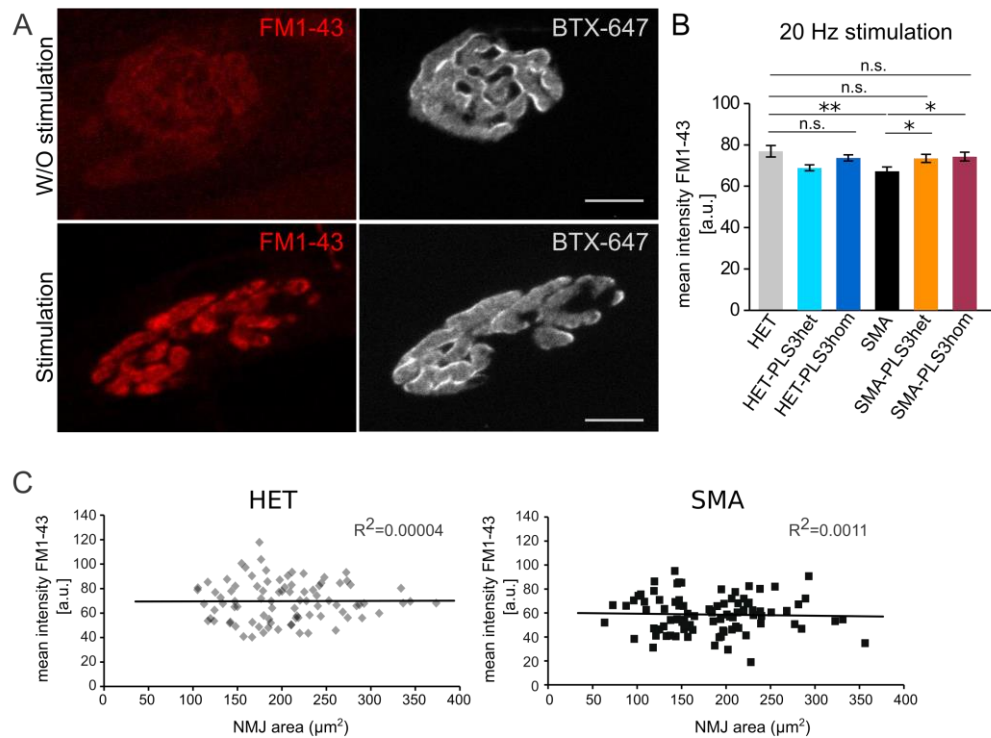
Figure 42: FM1-43 uptake at the presynaptic site in TVA muscle is stimulation-dependent. A) WT TVA muscles at P21 treated with FM1-43 dye with and without stimulation. Muscles without stimulation do not show any FM1-43 staining, proving that uptake of FM1-43 dye is stimulation-dependent. Postsynaptic receptors staining (BTX-647, grey) was used to define the area to analyze the FM1-43 uptake (red) at the presynaptic terminals. Scale bar: 10 µm. B) Quantification of the FM1-43 mean intensity at the presynaptic terminals in P10 TVA muscles without ASO injection under high frequency stimulation (20 Hz, 1s). C) NMJ size does not influence the uptake of FM1-43. Plotting the amount of FM1-43 uptake against the NMJ size did not show any correlation between the uptake amount and the endplate size in both HET and SMA TVA muscles (n = 3 per genotype, ~100 NMJs measured per genotype). n.s. non-significant; ** p < 0.01; *** p < 0.001, 2-tailed Student's *t* test. Error bars represent SEM. (Modi from (Hosseinibarkooie et al. 2016).)

6. Discussion

6.1   PLS3 MEDIATES A PHENOTYPIC RESCUE IN AN INTERMEDIATE SMA MOUSE MODEL

The actin filament binding and bundling protein PLS3 was reported as the first SMA modifier besides *SMN2* that was highly upregulated in *SMN1*-deleted individuals of six discordant families of SMA (Oprea et al. 2008). Indeed, when iPSCs were derived from fibroblasts from SMA patients and asymptomatic *SMN1*-deleted siblings and subsequently differentiated into MNs, PLS3 upregulation was observed only in these unaffected individuals, importantly in the disease-relevant cell type (especially in the growth cones) (Heesen et al. 2016). However, previous studies performed in two severely affected mouse models: Taiwanese and Δ7 SMA did not reveal the whole spectrum of the PLS3 protective effects (McGovern et al. 2015; Ackermann et al. 2013). PLS3 did not increase survival, despite ameliorating NMJ formation and maintenance as well as motoric abilities in Taiwanese SMA neonatal mice (Ackermann et al. 2013). These results, as well as the fact that every asymptomatic *SMN1*-deleted individual has at least 3 – 4 *SMN2* copies, led to the assumption that it is necessary to increase SMN levels above a certain threshold for PLS3 to fully unfold its modifying ability (Hosseinibarkooie et al. 2016). Comparing previous findings that are described above with the present study, we can conclude that our threshold hypothesis was correct as we observed only in the intermediate SMA mice that PLS3 provides an extensive phenotypic rescue, involving survival (5.4), weight progression (5.5), motoric ability (5.6), inner organ defects (5.9), NMJ integrity (5.10) and proprioception (5.11) as well as improved endocytic uptake (5.13). Therefore, using SMN-ASO injection to induce an intermediate phenotype in the severely affected Taiwanese SMA mice did not only provided us with a model that resembles more the condition of asymptomatic *SMN1*-deleted individuals but also supported the idea that combinatorial therapy of suboptimal doses of SMN-ASO in addition to compounds that either directly elevate PLS3 levels or compensate for the defects in the endocytosis pathway might be a feasible strategy for future clinical trials.

6.2   WHY ARE INTERMEDIATELY-AFFECTED SMA MOUSE MODELS NECESSARY BUT CHALLENGING TO PRODUCE?

In severe SMA mouse models with extremely low SMN levels, defects in a plethora of pathways apart from the neuromuscular system have been reported, especially affecting non-neuronal cell types and organs and leading to severe multi-organ failure (Hamilton and Gillingwater 2013; Sleigh et al. 2011). However, the protective modifying genes have been identified in asymptomatic individuals who would hypothetically present a milder form of SMA. Therefore, it is more suitable to use SMA models of an intermediate phenotype when searching for defects of cellular mechanisms in SMA pathology that are restored by protective modifying genes. As two human *SMN2* copies on a murine *Smn*-null background produce a severe phenotype and result in early death, while mice with three *SMN2* copies are already asymptomatic, it is rather challenging to produce a genetically engineered intermediate or mild SMA mouse model (Monani et al. 2000b; Hsieh-Li et al. 2000; Riessland et al. 2010). Indeed, a systemic approach aiming at generating intermediate SMA type 2 or 3-like mouse by the use of complete allelic series resulted in only these two phenotypic extremes: either severe or asymptomatic (Osborne et al. 2012).

Nonetheless, several groups successfully generated mice with intermediate phenotype as described in section 1.1.6.4 and 1.1.6.5. The Smn$^{2B/KO}$ mouse model has the advantage to analyze influences of protective modifying genes in an *SMN2*-independent context (Bowerman et al. 2012a), whereas the Burgheron mouse offers the great possibility to use a combined treatment strategy of protective modifiers in addition to SMN-ASO or morpholino injection, as well as to explore the window for therapeutic intervention (Bogdanik et al. 2015).

Intermediate SMA mouse models offer an opportunity to answer whether therapeutic approaches are temporarily limited to presymptomatic stages or if they extend even to later time points after the onset of the symptoms (Bogdanik et al. 2015). Treatment with compounds such as SMN-ASOs or morpholinos either solely injected into the severe SMA mouse models or as combined therapy similar to the present study, provide powerful tools to translate new findings to the human SMA pathology more efficiently and unravel pathway defects within target tissues. Hence, patients benefit from new therapies with more specific target strategies.

6.3   COMBINED EFFECT OF SMN-ASO AND PLS3 OVEREXPRESSION ON THE NEURONAL CIRCUITRY OF SMA ANIMALS

Pre-symptomatic treatment with higher doses of SMN-ASO fully rescues the SMA phenotype in mice, with the exception that these animals manifest a smaller body size (Hua et al. 2010; Porensky et al. 2012). Therefore, in this study we applied low doses of SMN-ASO, as we did not aim for a complete rescue, but rather an intermediate SMA model, which would serve as a platform to investigate the effect of elevated PLS3. As described in sections 4.1.6 and 5.3, we subcutaneously injected the Taiwanese mice at P2 and P3 with suboptimal doses of SMN-ASO (30 µg per injection) to increase SMN amounts in order to compensate for the described inner organ failure (5.9) and thereby increasing survival from 14 to 28 days. However, despite injecting SMN-ASO during early development and maturation of NMJs, the SMN increase was not sufficient to compensate for all defects within the neuronal circuitry. It increased NMJ size in comparison to NMJs of untreated mice (5.10) but the number of proprioceptive inputs and the MN soma size is still smaller in comparison to controls (5.11). Similarly, in mildly affected SMA patients, the SMN amount seems to be sufficient to maintain its housekeeping function in all cells except MNs (Wirth et al. 2015; Hamilton and Gillingwater 2013). In comparison to previously reported impairment of sensory motor connectivity (Mentis et al. 2011), we observed that elevated SMN amounts in combination with PLS3 overexpression, had a great beneficial impact on the disturbed neuronal circuitry of SMA mice. Among these there are increased NMJ size, which reflects an improved AChR clustering, and elevated proprioceptive inputs at the MN soma, as well as increased MN soma size (see also section 5.10 and 5.11). Interestingly, even in MNs derived from severely affected Taiwanese mice, PLS3 overexpression alone led to increased length of the main axon (see also section 5.12). As mentioned above, SMN-ASO or morpholino injection needs to be done during early developmental stages (neonatal mice) as higher amounts of SMN protein are required before P17 during development and maturation of NMJs (Kariya et al. 2014). If the SMN elevation in either low-dose pre-treated Δ7 SMA mice or in an intermediate mouse model is achieved later, it leads to only very moderate rescuing effects (Feng et al. 2016; Bogdanik et al. 2015; Zhou et al. 2015).

6.4 PLS3 OVEREXPRESSION RESCUES SURVIVAL IN THE INTERMEDIATE, BUT NOT IN THE SEVERE SMA MICE

As previously reported, PLS3 compensated for some symptoms of SMN deficiency in SMA-*PLS3*het mice, considering its restoring effect at the NMJ. Among these there is an improved connectivity at the presynaptic site, delayed axonal pruning, increased F-actin levels and AChR clustering at the postsynaptic site (Ackermann et al. 2013). Despite these improvements, elevated PLS3 was still not able to increase survival rate or weight progression, even if expressed homozygously (see also section 5.1). Our findings were reproduced by another group using a different severe SMA mouse model (McGovern et al. 2015). In these Δ7 SMA mice, overexpression of PLS3 did not improve the SMA phenotype. They detected elevated mRNA *PLS3* levels in the MNs and increased PLS3 protein overexpression throughout the whole spinal cord. This augmentation of PLS3 did neither change survival or weight nor improved the measured quantal content at the NMJ. Hence, as stated above, PLS3 cannot compensate for the inner organ dysfunctions in the severely affected Taiwanese or Δ7 SMA mice. As a consequence, these animals die early due to multi-organ failure.

Our SMN-ASO-induced intermediate mouse model survived for approximately one month and PLS3 overexpression prolonged the survival to more than 400 days in 30% and 250 days in 60% of all mice tested. In 25% of all SMN-ASO injected animals, mice died as early as untreated ones, despite PLS3 overexpression. We assumed that the SMN-ASO was not equally distributed and these suboptimal doses were not uniformly dispersed among all affected tissues, which caused the early death. However, in the majority of animals, PLS3 overexpression led to a marked increase in survival, suggesting that PLS3 overexpression is able to counteract the cellular defects caused by SMN deficits (Hosseinibarkooie et al. 2016).

Interestingly, when using the self-complementary adeno-associated virus 9 (scAAV9) for gene delivery into MNs of SMA mice by intravenous (Foust et al. 2010; Valori et al. 2010; Dominguez et al. 2011) or intramuscular injection (Benkhelifa-Ziyyat et al. 2013), the *SMN* gene was delivered to the spinal cord and thereby decreased disease severity in SMA mice. scAAV9-SMN is able to cross the blood brain barrier (BBB) and efficiently transduce MNs in the lumbar region of the spinal cord as well as muscle tissue. In the context of finding stably functioning intermediate or mild SMA animal models to test further modifiers, this technique could be very promising.

As mentioned earlier, SMN upregulation after disease onset did not effectively ameliorate the outcome of the SMA phenotype in mice (Bogdanik et al. 2015; Zhou et al. 2015; Feng et al. 2016). In case of type II and III SMA patients, an SMN-independent therapy targeting impaired endocytic processes and/or increasing the F-actin amounts could be more effective. As the majority (60%) of all SMA patients are SMA type I (Monani and De Vivo 2014) and SMN-ASO therapy is limited by the *SMN2* copy number, SMN elevation may be insufficient to protect MNs, cure SMA life-long, or rescue all additional symptoms, such as cardiac problems, spinal deformities and joint contractures. Therefore, SMA type I patients will benefit the most from combinatorial therapy of SMN-ASO and an *SMN2*-independent modifier and may have a great potential for future therapy strategies as we proved *in vivo*.

6.5   PLS3 AND ITS IMPACT IN NON-NEURONAL TISSUES

In several previous studies, muscle defects and dysfunction of non-neuronal tissues in SMA patients, as well as inner organ defects in mouse models of SMA have been reported and characterized in more detail (Schreml et al. 2013; Riessland et al. 2010; Shababi et al. 2010; Hayhurst et al. 2012; Shababi et al. 2012; Bevan et al. 2010; Heier et al. 2010; Butchbach et al. 2010; Bowerman et al. 2012b; Cifuentes-Diaz et al. 2001; Hua et al. 2011; Vitte et al. 2004; Le et al. 2011; Talbot 1999; De Sanctis et al. 2016; Shababi et al. 2014). In this context, muscular defects that did not secondarily occur due to decreased innervations but primarily due to SMN deficits are outlined in the following. Interestingly, in severely affected SMA mice abnormal differentiation and myotube formation (Hayhurst et al. 2012) have been described. Many different features that contribute to an early death of the Taiwanese SMA mice were previously reported and well characterized. Among these are not only changes in the molecular composition of skeletal muscle (Mutsaers et al. 2011) but also alterations of lung tissue described with dark red spots and ruptured alveolar septa and emphysema (Schreml et al. 2013). Additionally, these SMA mice suffer from diarrhea and the reduced numbers of villi in the small intestine. They show a prolapsed rectum, as well as intramural edema in the lamina propria (Schreml et al. 2013). Most importantly, a cardiac phenotype is well characterized in all commonly used severely affected SMA mouse models (Monani et al. 2000a; Riessland et al. 2010; Bowerman et al. 2012a). Noteworthy are Intraventricular septum remodelling and thin ventricular walls (Hua et al. 2011; Shababi et al. 2010), as well as vascular remodelling with interstitial fibrosis (Shababi et al. 2010), decreased numbers of capillaries and smaller cardio-myocytes (Shababi et al. 2012). Moreover, previous studies

revealed that transgenic mice lacking murine *Smn* in the liver are embryonic lethal (Vitte et al. 2004). They have reduced levels of Insulin-like growth factor binding protein acid labile subunit (IGFALS) in the liver (Hua et al. 2011), concomitant with glucose intolerance, hypersensitivity to insulin, hypoglycemia and hyper-glucagonemia, which have been reported in *Smn*[2B/KO] mice (Bowerman et al. 2012b) and Δ7 SMA mice (Butchbach et al. 2010). In the past, these characterizations of inner organ defects primarily contributed to a better understanding of – primary or secondary – non-neuromuscular organ involvement in SMA pathology and led to improved standards of care and reassessment of how to investigate SMA patients clinically. Interestingly, overexpression of PLS3 in the severely affected Taiwanese SMA mice increased muscle fibre size (Ackermann et al. 2013) but neither diminished intestinal problems (such as diarrhoea) nor increased heart size (see also section 5.9 and (Hosseinibarkooie et al. 2016)). PLS3 overexpression only reduced these inner organ impairments in the SMN-ASO-induced intermediate SMA mouse model, in which sufficient SMN amounts are present. In this case, SMA-*PLS3*het and SMA-*PLS3*hom mice showed a tendency towards increased heart size in comparison to SMA mice. Moreover, SMN-ASO injection ameliorated the inner organ impairments of the lung, heart, and intestine in SMA mice and were further improved in combination with PLS3 overexpression. The stably structured intestinal epithelium with more intact villi and the reorganizing secretory cells within it, as well as the diminished emphysema with ruptured alveolar septa and enlarged alveolar spaces in the lung are noteworthy (5.9). Taken together, these data additionally underline that a combinatorial therapy involving SMN-ASO and PLS3 overexpression has a highly beneficial ability to counteract SMA, as already found by natural protection in asymptomatic *SMN1*-deleted individuals.

6.6 ENDOCYTOSIS AND SYNAPTIC VESICLE RECYCLING ARE IMPAIRED IN SMA AND RESCUED BY PLS3

PLS3, which has been shown to be a F-actin-binding and -bundling protein, impairs endocytosis when knocked out in yeast (Kubler and Riezman 1993). As mentioned above (1.4), numerous studies have already addressed the role of actin as a key player in endocytosis. Importantly, actin assists at the remodelling of the cell surface to allow inward movement of vesicles (Smythe and Ayscough 2006). In the context of SMA, we have previously reported that SMN-depleted cells show reduced F-actin amounts and therefore, we hypothesized that this effect could be due to a disturbed transport of ß-actin mRNA along

the axons (Ackermann et al. 2013; Gabanella et al. 2016; Oprea et al. 2008). In several animal models of SMA it could be demonstrated that many F-actin-dependent processes are impaired, including axonal growth, proper NMJ connectivity, neurotransmission, synaptic-vesicle recycling and proprioceptive inputs at MN soma (Ackermann et al. 2013; Mentis et al. 2011; Oprea et al. 2008; McWhorter et al. 2003; Dimitriadi et al. 2010). All of these defects could be either ameliorated or completely restored by PLS3 overexpression (Oprea et al. 2008; Ackermann et al. 2013; Hao le et al. 2012). In section 5.13, we have demonstrated that reduced SMN levels lead to reduced endocytosis in murine embryonic fibroblasts, which could be restored by PLS3 overexpression. Moreover, we have recently reported that this finding also applies to NSC34 cells and at the NMJs, as shown by FM1-43 endocytic uptake under low- (Figure 41) and high-frequency (Figure 42) conditions. As PLS3 rescued disturbed endocytosis under both conditions, we confirmed that it is involved in clathrin-mediated endocytosis (CME), as well as clathrin-independent endocytosis (CIE) or activity-dependent bulk endocytosis (ADBE). PLS3 restored endocytosis and the SMA-related phenotype in mouse and/or zebrafish and similar to the findings in yeast, siRNA-mediated knockdown of PLS3 reduced endocytic uptake in various cell types (Hosseinibarkooie et al. 2016). In SMA mice, reduced F-actin amounts lead to reduced numbers of vesicles in the readily releasable pool of synaptic vesicles, which are needed for proper neurotransmission. Their size is smaller and the depletion and refilling time constants tend to be slower (Torres-Benito et al. 2012). F-actin is a crucial player in all types of endocytosis (Mooren et al. 2012; Doherty and McMahon 2009), and its inhibition reduces the endocytosis in neurons under high-rate stimulation (Watanabe et al. 2013). Our recently published data underline these findings and support the idea that PLS3 overexpression is able to rescue the impaired endocytosis in SMA through the crucial role of F-actin in endocytosis (Hosseinibarkooie et al. 2016). As the calcium-binding ability of PLS3 via its EF-hands (Lyon et al. 2014) seems to be essential for PLS3 to compensate for SMN loss, we hypothesized that decreased endocytosis might be a result of combined reduced calcium influx and F-actin dynamics (See et al. 2014). The fact that SMA MNs show disturbed calcium homeostasis (Ruiz et al. 2010) further strengthens this concept.

6.7   THE POWER OF GENETIC MODIFIERS

This work is an outstanding example of how the power of genetic modifiers can be used as a precise tool to identify key cellular mechanisms, molecular pathways and protein networks that successfully inhibit or counteract the disease-causing genes and/or processes. Figure 43 shows a model of the compensatory role of PLS3 and Coronin1C (CORO1C: an interacting partner of PLS3 and an additional disease modifier of SMA) in the process of endocytosis in SMA (Hosseinibarkooie et al. 2016). Our gained knowledge about these modifiers might pave the way for the development of new therapeutic strategies targeting the affected endocytic mechanism in SMA in addition to pharmacological compounds that induce SMN expression or stability.
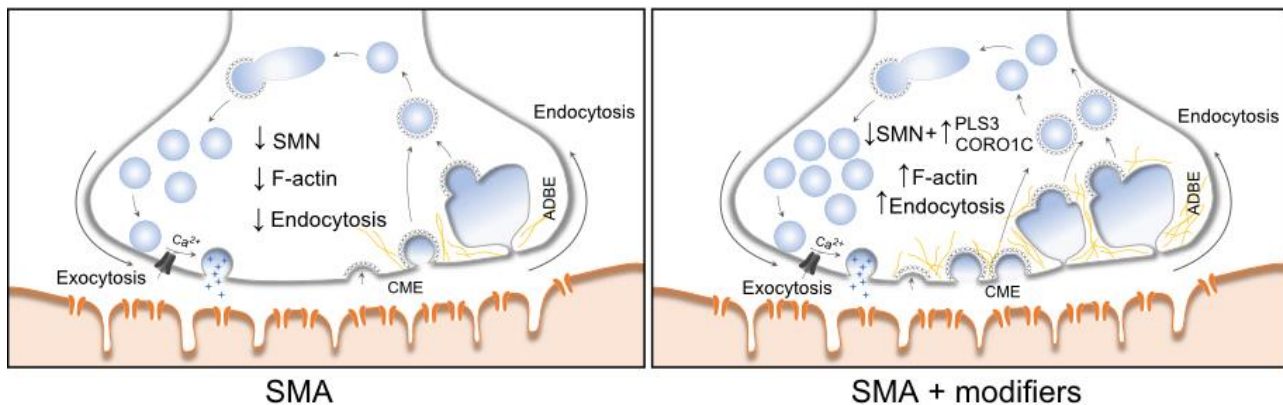
Figure 43: A model presenting the compensatory role of PLS3 and CORO1C in the process of endocytosis in SMA. CME and ADBE stand for clathrin-mediated endocytosis and activity-dependent bulk endocytosis, respectively. (Taken from (Hosseinibarkooie et al. 2016).)

In a more general context of genetic modifiers, it is important to investigate their mode of action as well as their role within the pathway or protein network in the context of the disease-causing gene. This means that the modifying genes can act upstream or downstream of the disease-causing gene, by either influencing their expression and/or function or compensating for imbalances and defects in a pathway affected by them, respectively. Their compensation can be directly within the affected protein complex or totally independent. Numerous pathogenic mutations have been unexpectedly identified in healthy individuals, opening a fully now era and allowing us to better understand diverse counteracting protein networks and their regulation, which ultimately will result in development of novel therapeutic strategies (Hosseinibarkooie et al. 2016).

6.8   OUTLOOK

Identification of PLS3 as a first SMN-independent protective modifier is a starting point to develop new treatment strategies for neurodegenerative disorders including SMA, Parkinson or ALS. PLS3 did not only help to identify endocytosis as a main cellular pathway disturbed in SMA pathology but also provided a more detailed insight into the molecular mechanisms and the protein networks, in which PLS3 and the disease-causing *SMN1* gene are involved.

In the meanwhile, additional asymptomatic *SMN1*-deleted individuals had been identified. Most interestingly, in these cases PLS3 upregulation has been excluded.

(1) There is a good reason to assume that other SMA modifiers do exist within the human population (Bernal et al. 2011) and unpublished data from our lab confirmed that at least one additional modifier is also improving the SMA phenotype via the endocytosis pathway (Riessland et al, AJHG, under review 2016).

(2) In an additional screening for SMA modifiers, several other modifiers with direct roles in endocytosis have been identified in worm (Dimitriadi et al. 2010). Further studies are required to properly understand the major impaired type of endocytosis as well as other modifying factors (in addition to reduced F-actin amounts in the presynapse) that determine the endocytic traffic in SMA.

(3) As described in section 1.1.6, several other research groups successfully generated different intermediate mouse models that are not drug-induced but genetically engineered. These could also be relevant for future studies of modifiers and drug design (Bogdanik et al. 2015).

(4) In this context, the advantages and weaknesses of pharmacologically induced intermediate SMA animal models versus genetically engineered ones (also see section 1.1.6) need to be discussed and evaluated in future studies.

(5) As a side effect, while studying SMA pathology in intermediate SMA mouse models, an extraordinary progress has been achieved in the development of using antisense oligonucleotides (ASOs) such as morpholinos or RNAs (Lim and Hertel 2001; Cartegni and Krainer 2003; Dickson et al. 2008; Hua et al. 2010; Hua et al. 2011) in order to correct the *SMN2* splicing pattern towards increased levels of FL-*SMN* transcripts (see also section 1.1.7). In future studies, the idea of individual drug design to target specific

dysfunctions such as the *SMN2* splicing defect (Rigo et al. 2012) should also be translated to extenuate pathomechanisms in other neurodegenerative pathologies equally successfully. They are currently used in ongoing clinical trials in SMA type I to III patients (http://www.clinicaltrials.gov). Further outcome of these studies can give new input for development of target-specific drug-design.

(6) New NGS technologies may help with the development of future studies in healthy individuals carrying pathogenic mutations in order to unravel new protective modifiers and eventually help to understand disease-relevant pathways in humans (Hosseinibarkooie et al. 2016).

Firstly, we used SMN-ASO injection as a means to induce an intermediate phenotype in the severely affected Taiwanese SMA mice to establish an animal model with a certain SMN threshold that resembles more the situation in asymptomatic *SMN1*-deleted individuals. Secondly, we thereby learned from our model that combined therapy of suboptimal doses of SMN-ASO in addition to compounds that either directly elevate PLS3 levels or compensate for the defects in the pathway of endocytosis, might be a logical strategy for future clinical trials.

7. Summary

Spinal muscular atrophy (SMA) is an autosomal recessive neurodegenerative disorder characterized by the loss of α-motor neurons in the anterior horns of the spinal cord. This leads to atrophy of proximal symmetrical muscles and paralysis. Patients suffering from SMA in almost all cases show homozygous absence of the *survival of motor neuron 1* gene (*SMN1*) and the severity of the disease is inversely correlated with the copy number of the main disease modifying gene *survival motor neuron 2* (*SMN2*).

Rarely, individuals with homozygous *SMN1*-deletion remain asymptomatic, suggesting the action of modifying gene(s). Plastin 3 (PLS3) – a F-actin binding and bundling protein - has been identified as a protective modifier showing high expression in *SMN1*-deleted asymptomatic siblings of SMA patients. PLS3 is highly expressed in spinal cord and axonal growth cones. PLS3 overexpression rescues the axonal outgrowth phenotype in SMA motor neuron cultures and SMA zebrafish (Oprea et al. 2008). Severely affected SMA mice carrying heterozygously a transgenic PLS3 overexpressing allele show improved motoric abilities as a consequence of improved innervation at neuromuscular junctions (NMJ), increased NMJs and muscle fibre size as well as an increase of proprioceptive input on motor neuron (MN) soma. Most importantly, PLS3 overexpression delays axon pruning and improves connectivity of the presynapse to motor endplates. Nonetheless, survival is only marginally increased by a few days, as a consequence of massive impairment of inner organs in SMA mice, which is not rescued by PLS3 overexpression (Ackermann et al. 2013). As PLS3 overexpression ameliorates some SMA hallmarks in the severe SMA mouse model, but its modifying function is likely diminished by the multi-organ impairment, we decided to study the effect of elevated PLS3 in an intermediate SMA mouse model, which would more faithfully model the condition of initially identified asymptomatic individuals. To do so, we made use of a low dose SMN-antisense oligonucleotide (ASO) that allows *SMN2* splice correction (Hua et al. 2011).

In this study, (1) an intermediately-affected SMA mouse model was produced by presymptomatic subcutaneous injection of low dose SMN-ASOs into the severely-affected SMA mouse model; (2) SMN-ASO treated SMA mice on congenic FVB/N background showed a much larger variability in survival than on C57BL/6N background. (3) The optimal conditions turned out to be 30 µg SMN-ASO, injected twice at P2 and P3 in C57BL/6N SMA mice. These mice showed an elongated lifespan from 14 to 28 days. (4) The suboptimal

doses of SMN-ASO considerably decreased inner organ defects including intestine, lung and heart. (5) Additional overexpression of the PLS3 transgene either heterozygously or homozygously rescued survival from 28 to >250 days, weight and motoric abilities (grip strength force and tube test). These data proved that PLS3 is a protective modifier of SMA if elevated in an animal model that resembles the situation in the asymptomatic *SMN1*-deleted individuals. (6) In this low dose SMN-ASO injected intermediate SMA mouse model, PLS3 counteracts the defects within the neuronal circuitry by increasing NMJ size and thereby stabilizing AChR clustering at the postsynaptic site. Presynaptically, PLS3 increases the number of proprioceptive inputs at the MN soma and leads to enlarged MN soma size. (7) Even in MNs isolated from the severely affected SMA mouse model, PLS3 overexpression led to an increased length of the main axon. (8) As PLS3 knockout in yeast impairs endocytosis (Kubler and Riezman 1993), we hypothesized that disturbed endocytosis might be a key cellular mechanism underlying impaired neurotransmission and neuromuscular junction maintenance in SMA. Indeed, SMN deficit dramatically reduced endocytosis in murine embryonic fibroblasts, which was restored to control levels by overexpression of PLS3.

Taken together, our findings in transgenic SMA mice demonstrate the efficacy of a combined treatment with SMN-ASO in addition to PLS3 overexpression, rather than solely increasing SMN levels. Hence, we suggest that compounds, which can restore endocytosis in combination with SMN-ASO therapy might not only improve the SMA phenotype but maybe even result in a complete rescue, and this possibility will be tested in future studies.

8. Zusammenfassung

Die spinale Muskelathrophie (SMA) ist eine autosomal rezessive neurodegenerative Erkrankung, die durch den Verlust von α-Motoneuronen in den ventralen Hörnern des Rückenmarks charakterisiert ist. Dies führt zum Muskelschwund der proximalen symmetrischen Muskeln mit einhergehenden Lähmungserscheinungen. Patienten, die an SMA erkrankt sind, weisen nahezu immer einen homozygoten Verlust des *Survival of motor neuron 1* Gens (*SMN1*) auf und es gibt eine reziproke Korrelation zwischen dem Schweregrad der Erkrankung und der Kopienzahl des primären modifizierenden Gens, *Survival of motor neuron 2* (*SMN2*).

In seltenen Fällen bleiben jedoch Menschen, die einen homozygoten *SMN1* Verlust aufweisen, asymptomatisch, was auf die Anwesenheit weiterer modifizierender Gene schließen lässt. Plastin 3 (PLS3) – ein F-Aktin-bündelndes und -bindendes Protein – wurde als solch ein protektives krankheitsmodifizierendes Gen identifiziert, indem es in den *SMN1*-negativen asymptomatischen Geschwistern von SMA Patienten besonders stark exprimiert wurde. Es stellte sich heraus, dass PLS3 sehr stark im Rückenmark und in den axonalen Wachstumsknospen exprimiert wird. Die Überexpression von PLS3 stabilisiert das axonale Längenwachstum in SMA Motoneuronkulturen und im SMA Zebrafischmodell (Oprea et al. 2008). Schwer erkrankte SMA Mäuse, die heterozygot ein PLS3 überexprimierendes Transgen tragen, zeigen verbesserte motorische Fähigkeiten in Folge von verbesserter Innervierung und vergrößerter Fläche der neuromuskulären Endplatten und größeren Muskelfasern, ebenso wie von erhöhten afferenten Synapsen auf den Zellkörpern der Motoneurone. Hervorzuheben ist, dass die Überexpression von PLS3 die axonale Rückbildung verzögert und somit die Verbindung der Präsynapse zur motorischen Endplatte unterstützt. Nichtsdestotrotz, die PLS3-Überexpression erhöhte die Überlebensrate der SMA Mäuse nur gering um wenige Tage, aufgrund von extremen Defekten der inneren Organe in SMA Mäusen, welche nicht verbessert werden konnten (Ackermann et al. 2013). Da PLS3-Überexpression einige SMA Merkmale im schwer betroffenen Mausmodell verbesserte, jedoch in seiner Funktion als modifizierendes Gen durch das Versagen mehrerer Organe abgeschwächt wurde, entschieden wir, den Effekt des PLS3-Anstiegs in einem intermediären SMA Mausmodell zu studieren, das besser den Phänotyp der asymptomatischen Menschen wiederspiegelt. Hierzu verwendeten wir geringe Mengen

eines SMN-Antisense-Oligonukleotids (ASO), das einen Defekt im *SMN2* Splicing korrigiert (Hua et al. 2011).

In der vorliegenden Arbeit wurden folgende Erkenntnisse hervorgebracht: (1) Durch präsymptomatische subkutane Injektion geringer Mengen SMN-ASOs in das schwer betroffene SMA Mausmodell haben wir ein mittelschwer betroffenes SMA Mausmodell entwickelt; (2) Die SMN-ASO behandelte Mäuse zeigten auf einem kongenen FVB/N Hintergrund stärkere Schwankungen in der Überlebensrate als auf einem C57BL/6N Hintergrund; (3) Wir haben als die optimale Applikation des SMN-ASOs in C57BL/6N SMA Mäuse eine Injektion von 30 µg an den Tagen P2 und P3 erarbeitet. Die Überlebensrate in den SMN-ASO injizierten Mäusen wurden von 14 auf 28 Tage verlängert; (4) Bereits diese suboptimale Dosis von SMN-ASO verringerte beträchtlich die Defekte der inneren Organe, einschließlich Darm, Lunge und Herz; (5) Zusätzliche hetero- oder homozygote Überexpression des PLS3 Transgens erhöhte die Überlebensrate von 28 auf >250 Tage, verbesserte die Gewichtszunahme und die motorischen Fähigkeiten. Dies bestätigt die Funktion von PLS3 als ein protektives modifizierendes Gen gegen SMA, sobald es in einem Tiermodell überexprimiert wird, das besser der Ausgangssituation der asymptomatischen *SMN1*-negativen Menschen entspricht; (6) In diesem SMN-ASO-induzierten intermediären SMA Mausmodell steuert die PLS3 Überexpression den Defekten innerhalb des neuronalen Schaltungskreises durch eine Vergrößerung der motorischen Endplatte und einer damit einhergehenden Stabilisierung der postsynaptischen AChR Clusters, entgegen. Präsynaptisch erhöht PLS3 die Anzahl der afferenten Synapsen an die Zellkörper der Motoneurone und führt zu einer Vergrößerung der motoneuronalen Zellkörper; (7) Interessanterweise führt die PLS3 Überexprimierung selbst in Motoneuronen, die aus schwer betroffenen SMA Mausembryonen isoliert wurden, zu einem verlängerten Hauptaxon; (8) Da PLS3 Knockout die Endozytose in Hefen negativ beeinträchtigt (Kubler and Riezman 1993), stellten wir die Hypothese auf, dass der Defekt der Endozytose einer der Hauptstoffwechselmechanismen sein könnte, der die Beeinträchtigungen bei der Neurotransmission und an der neuromuskulären Endplatte bei SMA erklärt. Tatsächlich stellten wir fest, dass SMN Defizite zu einer verringerten Endozytose in murinen embryonalen Fibroblasten führen, während die PLS3-Überexpression wieder zu einer Normalisierung des Endozytose führte.

Zusammenfassend zeigen unsere Erkenntnisse in der transgenen SMA Maus auf, dass eine kombinierte Behandlung mit SMN-ASO zusätzlich zur PLS3 Überexpression effizienter

wirkt, als eine alleinige Erhöhung der SMN Menge. Folglich weist dies darauf hin, dass Substanzen, welche die Endozytose verbessern können, in Kombination mit SMN-ASO Therapie nicht nur den SMA Phänotyp verbessern, sondern vielleicht sogar zu einer vollständigen Heilung der Krankheit führen könnten. Diese Hypothese stellt eine Grundlage für zukünftige Studien dar.

9. Publications and Poster Contributions

<u>Original Publications:</u>

The Power of Human Protective Modifiers: PLS3 and CORO1C Unravel Impaired Endocytosis in Spinal Muscular Atrophy and Rescue SMA Phenotype

Seyyedmohsen Hosseinibarkooie[*], **Miriam Peters**[*], Laura Torres-Benito, Raphael H. Rastetter, Kristina Hupperich, Andrea Hoffmann, Natalia Mendoza-Ferreira, Anna Kaczmarek, Eva Janzen, Janine Milbradt, Tobias Lamkemeyer, Frank Rigo, C. Frank Bennett, Christoph Guschlbauer, Ansgar Büschges, Matthias Hammerschmidt, Markus Riessland, Min Jeong Kye, Christoph S. Clemen, Brunhilde Wirth

[*]**These authors contributed equally to this work**

Am J Hum Genet. 2016 Sep 1;99(3):647-65. doi: 10.1016/j.ajhg.2016.07.014. Epub 2016 Aug 4.

SMN regulates axonal local translation via miR-183/mTOR pathway.

Kye MJ, Niederst ED, Wertz MH, Gonçalves Ido C, Akten B, Dover KZ, **Peters M**, Riessland M, Neveu P, Wirth B, Kosik KS, Sardi SP, Monani UR, Passini MA, Sahin M.

Hum Mol Genet. 2014 Dec 1;23(23):6318-31. doi: 10.1093/hmg/ddu350. Epub 2014 Jul 4.

Plastin 3 ameliorates spinal muscular atrophy via delayed axon pruning and improves neuromuscular junction functionality.

Ackermann B1, Kröber S, Torres-Benito L, Borgmann A, **Peters M**, Hosseini Barkooie SM, Tejero R, Jakubik M, Schreml J, Milbradt J, Wunderlich TF, Riessland M, Tabares L, Wirth B.

Hum Mol Genet. 2013 Apr 1;22(7):1328-47. doi: 10.1093/hmg/dds540. Epub 2012 Dec 20.

<u>Printed Posters:</u>

Calcineurin-Like EF-Hand Protein rescues the impaired endocytosis in an in vitro model of spinal muscular atrophy

Eva Janzen, Seyyed Mohsen Hosseini Barkooie, Natalia Mendoza Ferreira, **Miriam Peters**, Kristina Hupperich, Vanessa Grysko, Svenja Schneider, Laura Torres-Benito, Markus Riessland and Brunhilde Wirth

12- 17 June 2016: Lysosomes and Endocytosis. Gordon Research Conference. 2016, Harvard Universtiy, Boston, MA (USA)

Deregulated Calcium Signalling and Homeostasis in Spinal Muscular Atrophy

Torres-Benito, L.; Mendoza-Ferreira, N; **Peters, M**; Riessland, M; Bradler, C; Kloppenburg, P.; Wirth, B.

2016: AFM Theleton 2016, Kansas City, MO (USA)

SMA modifiers: Plastin 3 and CORO1C rescue the SMA phenotype through an actin-endocytosis dependent process

Seyyedmohsen Hosseinibarkooie, **Miriam Peters**, Laura Torres-Benito, Raphael Rastetter, Eva Janzen, Min Jeong Kye, Tobias Lamkaemeyer, Matthias Hammerschmidt, Christoph Clemen, Markus Riessland, and Brunhilde Wirth

18-21 June 2015: 19th FSMA Annual Researcher Meeting, Kansas City, MO (USA)

Homozygous PLS3 overexpression in intermediate SMA mice rescues phenotype and survival

Miriam Peters, Kristina Hupperich, Andrea Hoffmann, Seyedmohsen Hosseinibarkooie, Laura Torres-Benito, Anna Kaczmarek, Janine Milbradt, Min Jeong Kye, Frank Rigo, Frank Bennett, Markus Riessland and Brunhilde Wirth

19.06.2015: 19th FSMA Annual Researcher Meeting, The Westin Crown Center, Kansas City, MO

Plastin 3, a human protective modifier is highly upregulated in iPSC-derived motoneurons in asymptomatic SMN1-deteted individuals and rescues spinal muscular atrophy in mice by restored endocytosis

Hosseinibarkooie SM, **Peters M**, Torres-Benito L, Heesen L, Peitz M, Markus S. Kaczmarek A, Kye MJ, Brüstle O, Wirth B

2015: 26. Jahrestagung der Deutschen Gesellschaft für Humangenetik, Lübeck, Germany

Calcineurin homologous protein 1, a Plastin 3 Binding Partner and Potential Modifier of Spinal Muscular Atrophy

Eva Janzen, SeyyedMohsen Hosseini-Barkooie, Natalia Mendoza Ferreira, **Miriam Peters**, Markus Riessland and BrunhildeWirth

2015: ESHG, Bertinoro, Italy

In vivo analysis of a PLS3 overexpression in two different intermediate mouse models of SMA

Miriam Peters; Kristina Hupperich; Bastian Ackermann; Seyed Mohsen Hosseini Barkooie; Janine Milbradt; Sandra Kröber; Markus Riessland; and Brunhilde Wirth

23.05.2014: 5th Annual Human Genetics meeting, Universität zu Köln, Cologne, Germany

Osteoporosis: Filamentous-actin bundling, a novel mechanism underlying bone development

Milbradt J, Dimitra M, Riessland M, Hamann N, van Dijk FS, **Peters M**, Mendoza-Ferreira N, Hosseini-Barkooie M, Hammerschmidt M, Niehoff A, Pals G, Wirth B.

Conference: **2014 Jan:** Gordon Research Conference Bones and Teeth, At Galveston, TX, USA

Plastin 3 ameliorates synaptic defects in Spinal Muscular Atrophy

Rocío Tejero, Bastian Ackermann, Sandra Kröber, Laura Torres-Benito, Anke Borgmann, **Miriam Peters**, Seyyed Mohsen Hosseini Barkooie, Miriam Jakubik, Julia Schreml, Janine Milbradt, Thomas F. Wunderlich, Markus Riessland, Lucia Tabares and Brunhilde Wirth

7-9 Oct 2013: Current Trends in Biomedicine: Membrane Traffic at the Synapse. The Cell Biology of Synaptic Plasticity, Baeza (Spain)

In vivo **analysis of homozygous PLS3 overexpression in a mouse model of SMA and** *in vitro* **studies of several putative PLS3 interaction partners**

Miriam Peters; Bastian Ackermann; Seyed Mohsen Hosseini Barkooie, Sandra Kröber; Markus Riessland; and Brunhilde Wirth

29.11.2012: 4th **Annual Human Genetics meeting**, Universität zu Köln, Cologne, Germany

Printed Abstracts:

Plastin 3, a human protective modifier is highly upregulated in iPSC-derived motoneurons in asymptomatic *SMN1*-**deteted individuals and rescues spinal muscular atrophy in mice**

Wirth B, **Peters M**, Heesen L, Hosseini Barkooie SM, Peitz M, Kaczmarek A, Janzen E, Torres Benito L, Brüstle O

10.11.2016: ICHG 2016, Kyoto, Japan

The power of protective modifiers in human genetics: Plastin3 and Coronin1C unravel endocytosis as an essential cellular mechanism disturbed in spinal muscular atrophy

SM. Hosseinibarkooie, **M. Peters**, L. Torres-Benito, R. Rastetter, K. Hupperich, A. Hoffmann, N. Mendoza-Ferreira, A. Kaczmarek, E. Janzen, J. Milbradt, T. Lamkaemeyer, F. Rigo, F. Bennett, C. Guschlbauer, A. Büschges, M. Hammerschmidt, M. Riessland, MJ. Kye, C. Clemen and B. Wirth

16-19 June 2016: 20th **Annual SMA Conference. Anaheim**, CA (USA)

The power of protective modifiers in human genetics: Plastin3 and Coronin1C unravel endocytosis as an essential cellular mechanism disturbed in spinal muscular atrophy

L. Torres-Benito, SM. Hosseinibarkooie, **M. Peters**, R. Rastetter, K. Hupperich, A. Hoffmann, N. Mendoza-Ferreira, A. Kaczmarek, E. Janzen, T. Lamkaemeyer C. Guschlbauer, A. Büschges, M. Hammerschmidt, M. Riessland, MJ. Kye, C. Clemen, and B. Wirth

21 -24 May 2016: The European Human Genetics Conference 2016, Barcelona, (Spain)

Neuronal hyperactivity inhibits Drosha expression via autophagy-lysosome pathway in spinal muscular atrophy

Ines do Carmo Gil Goncalves, Johanna Brecht, **Miriam Peters**, Laura Torres-Benito, Darius Ebrahimi-Fakhari, Mustafa Sahin, Brunhilde Wirth and Min Jeong Kye

2016: The RNA Neurodegenerative Conference 2016, SanDiego, California (USA)

Plastin 3, a human protective modifier is highly upregulated in iPSC-derived motoneurons in asymptomatic *SMN1*-**deteted individuals and rescues spinal muscular atrophy in mice by restored endocytosis**

Hosseinibarkooie SM, **Peters M**, Torres-Benito L, Heesen L, Peitz M, Markus S. Kaczmarek A, Kye MJ, Brüstle O, Wirth B

29.11.2015: GfH 2015, Lübeck, Germany

Plastin 3, a human protective modifier is highly upregulated in IPSC-derived motor neurons in asymptomatic individuals and rescues spinal muscular atrophy in mice

Peters M, Heesen L, Hosseini Barkooie SM, Peitz M, Kaczmarek A, Janzen E, Brüstle O and Wirth B

2015: ESHG 2015, Glasgow, Great Britain

Mutations in *PLS3* causes osteoporosis with fractures. Overexpression of PLS3 and other F-actin bundling proteins influence skeletal development in zebrafish and mice

B. Wirth, J. Milbradt, D. Micha4, M. Riessland, N. Hamann, F. van Dijk, **M. Peters**, N. Mendoza-Ferreira, S.M. Hosseini Barkooie, E. Janzen, C.M. Zillikens, M. Hammerschmidt, A. Niehoff, G. Pals

2014: ASHG 2014, SanDiego, California (USA)

Mutations in *PLS3* causes osteoporosis with fractures. Overexpression of PLS3 and other F-actin bundling proteins influence skeletal development in zebrafish and mice

J. Milbradt, M. Dimitra, M. Riessland, N. Hamann, F. van Dijk, **M. Peters**, N. Mendoza Ferreira, M. S. Hosseini Barkooie, E. Janzen, M. C. Zillikens, M. Hammerschmidt, A. Niehoff, G. Pals, B. Wirth

2014: ESHG 2014, Milan, Italy

Further insight into the rescuing function of PLS3 and its binding partner in SMA

Seyed Mohsen Hosseini Barkooie, Raphael Rastetter, **Miriam Peters**, Eva Janzen, Bastian Ackerman, Min Jeong Key, Tobias Lamkemeyer, Matthias Hammerschmidt, Christoph Clemen, Markus Riessland, and Brunhilde Wirth

2014: NeurOmics 2014, Heidelberg, Germany

Plastin 3 ameliorates spinal muscular atrophy via delayed axon pruning and improves neuromuscular junction functionality

B. Ackermann, S. Kröber, L. Torres-Benito, A. Borgmann, **M. Peters**, S. Hosseini Barkooie, R. Tejero, M. Jakubik, J. Schreml, J. Milbradt, T. F. Wunderlich, M. Riessland, L. Tabares, B. Wirth

2013: ESHG 2013, Paris, France

10.   References

Ackermann B, Krober S, Torres-Benito L, Borgmann A, Peters M, Hosseini Barkooie SM, Tejero R, Jakubik M, Schreml J, Milbradt J, Wunderlich TF, Riessland M, Tabares L, Wirth B (2013) Plastin 3 ameliorates spinal muscular atrophy via delayed axon pruning and improves neuromuscular junction functionality. Hum Mol Genet 22 (7):1328-1347

Amatruda JF, Cooper JA (1992) Purification, characterization, and immunofluorescence localization of Saccharomyces cerevisiae capping protein. J Cell Biol 117 (5):1067-1076

Andreassi C, Angelozzi C, Tiziano FD, Vitali T, De Vincenzi E, Boninsegna A, Villanova M, Bertini E, Pini A, Neri G, Brahe C (2004) Phenylbutyrate increases SMN expression in vitro: relevance for treatment of spinal muscular atrophy. Eur J Hum Genet 12 (1):59-65

Avila AM, Burnett BG, Taye AA, Gabanella F, Knight MA, Hartenstein P, Cizman Z, Di Prospero NA, Pellizzoni L, Fischbeck KH, Sumner CJ (2007) Trichostatin A increases SMN expression and survival in a mouse model of spinal muscular atrophy. J Clin Invest 117 (3):659-671

Bardoni B, Schenck A, Mandel JL (2001) The Fragile X mental retardation protein. Brain Res Bull 56 (3-4):375-382

Baumbach-Reardon L, Sacharow S, Ahearn ME (1993) Spinal Muscular Atrophy, X-Linked Infantile. In: Pagon RA, Adam MP, Ardinger HH et al. (eds) GeneReviews(R). Seattle (WA),

Benkhelifa-Ziyyat S, Besse A, Roda M, Duque S, Astord S, Carcenac R, Marais T, Barkats M (2013) Intramuscular scAAV9-SMN injection mediates widespread gene delivery to the spinal cord and decreases disease severity in SMA mice. Mol Ther 21 (2):282-290. doi:10.1038/mt.2012.261

Bennett CF, Swayze EE (2010) RNA targeting therapeutics: molecular mechanisms of antisense oligonucleotides as a therapeutic platform. Annu Rev Pharmacol Toxicol 50:259-293. doi:10.1146/annurev.pharmtox.010909.105654

Bernal S, Also-Rallo E, Martinez-Hernandez R, Alias L, Rodriguez-Alvarez FJ, Millan JM, Hernandez-Chico C, Baiget M, Tizzano EF (2011) Plastin 3 expression in discordant spinal muscular atrophy (SMA) siblings. Neuromuscul Disord 21 (6):413-419

Bertrandy S, Burlet P, Clermont O, Huber C, Fondrat C, Thierry-Mieg D, Munnich A, Lefebvre S (1999) The RNA-binding properties of SMN: deletion analysis of the zebrafish orthologue defines domains conserved in evolution. Hum Mol Genet 8 (5):775-782

Bevan AK, Hutchinson KR, Foust KD, Braun L, McGovern VL, Schmelzer L, Ward JG, Petruska JC, Lucchesi PA, Burghes AH, Kaspar BK (2010) Early heart failure in the SMNDelta7 model of spinal muscular atrophy and correction by postnatal scAAV9-SMN delivery. Hum Mol Genet 19 (20):3895-3905

Bishop DL, Misgeld T, Walsh MK, Gan WB, Lichtman JW (2004) Axon branch removal at developing synapses by axosome shedding. Neuron 44 (4):651-661. doi:10.1016/j.neuron.2004.10.026

Blanchoin L, Boujemaa-Paterski R, Sykes C, Plastino J (2014) Actin dynamics, architecture, and mechanics in cell motility. Physiological reviews 94 (1):235-263. doi:10.1152/physrev.00018.2013

Bogdanik LP, Osborne MA, Davis C, Martin WP, Austin A, Rigo F, Bennett CF, Lutz CM (2015) Systemic, postsymptomatic antisense oligonucleotide rescues motor unit

maturation delay in a new mouse model for type II/III spinal muscular atrophy. Proc Natl Acad Sci U S A 112 (43):E5863-5872. doi:10.1073/pnas.1509758112

Bowerman M, Anderson CL, Beauvais A, Boyl PP, Witke W, Kothary R (2009) SMN, profilin IIa and plastin 3: a link between the deregulation of actin dynamics and SMA pathogenesis. Mol Cell Neurosci 42 (1):66-74

Bowerman M, Murray LM, Beauvais A, Pinheiro B, Kothary R (2012a) A critical smn threshold in mice dictates onset of an intermediate spinal muscular atrophy phenotype associated with a distinct neuromuscular junction pathology. Neuromuscul Disord 22 (3):263-276

Bowerman M, Shafey D, Kothary R (2007) Smn depletion alters profilin II expression and leads to upregulation of the RhoA/ROCK pathway and defects in neuronal integrity. J Mol Neurosci 32 (2):120-131

Bowerman M, Swoboda KJ, Michalski JP, Wang GS, Reeks C, Beauvais A, Murphy K, Woulfe J, Screaton RA, Scott FW, Kothary R (2012b) Glucose metabolism and pancreatic defects in spinal muscular atrophy. Ann Neurol 72 (2):256-268. doi:10.1002/ana.23582

Bradke F, Dotti CG (1999) The role of local actin instability in axon formation. Science 283 (5409):1931-1934

Brahe C, Servidei S, Zappata S, Ricci E, Tonali P, Neri G (1995) Genetic homogeneity between childhood-onset and adult-onset autosomal recessive spinal muscular atrophy. Lancet 346 (8977):741-742

Brahe C, Vitali T, Tiziano FD, Angelozzi C, Pinto AM, Borgo F, Moscato U, Bertini E, Mercuri E, Neri G (2005) Phenylbutyrate increases SMN gene expression in spinal muscular atrophy patients. Eur J Hum Genet 13 (2):256-259

Brichta L, Hofmann Y, Hahnen E, Siebzehnrubl FA, Raschke H, Blumcke I, Eyupoglu IY, Wirth B (2003) Valproic acid increases the SMN2 protein level: a well-known drug as a potential therapy for spinal muscular atrophy. Hum Mol Genet 12 (19):2481-2489

Brichta L, Holker I, Haug K, Klockgether T, Wirth B (2006) In vivo activation of SMN in spinal muscular atrophy carriers and patients treated with valproate. Ann Neurol 59 (6):970-975

Brzustowicz LM, Lehner T, Castilla LH, Penchaszadeh GK, Wilhelmsen KC, Daniels R, Davies KE, Leppert M, Ziter F, Wood D, et al. (1990) Genetic mapping of chronic childhood-onset spinal muscular atrophy to chromosome 5q11.2-13.3. Nature 344 (6266):540-541

Burglen L, Lefebvre S, Clermont O, Burlet P, Viollet L, Cruaud C, Munnich A, Melki J (1996) Structure and organization of the human survival motor neurone (SMN) gene. Genomics 32 (3):479-482

Burlet P, Huber C, Bertrandy S, Ludosky MA, Zwaenepoel I, Clermont O, Roume J, Delezoide AL, Cartaud J, Munnich A, Lefebvre S (1998) The distribution of SMN protein complex in human fetal tissues and its alteration in spinal muscular atrophy. Hum Mol Genet 7 (12):1927-1933

Burnett BG, Munoz E, Tandon A, Kwon DY, Sumner CJ, Fischbeck KH (2009) Regulation of SMN protein stability. Mol Cell Biol 29 (5):1107-1115

Butchbach ME, Rose FF, Jr., Rhoades S, Marston J, McCrone JT, Sinnott R, Lorson CL (2010) Effect of diet on the survival and phenotype of a mouse model for spinal muscular atrophy. Biochem Biophys Res Commun 391 (1):835-840. doi:10.1016/j.bbrc.2009.11.148

Carre A, Empey C (2016) Review of Spinal Muscular Atrophy (SMA) for Prenatal and Pediatric Genetic Counselors. J Genet Couns 25 (1):32-43. doi:10.1007/s10897-015-9859-z

Cartegni L, Krainer AR (2002) Disruption of an SF2/ASF-dependent exonic splicing enhancer in SMN2 causes spinal muscular atrophy in the absence of SMN1. Nat Genet 30 (4):377-384

Cartegni L, Krainer AR (2003) Correction of disease-associated exon skipping by synthetic exon-specific activators. Nat Struct Biol 10 (2):120-125

Carvalho T, Almeida F, Calapez A, Lafarga M, Berciano MT, Carmo-Fonseca M (1999) The spinal muscular atrophy disease gene product, SMN: A link between snRNP biogenesis and the Cajal (coiled) body. J Cell Biol 147 (4):715-728

Chan YB, Miguel-Aliaga I, Franks C, Thomas N, Trulzsch B, Sattelle DB, Davies KE, van den Heuvel M (2003) Neuromuscular defects in a Drosophila survival motor neuron gene mutant. Hum Mol Genet 12 (12):1367-1376

Chang HC, Hung WC, Chuang YJ, Jong YJ (2004) Degradation of survival motor neuron (SMN) protein is mediated via the ubiquitin/proteasome pathway. Neurochem Int 45 (7):1107-1112. doi:10.1016/j.neuint.2004.04.005

Chang JG, Hsieh-Li HM, Jong YJ, Wang NM, Tsai CH, Li H (2001) Treatment of spinal muscular atrophy by sodium butyrate. Proc Natl Acad Sci U S A 98 (17):9808-9813

Chen Q, Baird SD, Mahadevan M, Besner-Johnston A, Farahani R, Xuan J, Kang X, Lefebvre C, Ikeda JE, Korneluk RG, MacKenzie AE (1998) Sequence of a 131-kb region of 5q13.1 containing the spinal muscular atrophy candidate genes SMN and NAIP. Genomics 48 (1):121-127

Cho S, Dreyfuss G (2010) A degron created by SMN2 exon 7 skipping is a principal contributor to spinal muscular atrophy severity. Genes Dev 24 (5):438-442

Cifuentes-Diaz C, Frugier T, Tiziano FD, Lacene E, Roblot N, Joshi V, Moreau MH, Melki J (2001) Deletion of murine SMN exon 7 directed to skeletal muscle leads to severe muscular dystrophy. J Cell Biol 152 (5):1107-1114

Cobben JM, de Visser M (2002) SMN2 deletion in childhood-onset spinal muscular atrophy. Am J Med Genet 109 (3):246; discussion 247

Cobben JM, van der Steege G, Grootscholten P, de Visser M, Scheffer H, Buys CH (1995) Deletions of the survival motor neuron gene in unaffected siblings of patients with spinal muscular atrophy. Am J Hum Genet 57 (4):805-808

Compton SJ, Jones CG (1985) Mechanism of dye response and interference in the Bradford protein assay. Anal Biochem 151 (2):369-374

Coovert DD, Le TT, McAndrew PE, Strasswimmer J, Crawford TO, Mendell JR, Coulson SE, Androphy EJ, Prior TW, Burghes AH (1997) The survival motor neuron protein in spinal muscular atrophy. Hum Mol Genet 6 (8):1205-1214

Corti S, Nizzardo M, Nardini M, Donadoni C, Salani S, Ronchi D, Simone C, Falcone M, Papadimitriou D, Locatelli F, Mezzina N, Gianni F, Bresolin N, Comi GP (2010) Embryonic stem cell-derived neural stem cells improve spinal muscular atrophy phenotype in mice. Brain 133 (Pt 2):465-481. doi:10.1093/brain/awp318

De Sanctis R, Coratti G, Pasternak A, Montes J, Pane M, Mazzone ES, Young SD, Salazar R, Quigley J, Pera MC, Antonaci L, Lapenta L, Glanzman AM, Tiziano D, Muntoni F, Darras BT, De Vivo DC, Finkel R, Mercuri E (2016) Developmental milestones in type I spinal muscular atrophy. Neuromuscul Disord. doi:10.1016/j.nmd.2016.10.002

Deak F, Xu Y, Chang WP, Dulubova I, Khvotchev M, Liu X, Sudhof TC, Rizo J (2009) Munc18-1 binding to the neuronal SNARE complex controls synaptic vesicle priming. J Cell Biol 184 (5):751-764. doi:10.1083/jcb.200812026

Deimling von F, Scharf JM, Liehr T, Rothe M, Kelter AR, Albers P, Dietrich WF, Kunkel LM, Wernert N, Wirth B (1999) Human and mouse RAD17 genes: identification, localization, genomic structure and histological expression pattern in normal testis and seminoma. Hum Genet 105 (1-2):17-27

Delanote V, Vandekerckhove J, Gettemans J (2005) Plastins: versatile modulators of actin organization in (patho)physiological cellular processes. Acta Pharmacol Sin 26 (7):769-779

Dent EW, Gertler FB (2003) Cytoskeletal dynamics and transport in growth cone motility and axon guidance. Neuron 40 (2):209-227

Dickson A, Osman E, Lorson C (2008) A Negatively-Acting Bifunctional RNA Increases Survival Motor Neuron in vitro and in vivo. Hum Gene Ther

DiDonato CJ, Brun T, Simard LR (1999) Complete nucleotide sequence, genomic organization, and promoter analysis of the murine survival motor neuron gene (Smn). Mamm Genome 10 (6):638-641

DiDonato CJ, Chen XN, Noya D, Korenberg JR, Nadeau JH, Simard LR (1997) Cloning, characterization, and copy number of the murine survival motor neuron gene: homolog of the spinal muscular atrophy-determining gene. Genome Res 7 (4):339-352

DiDonato CJ, Lorson CL, De Repentigny Y, Simard L, Chartrand C, Androphy EJ, Kothary R (2001) Regulation of murine survival motor neuron (Smn) protein levels by modifying Smn exon 7 splicing. Hum Mol Genet 10 (23):2727-2736

Dimitriadi M, Sleigh JN, Walker A, Chang HC, Sen A, Kalloo G, Harris J, Barsby T, Walsh MB, Satterlee JS, Li C, Van Vactor D, Artavanis-Tsakonas S, Hart AC (2010) Conserved genes act as modifiers of invertebrate SMN loss of function defects. PLoS Genet 6 (10):e1001172

Doherty GJ, McMahon HT (2009) Mechanisms of endocytosis. Annu Rev Biochem 78:857-902. doi:10.1146/annurev.biochem.78.081307.110540

Dombert B, Sivadasan R, Simon CM, Jablonka S, Sendtner M (2014) Presynaptic localization of Smn and hnRNP R in axon terminals of embryonic and postnatal mouse motoneurons. PLoS One 9 (10):e110846. doi:10.1371/journal.pone.0110846

Dominguez E, Marais T, Chatauret N, Benkhelifa-Ziyyat S, Duque S, Ravassard P, Carcenac R, Astord S, Pereira de Moura A, Voit T, Barkats M (2011) Intravenous scAAV9 delivery of a codon-optimized SMN1 sequence rescues SMA mice. Hum Mol Genet 20 (4):681-693

Ebert AD, Yu J, Rose FF, Jr., Mattis VB, Lorson CL, Thomson JA, Svendsen CN (2009) Induced pluripotent stem cells from a spinal muscular atrophy patient. Nature 457 (7227):277-280

El-Khodor BF, Edgar N, Chen A, Winberg ML, Joyce C, Brunner D, Suarez-Farinas M, Heyes MP (2008) Identification of a battery of tests for drug candidate evaluation in the SMNDelta7 neonate model of spinal muscular atrophy. Exp Neurol 212 (1):29-43

Emery AE (1991) Population frequencies of inherited neuromuscular diseases--a world survey. Neuromuscul Disord 1 (1):19-29

Engqvist-Goldstein AE, Drubin DG (2003) Actin assembly and endocytosis: from yeast to mammals. Annu Rev Cell Dev Biol 19:287-332. doi:10.1146/annurev.cellbio.19.111401.093127

Fallini C, Donlin-Asp PG, Rouanet JP, Bassell GJ, Rossoll W (2016) Deficiency of the Survival of Motor Neuron Protein Impairs mRNA Localization and Local Translation in the Growth Cone of Motor Neurons. J Neurosci 36 (13):3811-3820. doi:10.1523/JNEUROSCI.2396-15.2016

Fan L, Simard LR (2002) Survival motor neuron (SMN) protein: role in neurite outgrowth and neuromuscular maturation during neuronal differentiation and development. Hum Mol Genet 11 (14):1605-1614

Fayzullina S, Martin LJ (2016) DNA Damage Response and DNA Repair in Skeletal Myocytes From a Mouse Model of Spinal Muscular Atrophy. J Neuropathol Exp Neurol 75 (9):889-902. doi:10.1093/jnen/nlw064

Feldkotter M, Schwarzer V, Wirth R, Wienker TF, Wirth B (2002) Quantitative analyses of SMN1 and SMN2 based on real-time lightCycler PCR: fast and highly reliable carrier testing and prediction of severity of spinal muscular atrophy. Am J Hum Genet 70 (2):358-368

Feng Z, Ling KK, Zhao X, Zhou C, Karp G, Welch EM, Naryshkin N, Ratni H, Chen KS, Metzger F, Paushkin S, Weetall M, Ko CP (2016) Pharmacologically induced mouse model of adult spinal muscular atrophy to evaluate effectiveness of therapeutics after disease onset. Hum Mol Genet 25 (5):964-975. doi:10.1093/hmg/ddv629

Foust KD, Wang X, McGovern VL, Braun L, Bevan AK, Haidet AM, Le TT, Morales PR, Rich MM, Burghes AH, Kaspar BK (2010) Rescue of the spinal muscular atrophy phenotype in a mouse model by early postnatal delivery of SMN. Nat Biotechnol 28 (3):271-274

Francesca G, Cinzia P, Antonella B, Stefano FV, Teresa CM, Tiziano I, Annalisa O, Martine AT, Nicoletta C, Nadia C, Lucia M, Claudio P, Grazia DC (2016) SMN affects membrane remodelling and anchoring of the protein synthesis machinery. J Cell Sci. doi:10.1242/jcs.176750

Gabanella F, Butchbach ME, Saieva L, Carissimi C, Burghes AH, Pellizzoni L (2007) Ribonucleoprotein assembly defects correlate with spinal muscular atrophy severity and preferentially affect a subset of spliceosomal snRNPs. PLoS One 2 (9):e921. doi:10.1371/journal.pone.0000921

Gabanella F, Pisani C, Borreca A, Farioli-Vecchioli S, Ciotti MT, Ingegnere T, Onori A, Ammassari-Teule M, Corbi N, Canu N, Monaco L, Passananti C, Di Certo MG (2016) SMN affects membrane remodelling and anchoring of the protein synthesis machinery. J Cell Sci 129 (4):804-816. doi:10.1242/jcs.176750

Galkin VE, Orlova A, Cherepanova O, Lebart MC, Egelman EH (2008) High-resolution cryo-EM structure of the F-actin-fimbrin/plastin ABD2 complex. Proc Natl Acad Sci U S A 105 (5):1494-1498. doi:10.1073/pnas.0708667105

Garbes L, Riessland M, Holker I, Heller R, Hauke J, Trankle C, Coras R, Blumcke I, Hahnen E, Wirth B (2009) LBH589 induces up to 10-fold SMN protein levels by several independent mechanisms and is effective even in cells from SMA patients non-responsive to valproate. Hum Mol Genet 18 (19):3645-3658

Gavrilina TO, McGovern VL, Workman E, Crawford TO, Gogliotti RG, DiDonato CJ, Monani UR, Morris GE, Burghes AH (2008) Neuronal SMN expression corrects spinal muscular atrophy in severe SMA mice while muscle-specific SMN expression has no phenotypic effect. Hum Mol Genet 17 (8):1063-1075

Geary RS, Wancewicz E, Matson J, Pearce M, Siwkowski A, Swayze E, Bennett F (2009) Effect of dose and plasma concentration on liver uptake and pharmacologic activity of a 2'-methoxyethyl modified chimeric antisense oligonucleotide targeting PTEN. Biochem Pharmacol 78 (3):284-291. doi:10.1016/j.bcp.2009.04.013

Geary RS, Yu RZ, Watanabe T, Henry SP, Hardee GE, Chappell A, Matson J, Sasmor H, Cummins L, Levin AA (2003) Pharmacokinetics of a tumor necrosis factor-alpha phosphorothioate 2'-O-(2-methoxyethyl) modified antisense oligonucleotide: comparison across species. Drug Metab Dispos 31 (11):1419-1428. doi:10.1124/dmd.31.11.1419

Geiser M (2010) Update on Macrophage Clearance of Inhaled Micro- and Nanoparticles. J Aerosol Med Pulm D 23 (4):207-217. doi:10.1089/jamp.2009.0797

Giesemann T, Rathke-Hartlieb S, Rothkegel M, Bartsch JW, Buchmeier S, Jockusch BM, Jockusch H (1999) A role for polyproline motifs in the spinal muscular atrophy protein SMN. Profilins bind to and colocalize with smn in nuclear gems. J Biol Chem 274 (53):37908-37914

Grohmann K, Varon R, Stolz P, Schuelke M, Janetzki C, Bertini E, Bushby K, Muntoni F, Ouvrier R, Van Maldergem L, Goemans NM, Lochmuller H, Eichholz S, Adams C, Bosch F, Grattan-Smith P, Navarro C, Neitzel H, Polster T, Topaloglu H, Steglich C, Guenther UP, Zerres K, Rudnik-Schoneborn S, Hubner C (2003) Infantile spinal muscular atrophy with respiratory distress type 1 (SMARD1). Ann Neurol 54 (6):719-724. doi:10.1002/ana.10755

Gupta K, Martin R, Sharp R, Sarachan KL, Ninan NS, Van Duyne GD (2015) Oligomeric Properties of Survival Motor Neuron.Gemin2 Complexes. J Biol Chem 290 (33):20185-20199. doi:10.1074/jbc.M115.667279

Hahnen E, Forkert R, Marke C, Rudnik-Schoneborn S, Schonling J, Zerres K, Wirth B (1995) Molecular analysis of candidate genes on chromosome 5q13 in autosomal recessive spinal muscular atrophy: evidence of homozygous deletions of the SMN gene in unaffected individuals. Hum Mol Genet 4 (10):1927-1933

Hamilton G, Gillingwater TH (2013) Spinal muscular atrophy: going beyond the motor neuron. Trends Mol Med 19 (1):40-50

Hanein D, Volkmann N, Goldsmith S, Michon AM, Lehman W, Craig R, DeRosier D, Almo S, Matsudaira P (1998) An atomic model of fimbrin binding to F-actin and its implications for filament crosslinking and regulation. Nat Struct Biol 5 (9):787-792

Hao le T, Wolman M, Granato M, Beattie CE (2012) Survival motor neuron affects plastin 3 protein levels leading to motor defects. J Neurosci 32 (15):5074-5084

Hauke J, Riessland M, Lunke S, Eyupoglu IY, Blumcke I, El-Osta A, Wirth B, Hahnen E (2009) Survival motor neuron gene 2 silencing by DNA methylation correlates with spinal muscular atrophy disease severity and can be bypassed by histone deacetylase inhibition. Hum Mol Genet 18 (2):304-317

Hayhurst M, Wagner AK, Cerletti M, Wagers AJ, Rubin LL (2012) A cell-autonomous defect in skeletal muscle satellite cells expressing low levels of survival of motor neuron protein. Dev Biol 368 (2):323-334. doi:10.1016/j.ydbio.2012.05.037

Heesen L, Peitz M, Torres-Benito L, Holker I, Hupperich K, Dobrindt K, Jungverdorben J, Ritzenhofen S, Weykopf B, Eckert D, Hosseini-Barkooie SM, Storbeck M, Fusaki N, Lonigro R, Heller R, Kye MJ, Brustle O, Wirth B (2016) Plastin 3 is upregulated in iPSC-derived motoneurons from asymptomatic SMN1-deleted individuals. Cell Mol Life Sci 73 (10):2089-2104. doi:10.1007/s00018-015-2084-y

Heier CR, Satta R, Lutz C, DiDonato CJ (2010) Arrhythmia and cardiac defects are a feature of spinal muscular atrophy model mice. Hum Mol Genet 19 (20):3906-3918

Helmken C, Hofmann Y, Schoenen F, Oprea G, Raschke H, Rudnik-Schoneborn S, Zerres K, Wirth B (2003) Evidence for a modifying pathway in SMA discordant families: reduced SMN level decreases the amount of its interacting partners and Htra2-beta1. Hum Genet 114 (1):11-21

Helmken C, Wirth B (2000) Exclusion of Htra2-beta1, an up-regulator of full-length SMN2 transcript, as a modifying gene for spinal muscular atrophy. Hum Genet 107 (6):554-558

Hosseinibarkooie S, Peters M, Torres-Benito L, Rastetter RH, Hupperich K, Hoffmann A, Mendoza-Ferreira N, Kaczmarek A, Janzen E, Milbradt J, Lamkemeyer T, Rigo F, Bennett CF, Guschlbauer C, Buschges A, Hammerschmidt M, Riessland M, Kye MJ, Clemen CS, Wirth B (2016) The Power of Human Protective Modifiers: PLS3 and CORO1C Unravel Impaired Endocytosis in Spinal Muscular Atrophy and Rescue SMA Phenotype. Am J Hum Genet 99 (3):647-665. doi:10.1016/j.ajhg.2016.07.014

Hsieh-Li HM, Chang JG, Jong YJ, Wu MH, Wang NM, Tsai CH, Li H (2000) A mouse model for spinal muscular atrophy. Nat Genet 24 (1):66-70

Hua Y, Sahashi K, Hung G, Rigo F, Passini MA, Bennett CF, Krainer AR (2010) Antisense correction of SMN2 splicing in the CNS rescues necrosis in a type III SMA mouse model. Genes Dev 24 (15):1634-1644

Hua Y, Sahashi K, Rigo F, Hung G, Horev G, Bennett CF, Krainer AR (2011) Peripheral SMN restoration is essential for long-term rescue of a severe spinal muscular atrophy mouse model. Nature 478 (7367):123-126

Hua Y, Vickers TA, Baker BF, Bennett CF, Krainer AR (2007) Enhancement of SMN2 exon 7 inclusion by antisense oligonucleotides targeting the exon. PLoS Biol 5 (4):e73. doi:10.1371/journal.pbio.0050073

Hua Y, Vickers TA, Okunola HL, Bennett CF, Krainer AR (2008) Antisense masking of an hnRNP A1/A2 intronic splicing silencer corrects SMN2 splicing in transgenic mice. Am J Hum Genet 82 (4):834-848. doi:10.1016/j.ajhg.2008.01.014

Hua Y, Zhou J (2004a) Modulation of SMN nuclear foci and cytoplasmic localization by its C-terminus. Cell Mol Life Sci 61 (19-20):2658-2663

Hua Y, Zhou J (2004b) Rpp20 interacts with SMN and is re-distributed into SMN granules in response to stress. Biochem Biophys Res Commun 314 (1):268-276

Huotari J, Helenius A (2011) Endosome maturation. EMBO J 30 (17):3481-3500. doi:10.1038/emboj.2011.286

Jablonka S, Schrank B, Kralewski M, Rossoll W, Sendtner M (2000) Reduced survival motor neuron (Smn) gene dose in mice leads to motor neuron degeneration: an animal model for spinal muscular atrophy type III. Hum Mol Genet 9 (3):341-346

Kariya S, Park GH, Maeno-Hikichi Y, Leykekhman O, Lutz C, Arkovitz MS, Landmesser LT, Monani UR (2008) Reduced SMN protein impairs maturation of the neuromuscular junctions in mouse models of spinal muscular atrophy. Hum Mol Genet 17 (16):2552-2569

Kariya S, Re DB, Jacquier A, Nelson K, Przedborski S, Monani UR (2014) Mutant superoxide dismutase 1 (SOD1), a cause of amyotrophic lateral sclerosis, disrupts the recruitment of SMN, the spinal muscular atrophy protein to nuclear Cajal bodies. Hum Mol Genet 21 (15):3421-3434

Kashima T, Manley JL (2003) A negative element in SMN2 exon 7 inhibits splicing in spinal muscular atrophy. Nat Genet 34 (4):460-463

Kedersha N, Anderson P (2009) Regulation of translation by stress granules and processing bodies. Prog Mol Biol Transl Sci 90:155-185. doi:10.1016/S1877-1173(09)90004-7

Kedersha NL, Gupta M, Li W, Miller I, Anderson P (1999) RNA-binding proteins TIA-1 and TIAR link the phosphorylation of eIF-2 alpha to the assembly of mammalian stress granules. J Cell Biol 147 (7):1431-1442

Kelter AR, Herchenbach J, Wirth B (2000) The transcription factor-like nuclear regulator (TFNR) contains a novel 55-amino-acid motif repeated nine times and maps closely to SMN1. Genomics 70 (3):315-326

Kerr DA, Nery JP, Traystman RJ, Chau BN, Hardwick JM (2000) Survival motor neuron protein modulates neuron-specific apoptosis. Proc Natl Acad Sci U S A 97 (24):13312-13317

Koller E, Vincent TM, Chappell A, De S, Manoharan M, Bennett CF (2011) Mechanisms of single-stranded phosphorothioate modified antisense oligonucleotide accumulation in hepatocytes. Nucleic Acids Res 39 (11):4795-4807. doi:10.1093/nar/gkr089

Kong L, Wang X, Choe DW, Polley M, Burnett BG, Bosch-Marce M, Griffin JW, Rich MM, Sumner CJ (2009) Impaired synaptic vesicle release and immaturity of neuromuscular junctions in spinal muscular atrophy mice. J Neurosci 29 (3):842-851

Kononenko NL, Puchkov D, Classen GA, Walter AM, Pechstein A, Sawade L, Kaempf N, Trimbuch T, Lorenz D, Rosenmund C, Maritzen T, Haucke V (2014) Clathrin/AP-2 mediate synaptic vesicle reformation from endosome-like vacuoles but are not

essential for membrane retrieval at central synapses. Neuron 82 (5):981-988. doi:10.1016/j.neuron.2014.05.007

Kubler E, Riezman H (1993) Actin and fimbrin are required for the internalization step of endocytosis in yeast. Embo J 12 (7):2855-2862

Kugelberg E, Welander L (1956) Heredofamilial juvenile muscular atrophy simulating muscular dystrophy. AMA Arch Neurol Psychiatry 75 (5):500-509

Kunda P, Paglini G, Quiroga S, Kosik K, Caceres A (2001) Evidence for the involvement of Tiam1 in axon formation. J Neurosci 21 (7):2361-2372

Laemmli UK (1970). Nature 227:680-685

Le TT, McGovern VL, Alwine IE, Wang X, Massoni-Laporte A, Rich MM, Burghes AH (2011) Temporal requirement for high SMN expression in SMA mice. Hum Mol Genet 20 (18):3578-3591. doi:10.1093/hmg/ddr275

Le TT, Pham LT, Butchbach ME, Zhang HL, Monani UR, Coovert DD, Gavrilina TO, Xing L, Bassell GJ, Burghes AH (2005) SMNDelta7, the major product of the centromeric survival motor neuron (SMN2) gene, extends survival in mice with spinal muscular atrophy and associates with full-length SMN. Hum Mol Genet 14 (6):845-857

Lefebvre S, Burglen L, Reboullet S, Clermont O, Burlet P, Viollet L, Benichou B, Cruaud C, Millasseau P, Zeviani M, et al. (1995) Identification and characterization of a spinal muscular atrophy-determining gene. Cell 80 (1):155-165

Letourneau PC, Shattuck TA (1989) Distribution and possible interactions of actin-associated proteins and cell adhesion molecules of nerve growth cones. Development 105 (3):505-519

Li CH, Tam PKS (1998) An iterative algorithm for minimum cross entropy thresholding. Pattern Recogn Lett 19 (8):771-776. doi:Doi 10.1016/S0167-8655(98)00057-9

Lichtman JW, Colman H (2000) Synapse elimination and indelible memory. Neuron 25 (2):269-278

Lim SR, Hertel KJ (2001) Modulation of survival motor neuron pre-mRNA splicing by inhibition of alternative 3' splice site pairing. J Biol Chem 276 (48):45476-45483

Lin CS, Aebersold RH, Kent SB, Varma M, Leavitt J (1988) Molecular cloning and characterization of plastin, a human leukocyte protein expressed in transformed human fibroblasts. Mol Cell Biol 8 (11):4659-4668

Lin CS, Chen ZP, Park T, Ghosh K, Leavitt J (1993a) Characterization of the human L-plastin gene promoter in normal and neoplastic cells. J Biol Chem 268 (4):2793-2801

Lin CS, Park T, Chen ZP, Leavitt J (1993b) Human plastin genes. Comparative gene structure, chromosome location, and differential expression in normal and neoplastic cells. J Biol Chem 268 (4):2781-2792

Lin CS, Shen W, Chen ZP, Tu YH, Matsudaira P (1994) Identification of I-plastin, a human fimbrin isoform expressed in intestine and kidney. Mol Cell Biol 14 (4):2457-2467

Ling KK, Gibbs RM, Feng Z, Ko CP (2012) Severe neuromuscular denervation of clinically relevant muscles in a mouse model of spinal muscular atrophy. Hum Mol Genet 21 (1):185-195. doi:10.1093/hmg/ddr453

Liu Q, Dreyfuss G (1996) A novel nuclear structure containing the survival of motor neurons protein. Embo J 15 (14):3555-3565

Liu Q, Fischer U, Wang F, Dreyfuss G (1997) The spinal muscular atrophy disease gene product, SMN, and its associated protein SIP1 are in a complex with spliceosomal snRNP proteins. Cell 90 (6):1013-1021

Lorson CL, Androphy EJ (2000) An exonic enhancer is required for inclusion of an essential exon in the SMA-determining gene SMN. Hum Mol Genet 9 (2):259-265

Lorson CL, Hahnen E, Androphy EJ, Wirth B (1999) A single nucleotide in the SMN gene regulates splicing and is responsible for spinal muscular atrophy. Proc Natl Acad Sci U S A 96 (11):6307-6311

Lorson CL, Strasswimmer J, Yao JM, Baleja JD, Hahnen E, Wirth B, Le T, Burghes AH, Androphy EJ (1998) SMN oligomerization defect correlates with spinal muscular atrophy severity. Nat Genet 19 (1):63-66

Low LK, Cheng HJ (2006) Axon pruning: an essential step underlying the developmental plasticity of neuronal connections. Philos Trans R Soc Lond B Biol Sci 361 (1473):1531-1544. doi:10.1098/rstb.2006.1883

Lunn MR, Wang CH (2008) Spinal muscular atrophy. Lancet 371 (9630):2120-2133

Lyon AN, Pineda RH, Hao le T, Kudryashova E, Kudryashov DS, Beattie CE (2014) Calcium binding is essential for plastin 3 function in Smn-deficient motoneurons. Hum Mol Genet 23 (8):1990-2004

Lyon CE, Bohmann K, Sleeman J, Lamond AI (1997) Inhibition of protein dephosphorylation results in the accumulation of splicing snRNPs and coiled bodies within the nucleolus. Experimental Cell Research 230 (1):84-93. doi:DOI 10.1006/excr.1996.3380

Markowitz JA, Tinkle MB, Fischbeck KH (2004) Spinal muscular atrophy in the neonate. J Obstet Gynecol Neonatal Nurs 33 (1):12-20

Matsudaira P (1994) The fimbrin and alpha-actinin footprint on actin. J Cell Biol 126 (2):285-287

McGovern VL, Massoni-Laporte A, Wang XY, Le TT, Le HT, Beattie CE, Rich MM, Burghes AHM (2015) Plastin 3 Expression Does Not Modify Spinal Muscular Atrophy Severity in the Delta 7 SMA Mouse. Plos One 10 (7). doi:ARTN e0132364

10.1371/journal.pone.0132364

McWhorter ML, Monani UR, Burghes AH, Beattie CE (2003) Knockdown of the survival motor neuron (Smn) protein in zebrafish causes defects in motor axon outgrowth and pathfinding. J Cell Biol 162 (5):919-931

Meister G, Fischer U (2002) Assisted RNP assembly: SMN and PRMT5 complexes cooperate in the formation of spliceosomal UsnRNPs. Embo J 21 (21):5853-5863

Melki J, Abdelhak S, Sheth P, Bachelot MF, Burlet P, Marcadet A, Aicardi J, Barois A, Carriere JP, Fardeau M, et al. (1990) Gene for chronic proximal spinal muscular atrophies maps to chromosome 5q. Nature 344 (6268):767-768

Mentis GZ, Blivis D, Liu W, Drobac E, Crowder ME, Kong L, Alvarez FJ, Sumner CJ, O'Donovan MJ (2011) Early functional impairment of sensory-motor connectivity in a mouse model of spinal muscular atrophy. Neuron 69 (3):453-467

Michaud M, Arnoux T, Bielli S, Durand E, Rotrou Y, Jablonka S, Robert F, Giraudon-Paoli M, Riessland M, Mattei MG, Andriambeloson E, Wirth B, Sendtner M, Gallego J, Pruss RM, Bordet T (2010) Neuromuscular defects and breathing disorders in a new mouse model of spinal muscular atrophy. Neurobiol Dis 38 (1):125-135

Miguel-Aliaga I, Culetto E, Walker DS, Baylis HA, Sattelle DB, Davies KE (1999) The Caenorhabditis elegans orthologue of the human gene responsible for spinal muscular atrophy is a maternal product critical for germline maturation and embryonic viability. Hum Mol Genet 8 (12):2133-2143

Monani UR, Coovert DD, Burghes AH (2000a) Animal models of spinal muscular atrophy. Hum Mol Genet 9 (16):2451-2457

Monani UR, De Vivo DC (2014) Neurodegeneration in spinal muscular atrophy: from disease phenotype and animal models to therapeutic strategies and beyond. Future Neurol 9 (1):49-65

Monani UR, Pastore MT, Gavrilina TO, Jablonka S, Le TT, Andreassi C, DiCocco JM, Lorson C, Androphy EJ, Sendtner M, Podell M, Burghes AH (2003) A transgene carrying an A2G missense mutation in the SMN gene modulates phenotypic severity in mice with severe (type I) spinal muscular atrophy. J Cell Biol 160 (1):41-52

Monani UR, Sendtner M, Coovert DD, Parsons DW, Andreassi C, Le TT, Jablonka S, Schrank B, Rossol W, Prior TW, Morris GE, Burghes AH (2000b) The human

centromeric survival motor neuron gene (SMN2) rescues embryonic lethality in Smn(-/-) mice and results in a mouse with spinal muscular atrophy. Hum Mol Genet 9 (3):333-339

Montes J, Gordon AM, Pandya S, De Vivo DC, Kaufmann P (2009) Clinical outcome measures in spinal muscular atrophy. J Child Neurol 24 (8):968-978. doi:10.1177/0883073809332702

Mooren OL, Galletta BJ, Cooper JA (2012) Roles for actin assembly in endocytosis. Annu Rev Biochem 81:661-686. doi:10.1146/annurev-biochem-060910-094416

Mullis KB FF, Scharf SJ, Saiki RK, Horn GT, Ehrlich HA (1986) Specific enzymatic amplification of DNA in vitro: the polymerase chain reaction. Cold Spring Harbor Symposium, Quant Biol (51):263-273

Munsat TL, Davies KE (1992) International SMA consortium meeting. (26-28 June 1992, Bonn, Germany). Neuromuscul Disord 2 (5-6):423-428

Murray LM, Comley LH, Thomson D, Parkinson N, Talbot K, Gillingwater TH (2008) Selective vulnerability of motor neurons and dissociation of pre- and post-synaptic pathology at the neuromuscular junction in mouse models of spinal muscular atrophy. Hum Mol Genet 17 (7):949-962

Mutsaers CA, Wishart TM, Lamont DJ, Riessland M, Schreml J, Comley LH, Murray LM, Parson SH, Lochmuller H, Wirth B, Talbot K, Gillingwater TH (2011) Reversible molecular pathology of skeletal muscle in spinal muscular atrophy. Hum Mol Genet 20 (22):4334-4344

Nover L, Scharf KD, Neumann D (1989) Cytoplasmic heat shock granules are formed from precursor particles and are associated with a specific set of mRNAs. Mol Cell Biol 9 (3):1298-1308

Oh N, Park JH (2014) Endocytosis and exocytosis of nanoparticles in mammalian cells. Int J Nanomedicine 9 Suppl 1:51-63. doi:10.2147/IJN.S26592

Okamoto K, Narayanan R, Lee SH, Murata K, Hayashi Y (2007) The role of CaMKII as an F-actin-bundling protein crucial for maintenance of dendritic spine structure. Proc Natl Acad Sci U S A 104 (15):6418-6423. doi:10.1073/pnas.0701656104

Ollion J, Cochennec J, Loll F, Escude C, Boudier T (2013) TANGO: a generic tool for high-throughput 3D image analysis for studying nuclear organization. Bioinformatics 29 (14):1840-1841. doi:10.1093/bioinformatics/btt276

Oprea GE, Krober S, McWhorter ML, Rossoll W, Muller S, Krawczak M, Bassell GJ, Beattie CE, Wirth B (2008) Plastin 3 is a protective modifier of autosomal recessive spinal muscular atrophy. Science 320 (5875):524-527

Osborne M, Gomez D, Feng ZH, McEwen C, Beltran J, Cirillo K, El-Khodor B, Lin MY, Li Y, Knowlton WM, McKemy DD, Bogdanik L, Butts-Dehm K, Martens K, Davis C, Doty R, Wardwell K, Ghavami A, Kobayashi D, Ko CP, Ramboz S, Lutz C (2012) Characterization of behavioral and neuromuscular junction phenotypes in a novel allelic series of SMA mouse models. Human Molecular Genetics 21 (20):4431-4447. doi:10.1093/hmg/dds285

Otsu N (1979) Threshold Selection Method from Gray-Level Histograms. Ieee T Syst Man Cyb 9 (1):62-66

Pak CW, Flynn KC, Bamburg JR (2008) Actin-binding proteins take the reins in growth cones. Nat Rev Neurosci 9 (2):136-147. doi:10.1038/nrn2236

Park GH, Kariya S, Monani UR (2010) Spinal muscular atrophy: new and emerging insights from model mice. Curr Neurol Neurosci Rep 10 (2):108-117

Passini MA, Bu J, Richards AM, Kinnecom C, Sardi SP, Stanek LM, Hua Y, Rigo F, Matson J, Hung G, Kaye EM, Shihabuddin LS, Krainer AR, Bennett CF, Cheng SH (2011) Antisense oligonucleotides delivered to the mouse CNS ameliorate symptoms of severe spinal muscular atrophy. Sci Transl Med 3 (72):72ra18

Passini MA, Bu J, Roskelley EM, Richards AM, Sardi SP, O'Riordan CR, Klinger KW, Shihabuddin LS, Cheng SH (2010) CNS-targeted gene therapy improves survival and motor function in a mouse model of spinal muscular atrophy. J Clin Invest 120 (4):1253-1264

Paushkin S, Charroux B, Abel L, Perkinson RA, Pellizzoni L, Dreyfuss G (2000) The survival motor neuron protein of Schizosacharomyces pombe. Conservation of survival motor neuron interaction domains in divergent organisms. J Biol Chem 275 (31):23841-23846

Pearn J (1978) Incidence, prevalence, and gene frequency studies of chronic childhood spinal muscular atrophy. J Med Genet 15 (6):409-413

Pelkmans L, Kartenbeck J, Helenius A (2001) Caveolar endocytosis of simian virus 40 reveals a new two-step vesicular-transport pathway to the ER. Nat Cell Biol 3 (5):473-483. doi:10.1038/35074539

Pellizzoni L (2007) Chaperoning ribonucleoprotein biogenesis in health and disease. EMBO Rep 8 (4):340-345. doi:10.1038/sj.embor.7400941

Pellizzoni L, Charroux B, Dreyfuss G (1999) SMN mutants of spinal muscular atrophy patients are defective in binding to snRNP proteins. Proc Natl Acad Sci U S A 96 (20):11167-11172

Piazzon N, Rage F, Schlotter F, Moine H, Branlant C, Massenet S (2008) In vitro and in cellulo evidences for association of the survival of motor neuron complex with the fragile X mental retardation protein. J Biol Chem 283 (9):5598-5610

Pollard TD, Borisy GG (2003) Cellular motility driven by assembly and disassembly of actin filaments. Cell 112 (4):453-465

Porensky PN, Mitrpant C, McGovern VL, Bevan AK, Foust KD, Kaspar BK, Wilton SD, Burghes AH (2012) A single administration of morpholino antisense oligomer rescues spinal muscular atrophy in mouse. Hum Mol Genet 21 (7):1625-1638

Rajendra TK, Gonsalvez GB, Walker MP, Shpargel KB, Salz HK, Matera AG (2007) A Drosophila melanogaster model of spinal muscular atrophy reveals a function for SMN in striated muscle. J Cell Biol 176 (6):831-841

Ralser M, Albrecht M, Nonhoff U, Lengauer T, Lehrach H, Krobitsch S (2005a) An integrative approach to gain insights into the cellular function of human ataxin-2. J Mol Biol 346 (1):203-214. doi:10.1016/j.jmb.2004.11.024

Ralser M, Nonhoff U, Albrecht M, Lengauer T, Wanker EE, Lehrach H, Krobitsch S (2005b) Ataxin-2 and huntingtin interact with endophilin-A complexes to function in plastin-associated pathways. Hum Mol Genet 14 (19):2893-2909. doi:10.1093/hmg/ddi321

Riessland M, Ackermann B, Forster A, Jakubik M, Hauke J, Garbes L, Fritzsche I, Mende Y, Blumcke I, Hahnen E, Wirth B (2010) SAHA ameliorates the SMA phenotype in two mouse models for spinal muscular atrophy. Hum Mol Genet 19 (8):1492-1506

Riessland M, Brichta L, Hahnen E, Wirth B (2006) The benzamide M344, a novel histone deacetylase inhibitor, significantly increases SMN2 RNA/protein levels in spinal muscular atrophy cells. Hum Genet 120 (1):101-110

Rigo F, Hua Y, Krainer AR, Bennett CF (2012) Antisense-based therapy for the treatment of spinal muscular atrophy. J Cell Biol 199 (1):21-25. doi:10.1083/jcb.201207087

Rochette CF, Gilbert N, Simard LR (2001) SMN gene duplication and the emergence of the SMN2 gene occurred in distinct hominids: SMN2 is unique to Homo sapiens. Hum Genet 108 (3):255-266

Rosenthal JL, Taraskevich PS (1977) Reduction of multiaxonal innervation at the neuromuscular junction of the rat during development. J Physiol 270 (2):299-310

Rossoll W, Jablonka S, Andreassi C, Kroning AK, Karle K, Monani UR, Sendtner M (2003) Smn, the spinal muscular atrophy-determining gene product, modulates axon growth

and localization of beta-actin mRNA in growth cones of motoneurons. J Cell Biol 163 (4):801-812. doi:10.1083/jcb.200304128

Rudnik-Schoneborn S, Berg C, Zerres K, Betzler C, Grimm T, Eggermann T, Eggermann K, Wirth R, Wirth B, Heller R (2009) Genotype-phenotype studies in infantile spinal muscular atrophy (SMA) type I in Germany: implications for clinical trials and genetic counselling. Clin Genet 76 (2):168-178

Rudnik-Schöneborn S, Rohrig D, Morgan G, Wirth B, Zerres K (1994) Autosomal recessive proximal spinal muscular atrophy in 101 sibs out of 48 families: clinical picture, influence of gender, and genetic implications. Am J Med Genet 51 (1):70-76

Ruiz R, Casanas JJ, Torres-Benito L, Cano R, Tabares L (2010) Altered intracellular Ca2+ homeostasis in nerve terminals of severe spinal muscular atrophy mice. J Neurosci 30 (3):849-857

Russman BS (2007) Spinal muscular atrophy: clinical classification and disease heterogeneity. J Child Neurol 22 (8):946-951

Sanes JR, Lichtman JW (1999) Development of the vertebrate neuromuscular junction. Annu Rev Neurosci 22:389-442. doi:10.1146/annurev.neuro.22.1.389

Schmidt H, Rathjen FG (2010) Signalling mechanisms regulating axonal branching in vivo. BioEssays : news and reviews in molecular, cellular and developmental biology 32 (11):977-985. doi:10.1002/bies.201000054

Schmutz J, Martin J, Terry A, Couronne O, Grimwood J, Lowry S, Gordon LA, Scott D, Xie G, Huang W, Hellsten U, Tran-Gyamfi M, She X, Prabhakar S, Aerts A, Altherr M, Bajorek E, Black S, Branscomb E, Caoile C, Challacombe JF, Chan YM, Denys M, Detter JC, Escobar J, Flowers D, Fotopulos D, Glavina T, Gomez M, Gonzales E, Goodstein D, Grigoriev I, Groza M, Hammon N, Hawkins T, Haydu L, Israni S, Jett J, Kadner K, Kimball H, Kobayashi A, Lopez F, Lou Y, Martinez D, Medina C, Morgan J, Nandkeshwar R, Noonan JP, Pitluck S, Pollard M, Predki P, Priest J, Ramirez L, Retterer J, Rodriguez A, Rogers S, Salamov A, Salazar A, Thayer N, Tice H, Tsai M, Ustaszewska A, Vo N, Wheeler J, Wu K, Yang J, Dickson M, Cheng JF, Eichler EE, Olsen A, Pennacchio LA, Rokhsar DS, Richardson P, Lucas SM, Myers RM, Rubin EM (2004) The DNA sequence and comparative analysis of human chromosome 5. Nature 431 (7006):268-274

Schrank B, Gotz R, Gunnersen JM, Ure JM, Toyka KV, Smith AG, Sendtner M (1997) Inactivation of the survival motor neuron gene, a candidate gene for human spinal muscular atrophy, leads to massive cell death in early mouse embryos. Proc Natl Acad Sci U S A 94 (18):9920-9925

Schreml J, Riessland M, Paterno M, Garbes L, Rossbach K, Ackermann B, Kramer J, Somers E, Parson SH, Heller R, Berkessel A, Sterner-Kock A, Wirth B (2013) Severe SMA mice show organ impairment that cannot be rescued by therapy with the HDACi JNJ-26481585. Eur J Hum Genet 21 (6):643-652

Schul W, van Driel R, de Jong L (1998) Coiled bodies and U2 snRNA genes adjacent to coiled bodies are enriched in factors required for snRNA transcription. Molecular Biology of the Cell 9 (5):1025-1036

See K, Yadav P, Giegerich M, Cheong PS, Graf M, Vyas H, Lee SG, Mathavan S, Fischer U, Sendtner M, Winkler C (2014) SMN deficiency alters Nrxn2 expression and splicing in zebrafish and mouse models of spinal muscular atrophy. Hum Mol Genet 23 (7):1754-1770. doi:10.1093/hmg/ddt567

Selenko P, Sprangers R, Stier G, Buhler D, Fischer U, Sattler M (2001) SMN tudor domain structure and its interaction with the Sm proteins. Nat Struct Biol 8 (1):27-31

Setola V, Terao M, Locatelli D, Bassanini S, Garattini E, Battaglia G (2007) Axonal-SMN (a-SMN), a protein isoform of the survival motor neuron gene, is specifically involved in axonogenesis. Proc Natl Acad Sci U S A 104 (6):1959-1964

Shababi M, Habibi J, Ma L, Glascock JJ, Sowers JR, Lorson CL (2012) Partial restoration of cardio-vascular defects in a rescued severe model of spinal muscular atrophy. J Mol Cell Cardiol 52 (5):1074-1082. doi:10.1016/j.yjmcc.2012.01.005

Shababi M, Habibi J, Yang HT, Vale SM, Sewell WA, Lorson CL (2010) Cardiac defects contribute to the pathology of spinal muscular atrophy models. Hum Mol Genet 19 (20):4059-4071

Shababi M, Lorson CL, Rudnik-Schoneborn SS (2014) Spinal muscular atrophy: a motor neuron disorder or a multi-organ disease? J Anat 224 (1):15-28. doi:10.1111/joa.12083

Shafey D, Cote PD, Kothary R (2005) Hypomorphic Smn knockdown C2C12 myoblasts reveal intrinsic defects in myoblast fusion and myotube morphology. Exp Cell Res 311 (1):49-61. doi:10.1016/j.yexcr.2005.08.019

Singh NK, Singh NN, Androphy EJ, Singh RN (2006) Splicing of a critical exon of human survival motor neuron is regulated by a unique silencer element located in the last intron. Mol Cell Biol 26 (4):1333-1346

Sleigh JN, Gillingwater TH, Talbot K (2011) The contribution of mouse models to understanding the pathogenesis of spinal muscular atrophy. Dis Model Mech 4 (4):457-467

Smythe E, Ayscough KR (2006) Actin regulation in endocytosis. J Cell Sci 119 (Pt 22):4589-4598. doi:10.1242/jcs.03247

Sumner CJ, Huynh TN, Markowitz JA, Perhac JS, Hill B, Coovert DD, Schussler K, Chen X, Jarecki J, Burghes AH, Taylor JP, Fischbeck KH (2003) Valproic acid increases SMN levels in spinal muscular atrophy patient cells. Ann Neurol 54 (5):647-654

Sun Y, Grimmler M, Schwarzer V, Schoenen F, Fischer U, Wirth B (2005) Molecular and functional analysis of intragenic SMN1 mutations in patients with spinal muscular atrophy. Hum Mutat 25 (1):64-71

Takata RI, Speck Martins CE, Passosbueno MR, Abe KT, Nishimura AL, Da Silva MD, Monteiro A, Jr., Lima MI, Kok F, Zatz M (2004) A new locus for recessive distal spinal muscular atrophy at Xq13.1-q21. J Med Genet 41 (3):224-229

Talbot K (1999) Spinal muscular atrophy. J Inherit Metab Dis 22 (4):545-554

Torres-Benito L, Neher MF, Cano R, Ruiz R, Tabares L (2011) SMN requirement for synaptic vesicle, active zone and microtubule postnatal organization in motor nerve terminals. PLoS One 6 (10):e26164. doi:10.1371/journal.pone.0026164

Torres-Benito L, Ruiz R, Tabares L (2012) Synaptic defects in SMA animal models. Dev Neurobiol

Towbin H, Staehelin T, Gordon J (1979) Electrophoretic transfer of proteins from polyacrylamide gels to nitrocellulose sheets: procedure and some applications. Proc Natl Acad Sci U S A 76 (9):4350-4354

Tsai LK, Tsai MS, Ting CH, Li H (2008) Multiple therapeutic effects of valproic acid in spinal muscular atrophy model mice. J Mol Med (Berl) 86 (11):1243-1254

Valori CF, Ning K, Wyles M, Mead RJ, Grierson AJ, Shaw PJ, Azzouz M (2010) Systemic delivery of scAAV9 expressing SMN prolongs survival in a model of spinal muscular atrophy. Sci Transl Med 2 (35):35ra42

van Bergeijk J, Rydel-Konecke K, Grothe C, Claus P (2007) The spinal muscular atrophy gene product regulates neurite outgrowth: importance of the C terminus. Faseb J 21 (7):1492-1502

Vanderhaeghen P, Cheng HJ (2010) Guidance molecules in axon pruning and cell death. Cold Spring Harb Perspect Biol 2 (6):a001859. doi:10.1101/cshperspect.a001859

Viollet L, Bertrandy S, Bueno Brunialti AL, Lefebvre S, Burlet P, Clermont O, Cruaud C, Guenet JL, Munnich A, Melki J (1997) cDNA isolation, expression, and chromosomal

localization of the mouse survival motor neuron gene (Smn). Genomics 40 (1):185-188

Vitte JM, Davoult B, Roblot N, Mayer M, Joshi V, Courageot S, Tronche F, Vadrot J, Moreau MH, Kemeny F, Melki J (2004) Deletion of murine Smn exon 7 directed to liver leads to severe defect of liver development associated with iron overload. Am J Pathol 165 (5):1731-1741

Walker MP, Rajendra TK, Saieva L, Fuentes JL, Pellizzoni L, Matera AG (2008) SMN complex localizes to the sarcomeric Z-disc and is a proteolytic target of calpain. Hum Mol Genet 17 (21):3399-3410

Wang CH, Finkel RS, Bertini ES, Schroth M, Simonds A, Wong B, Aloysius A, Morrison L, Main M, Crawford TO, Trela A (2007) Consensus statement for standard of care in spinal muscular atrophy. J Child Neurol 22 (8):1027-1049

Wang CH, Xu J, Carter TA, Ross BM, Dominski MK, Bellcross CA, Penchaszadeh GK, Munsat TL, Gilliam TC (1996) Characterization of survival motor neuron (SMNT) gene deletions in asymptomatic carriers of spinal muscular atrophy. Hum Mol Genet 5 (3):359-365

Wang ZJ, Tiruppathi C, Minshall RD, Malik AB (2009) Size and Dynamics of Caveolae Studied Using Nanoparticles in Living Endothelial Cells. Acs Nano 3 (12):4110-4116. doi:10.1021/nn9012274

Watanabe S, Rost BR, Camacho-Perez M, Davis MW, Sohl-Kielczynski B, Rosenmund C, Jorgensen EM (2013) Ultrafast endocytosis at mouse hippocampal synapses. Nature 504 (7479):242-247. doi:10.1038/nature12809

Werdnig G (1891) Zwei frühinfantile hereditäre Fälle von progressiver Muskelatrophie unter dem Bilde der Dystrophie, aber auf neurotischer Grundlage. Archiv für Psychiatrie und Nervenkrankheiten 22:437-480

Williams JH, Schray RC, Patterson CA, Ayitey SO, Tallent MK, Lutz GJ (2009) Oligonucleotide-mediated survival of motor neuron protein expression in CNS improves phenotype in a mouse model of spinal muscular atrophy. J Neurosci 29 (24):7633-7638

Wirth B, Barkats M, Martinat C, Sendtner M, Gillingwater TH (2015) Moving towards treatments for spinal muscular atrophy: hopes and limits. Expert opinion on emerging drugs 20 (3):353-356. doi:10.1517/14728214.2015.1041375

Wirth B, Brichta L, Hahnen E (2006) Spinal muscular atrophy: from gene to therapy. Semin Pediatr Neurol 13 (2):121-131. doi:10.1016/j.spen.2006.06.008

Wirth B, Garbes L, Riessland M (2013) How genetic modifiers influence the phenotype of spinal muscular atrophy and suggest future therapeutic approaches. Curr Opin Genet Dev 23 (3):330-338

Wyatt TJ, Keirstead HS (2010) Stem cell-derived neurotrophic support for the neuromuscular junction in spinal muscular atrophy. Expert Opin Biol Ther 10 (11):1587-1594

Ymlahi-Ouazzani Q, O JB, Paillard E, Ballagny C, Chesneau A, Jadaud A, Mazabraud A, Pollet N (2010) Reduced levels of survival motor neuron protein leads to aberrant motoneuron growth in a Xenopus model of muscular atrophy. Neurogenetics 11 (1):27-40

Young KD (2006) The selective value of bacterial shape. Microbiology and molecular biology reviews : MMBR 70 (3):660-703. doi:10.1128/MMBR.00001-06

Young PJ, Le TT, Dunckley M, Nguyen TM, Burghes AH, Morris GE (2001) Nuclear gems and Cajal (coiled) bodies in fetal tissues: nucleolar distribution of the spinal muscular atrophy protein, SMN. Exp Cell Res 265 (2):252-261

Young PJ, Le TT, thi Man N, Burghes AH, Morris GE (2000) The relationship between SMN, the spinal muscular atrophy protein, and nuclear coiled bodies in differentiated tissues and cultured cells. Exp Cell Res 256 (2):365-374

Zerres K, Rudnik-Schoneborn S (1995) Natural history in proximal spinal muscular atrophy. Clinical analysis of 445 patients and suggestions for a modification of existing classifications. Arch Neurol 52 (5):518-523

Zhang H, Xing L, Rossoll W, Wichterle H, Singer RH, Bassell GJ (2006) Multiprotein complexes of the survival of motor neuron protein SMN with Gemins traffic to neuronal processes and growth cones of motor neurons. J Neurosci 26 (33):8622-8632

Zhang HL, Pan F, Hong D, Shenoy SM, Singer RH, Bassell GJ (2003) Active transport of the survival motor neuron protein and the role of exon-7 in cytoplasmic localization. J Neurosci 23 (16):6627-6637

Zhang Z, Lotti F, Dittmar K, Younis I, Wan L, Kasim M, Dreyfuss G (2008) SMN deficiency causes tissue-specific perturbations in the repertoire of snRNAs and widespread defects in splicing. Cell 133 (4):585-600

Zhou H, Meng J, Marrosu E, Janghra N, Morgan J, Muntoni F (2015) Repeated low doses of morpholino antisense oligomer: an intermediate mouse model of spinal muscular atrophy to explore the window of therapeutic response. Hum Mol Genet 24 (22):6265-6277. doi:10.1093/hmg/ddv329

11.   Appendix

```
1  /*
2   PZ, 20160420
3   Tested with Fiji/ImageJ 1.50g on Linux (Ubuntu14.04.1 x86_64 GNU/Linux 3.16.0-67-generic)
4
5  By this macro the soma of motoneurons and axonal terminals can be identified in 3d fluorescence micrographs.
6  */
7  //Config
8  //Specify channels
9  //Switches - set 1 for activation, 0 to disable
10 var skipExistingFiles=1; //set 1 to use preprocessed images from earlier runs
11 var pickCellsManually=1; //set 1 to select cells by clicking, automatic detection might take very long and does not always work properly
12 var MNautoThreshold=1; // only applies if pickCellsManually is set; set 1 to automatically determine watershed image threshold, from mean values of slices, which contain pi
13 //var adjust3DSegmentationManually=0; //0: do not adjust, set to 1 to always manually merge/spit/delete cells and inputs before statistics are calculated, set to 2 to only
14 var automaticInputSegmentation=1;//if switched of reasonable thresholds have to be provided below, otherwise "Li dark"-algorithm is applied to autodetermine the threshold v
15 var lowContrastOptimisedAutoThreshold=0; //only applicable when MNautoThreshold is active, set to 1 if contrast is poor (i.e. high BG and dim cell staining)
16
17 //Parameters
18 //for some parameter changes to take effect, switch skipExistingFiles may have to be set to 0
19 var MNChannel=2; //set soma channel in lsm-file
20 var InputChannel=1;//set axonal input channel in lsm-file
21 var inputFileformat=".czi";//(.lsm/.czi/.tif)
22
23 var watershedMNSeedThreshold=100;//important for autodetection of cells...
24
25 var watershedImgThreshold=70;//overwritten
26
27 var MNseedSize=10;//size of watershed seeds for manual and automatic watershed segmentation
28
29 var nrOfMNDilationCycles=5;//number of iterations of 3D dilation on watershed result (set to 0 if watershed perfectly finds the cells, increase if watershed segmentation ap
30 var inputAutoThreshold=1;
31 var inputManualThreshold=10;//threshold for segmentation of inputs, only applies if inputAutoThreshold=0
32 var inputVolumeMin=20;
33 var inputVolumeMax=-1;
34 var inputThreshold;//to save the autothreshold value
35 var neuronThresholdLow;//to save the autothreshold value
36 var neuronThresholdHigh;//to save the autothreshold value
37
38 var distanceThreshold=2;
39
40 var inputSpotSegmentationCommand=1;
41
42 //Global variables
43 var lsmFilelist=newArray(0);
44 var directory;
45 var parentfolder;
46 var parentfolderTop;
47 var ppfolder;
48 var segfolder;
49 var resultfolder;
50
51
52 var logFilename="Log_"+ random+".txt";
53 var origInputFilename="axonalInputs.tif";
54 var origNeuronFilename="motorneurons.tif";
55 var ppMN1Filename="motorneuronSmoothed.tif";
56 var ppInp1Filename="inputSmoothed.tif";
57 var segInp1Filename="inputSegmented.tif";
58 var segMN1Filename="motorneuronsSegmented.tif";
59 var result1Filename="_separateCellResult.tif";
60 var result2Filename="CellMeasurements.csv";
61 var result3Filename="CellMeasurementsResultSummary.csv";
62 var cellResultsArray=newArray();
63 //1:Img-Folderfilename
64 //2:CellNr
65 //3:CellVolume [um3]
66 //4:CellSurf [um2]
67 //5:# of inputs
68 //6: avg Volume of inputs [um3]
69
70 //7:cx
71 //8:cy
72 //9:cz
73 //10: inputThreshold
74 //11: neuron Lower Threshold
75 //12: neuron upper Threshold
76 var cRLineLength=12;
77
78 var calibratedVoxelWidth;
79 var calibratedVoxelUnit;
80 var voxelSizeFilelist;
81 //Main-Loop
82 //Recursively find all input-files from folder
83 print("\\Clear");
84 print("logFilename");
85 logDate();
86 directory=getDirectory("Choose input Directory");
87 print("Looking for "+ inputFileformat+"-files in "+directory);
88 lsmFilelist=listLsmFiles(directory,lsmFilelist);
89 //Generate resultfolders from lsmFilelist
90 parentfolderTop=newArray(lsmFilelist.length);//ImageX_results
91 parentfolder=newArray(lsmFilelist.length);//ImageX_results/ImageJ
92 ppfolder=newArray(lsmFilelist.length);
93 segfolder=newArray(lsmFilelist.length);
94 resultfolder=newArray(lsmFilelist.length);
95
96 inputThreshold=newArray(lsmFilelist.length);
97 neuronThresholdHigh=newArray(lsmFilelist.length);
98 neuronThresholdLow=newArray(lsmFilelist.length);
99
100
101 for(i=0;i<lsmFilelist.length;i++){
102     if(startsWith(getInfo("os.name"),"Win")){
```

```
103     lsmFilelist[i]=replace(lsmFilelist[i],"/",File.separator);
104     }
105     parentfolderTop[i]=replace(lsmFilelist[i],inputFileformat,"_results");
106
107     print("lsm: "+lsmFilelist[i]+" IFF: "+inputFileformat);
108     if(startsWith(getInfo("os.name"),"Win")){
109     print(parentfolderTop[i]);
110 //  parentfolderTop[i]=replace(parentfolder[i],"\\/",File.separator);
111     print(parentfolderTop[i]);
112     }
113     if(!File.exists(parentfolderTop[i])){
114     File.makeDirectory(parentfolderTop[i]);
115     }
116
117     parentfolder[i]=parentfolderTop[i]+File.separator+"ImageJ";
118     if(startsWith(getInfo("os.name"),"Win")){
119     parentfolder[i]=replace(parentfolder[i],"/",File.separator);
120     }
121     if(!File.exists(parentfolder[i])){
122     File.makeDirectory(parentfolder[i]);
123     }
124
125
126     ppfolder[i]=parentfolder[i]+File.separator+"prep";
127     if(!File.exists(ppfolder[i])){
128     File.makeDirectory(ppfolder[i]);
129     }
130     segfolder[i]=parentfolder[i]+File.separator+"seg";
131     if(!File.exists(segfolder[i])){
132     File.makeDirectory(segfolder[i]);
133     }
134
135     beginIndex=lastIndexOf(substring(parentfolder[i],0,lengthOf(parentfolder[i])-7), File.separator)+1;
136     endIndex=lastIndexOf(parentfolder[i], "_results");
137     basefilename=substring(parentfolder[i],beginIndex,endIndex);
138     basefolderFullpath=File.getParent(parentfolderTop[i]);
139     endIndex=lengthOf(basefolderFullpath);
140     startIndex=lastIndexOf(basefolderFullpath, File.separator)+1;
141     basedir=substring(parentfolder[i],startIndex,endIndex);
142     resdir="result_"+basedir+"-"+basefilename;
143     resultfolder[i]=parentfolder[i]+File.separator+resdir;
144     if(!File.exists(resultfolder[i])){
145     File.makeDirectory(resultfolder[i]);
146     }
147 }
148
149
150 saveLogs(directory);
151
152
153
```

```
154 //Split original files each channel in one spatially calibrated (resliced, so that voxel are isometric) tiff-stack
155 for(i=0;i<lsmFilelist.length;i++){
156     print(i+": split "+lsmFilelist[i]);
157     if(skipExistingFiles) {
158     if (File.exists(ppfolder[i]+File.separator+origInputFilename)&&File.exists(ppfolder[i]+File.separator+origNeuronFilename)) {
159         print(lsmFilelist[i]+"-split files already exist. Skip.");
160         continue;
161     }
162     }
163     open(lsmFilelist[i]);
164     openOrigImg=getImageID();
165     getVoxelSize(voxelWidth, voxelHeight, voxelDepth, voxelUnit);
166     calibratedVoxelWidth=voxelWidth;
167     calibratedVoxelUnit=voxelUnit;
168     //Split channels of original image
169     run("Duplicate...", "duplicate channels=MNChannel");
170     setVoxelSize(voxelWidth,voxelHeight,voxelDepth,voxelUnit);
171     eval("run(\"Reslice Z\", \"new="+voxelWidth+"\");");
172     save(ppfolder[i]+File.separator+origNeuronFilename);
173     openMNorigImg=getImageID();
174
175     selectImage(openOrigImg);
176     run("Duplicate...", "duplicate channels=InputChannel");
177     setVoxelSize(voxelWidth,voxelHeight,voxelDepth,voxelUnit);
178     eval("run(\"Reslice Z\", \"new="+voxelWidth+"\");");
179     save(ppfolder[i]+File.separator+origInputFilename);
180
181     closeAllOpenImages();
182 }
183 //saveLogs(directory);
184
185
186
187 //preprocess motorneuron images
188 for(i=0;i<lsmFilelist.length;i++){
189     processed=preprocessMotorneuronImg(i);
190     if(processed==0){
191     print("Warning: Preprocessing of "+"failed. This will most certainly cause problems in the further course of analysis...");
192     }
193     else{
194     print(i+": "+ppMN1Filename +" was created/existed.");
195     }
196     closeAllOpenImages();
197 }
198 saveLogs(directory);
199
200
201 //preprocess axonal input images
202 for(i=0;i<lsmFilelist.length;i++){
203     processed=preprocessInputImg(i);
204     if(processed==0){
```

```
205        print("Warning: Preprocessing of "+"failed. This will most certainly cause problems in the further course of analysis...");
206      }
207      else{
208      print(i+": "+ppInp1Filename +" was created/existed.");
209      }
210      closeAllOpenImages();
211  }
212
213  saveLogs(directory);
214  //segmentate axonal input
215  for(i=0;i<lsmFilelist.length;i++){
216      segmented=segmentInputImg(i);
217      if(segmented==0){
218      print("Warning: Segmentation of "+"failed. This will most certainly cause problems in the further course of analysis...");
219      }
220      else{
221      print(i+": "+segInp1Filename +" was created/existed.");
222      }
223      closeAllOpenImages();
224  }
225
226  saveLogs(directory);
227
228  //cell selection and segmentation
229
230  for(i=0;i<lsmFilelist.length;i++){
231      print("Cell segmentation - file:  "+i+" of "+lsmFilelist.length);
232      segmented=segmentMotorneurons(i);
233      if(segmented==0){
234      print("Warning: No cells were selected. This might cause problems in the further course of analysis...");
235      }
236      else{
237      print(i+": "+segMN1Filename +" was created/existed.");
238      }
239      closeAllOpenImages();
240  }
241
242  saveLogs(directory);
243
244  //ensure spatial calibration
245  voxelSizeFilelist=newArray(lsmFilelist.length);
246  for(i=0;i<lsmFilelist.length;i++){
247      calibrated=spatialCalibration(i);
248      closeAllOpenImages();
249      Array.show(voxelSizeFilelist);
250  }
251
252  //Review segmentation (optional)
253
254  if(getBoolean("Review/edit segmented cells?")){
255      for(i=0;i<lsmFilelist.length;i++){
```

```
255      for(i=0;i<lsmFilelist.length;i++){
256      print("Cell segmentation - file:  "+i+" of "+lsmFilelist.length);
257      reviewed=inspectCellSegmentation(i);
258      if(reviewed==1){
259      print("Image was edited...");
260      }
261      else{
262      print(i+": "+segMN1Filename +"no edits saved.");
263      }
264
265      }
266      closeAllOpenImages();
267  }
268
269  saveLogs(directory);
270  //Check for result files, prompt for deletion
271  deleteFlag=0;
272  for(i=0;i<lsmFilelist.length;i++){
273      trashFilelist=getFileList(resultfolder[i]);
274      if(trashFilelist.length>0){
275      for(j=0;j<trashFilelist.length;j++){
276          if(endsWith(trashFilelist[j],result1Filename)){
277          deleteFlag=1;
278          print(trashFilelist[j]);
279          File.delete(trashFilelist[j]);
280          }
281      }
282      }
283  }
284
285
286
287  //create single cell 3d-images
288  run("3D Manager");
289  for(i=0;i<lsmFilelist.length;i++){
290      Ext.Manager3D_Reset();
291      singleCellReconstruction=drawSeparateCells(i);
292      if(singleCellReconstruction==0){
293      print("Warning: Single cell reconstruction did not work out for dataset "+ lsmFilelist[i]".");
294      }
295      else{
296      print(i+": Cells succesfully separated.");
297      }
298      closeAllOpenImages();
299  }
300  Ext.Manager3D_Close();
301  saveLogs(directory);
302
303  //measure cells and assigned inputs from single cell images
304  run("3D Manager");
305
```

```
306
307
308 for(i=0;i<lsmFilelist.length;i++){
309     Ext.Manager3D_Reset();
310     measured=measureSeparatedCells(i);
311     if(measured==0){
312     print("Warning: Was not able to measure all cells from this image: "+ lsmFilelist[i]".");
313     }
314     else{
315     print(i+": Cells succesfully separated.");
316     }
317     closeAllOpenImages();
318 }
319 Ext.Manager3D_Close();
320
321 //compile summary of results from all cells
322 run("Clear Results");
323 compileResultsSummary();
324 saveAs("results", directory+File.separator+"CellMeasurementsResultSummary.csv");
325 print("All files processed. Exit...");
326 saveLogs(directory);
327 print("Done!");
328
329 exit();
330
331
332
333
334 //Functions
335
336 function saveLogs(directory){
337     logpath=directory;
338     selectWindow("Log");
339     if(File.exists(logpath+File.separator+logFilename)){
340     File.append(getInfo("log"),logpath+File.separator+logFilename);
341     }else{
342     saveAs("Text", logpath+logFilename);
343     }
344     print("\\Clear");
345 }
346
347
348
349   function listLsmFiles(dir,filelist) {
350
351     lsmList=filelist;
352     addFile=newArray(1);
353
354      list = getFileList(dir);
355
355
356       for (i=0; i<list.length; i++) {
357
358     if (endsWith(list[i],"/")){
359         lsmList=listLsmFiles(""+dir+list[i],lsmList);
360     }else{
361         if (endsWith(list[i], inputFileformat)) {
362         addFile=dir +list[i];
363         lsmList=Array.concat(lsmList,addFile);
364         }
365     }
366     }
367
368     return lsmList;
369   }
370 function logDate(){
371     getDateAndTime(y,m,dow,dom,hour,min,sec,ms);
372     print(hour+":"+min+":"+sec+" "+dom+"."+(m+1)+"."+y);
373     return;
374 }
375
376 function closeAllOpenImages(){
377     openImageList=getList("image.titles");
378     for(u=0;u<openImageList.length;u++){
379     selectWindow(openImageList[u]);
380     close;
381     }
382     openImageList=getList("image.titles");
383     if(openImageList.length>0){
384     for(u=0;u<openImageList.length;u++){
385         print("Warning: Not possible to close window"+openImageList[u]);
386     }
387     }
388     return;
389 }
390
391 function findImageIdAndTitle(titlepattern){
392     //returns array with window ID and title of an open window containing titlepattern in its title
393     windowTitleList=getList("image.titles");
394     // Array.show(windowTitleList);
395     for(w=0;w<windowTitleList.length;w++){
396     pattern=".*"+titlepattern+".*";
397     if(matches(windowTitleList[w],pattern)){
398         selectWindow(windowTitleList[w]);
399         id=getImageID();
400         windowIdAndTitle=newArray(id,windowTitleList[w]);
401         return windowIdAndTitle;
402     }
403     }
404     print("Warning: no window matching title "+titlepattern+" was found.");
405     return 0;
406 }
```

```
407
408  function spatialCalibration(i){
409      open(lsmFilelist[i]);
410      openOrigImg=getImageID();
411      getVoxelSize(voxelWidth, voxelHeight, voxelDepth, voxelUnit);
412      voxelSizeFilelist[i]=voxelWidth;
413      close;
414      return 1;
415  }
416
417  function preprocessMotorneuronImg(filelistIndex){
418      outputfolder=ppfolder[filelistIndex];
419      print(outputfolder);
420      inputFolderFilename=ppfolder[filelistIndex]+File.separator+origNeuronFilename;
421      outputFolderFilename=outputfolder+File.separator+ppMN1Filename;
422
423      if(skipExistingFiles) {
424      if(File.exists(outputFolderFilename)){
425          print("File "+outputFolderFilename+" already exists. Skip smoothing...");
426          return 1;
427      }
428      }
429
430      open(inputFolderFilename);
431      setMinAndMax(0, 255);
432      run("3D Fast Filters","filter=Median radius_x_pix=8.0 radius_y_pix=8.0 radius_z_pix=8.0 Nb_cpus=24");
433      setMinAndMax(0, 255);
434      save(outputFolderFilename);
435      return 1;
436  }
437
438
439
440  function preprocessInputImg(filelistIndex){
441      outputfolder=ppfolder[filelistIndex];
442      inputFolderFilename=ppfolder[filelistIndex]+File.separator+origInputFilename;
443      outputFolderFilename=outputfolder+File.separator+ppInp1Filename;
444      if(skipExistingFiles) {
445      if(File.exists(outputFolderFilename)){
446          print("File "+outputFolderFilename+" already exists. Skip smoothing...");
447          return 1;
448      }
449      }
450      open(inputFolderFilename);
451      setMinAndMax(0, 255);
452      run("3D Fast Filters","filter=Adaptive radius_x_pix=3.0 radius_y_pix=3.0 radius_z_pix=2.0 Nb_cpus=24");
453      openAdaptiveSmooth=getTitle();
454      run("Duplicate...", "duplicate");
455      if(automaticInputSegmentation){
456      setAutoThreshold("Li dark");


457      run("Convert to Mask", "method=Li background=Dark calculate");
458      }else{
459      setThreshold(inputManualThreshold,255);
460      run("Convert to Mask", "method=Default background=Dark");
461      }
462      openMask=getTitle();
463      run("Divide...", "value=255.000 stack");
464
465      imageCalculator("Multiply create stack", openAdaptiveSmooth,openMask);
466      setMinAndMax(0, 255);
467      save(outputFolderFilename);
468      return 1;
469  }
470
471  function segmentInputImg(filelistIndex){
472      outputfolder=segfolder[filelistIndex];
473      inputFolderFilename=ppfolder[filelistIndex]+File.separator+ppInp1Filename;
474      outputFolderFilename=outputfolder+File.separator+segInp1Filename;
475      if(skipExistingFiles) {
476      if(File.exists(outputFolderFilename)){
477          print("File "+outputFolderFilename+" already exists. Skip input segmentation...");
478          return 1;
479      }
480      }
481      open(inputFolderFilename);
482      inputImg=getImageID();
483      if(inputAutoThreshold==1){
484      setAutoThreshold("Otsu"+" dark show stack use_stack_histogram");
485      getThreshold(lower,upper);
486      inputThreshold[filelistIndex]=lower;
487      resetThreshold();
488      run("3D Simple Segmentation", "low_threshold="+lower+" min_size="+inputVolumeMin+" max_size=-1");
489
490      }else{
491      run("3D Simple Segmentation", "low_threshold="+inputManualThreshold+" min_size="+inputVolumeMin+" max_size="+inputVolumeMax);
492      inputThreshold[filelistIndex]=inputManualThreshold;
493      }
494
495
496      save(outputFolderFilename);
497      return 1;
498  }
499
500  function segmentMotorneurons(filelistIndex){
501      outputfolder=segfolder[filelistIndex];
502      inputFolderFilename=ppfolder[filelistIndex]+File.separator+ppMN1Filename;
503      outputFolderFilename=outputfolder+File.separator+segMN1Filename;
504      if(skipExistingFiles) {
505      if(File.exists(outputFolderFilename)){
506          print("File "+outputFolderFilename+" already exists. Skip cell selection...");
507          return 1;
```

```
508    }
509    }
510    open(inputFolderFilename);
511    mnSmoothImg=getImageID();
512    origWidth=getWidth();
513    origHeight=getHeight();
514    origSlices=nSlices;
515    run("Z Project...", "projection=[Sum Slices]");
516    xyImg=getImageID();
517    selectImage(xyImg);
518
519    run("ROI Manager...");
520    roiManager("Show All");
521    setTool("rectangle");
522    //load existing or prompt for deletion
523    if(File.exists(outputfolder+File.separator+"RoiSet.zip")){
524        reloadRoi=getBoolean("A roi set already exists. Would you like to reload it?");
525        if(reloadRoi){
526            roiManager("Open",outputfolder+File.separator+"RoiSet.zip");
527            //showMessage("If you would like to save any modifications or add rois, at first you have to delete the RoiSet.zip file otherwise your changes will not be saved!"
528        }else{
529            showMessage("Your rois will not be saved unless you delete the existing RoiSet.zip file before you proceed!");
530        }
531    }
532
533    waitForUser("Select all cells you would like to analyse. Press 't' to add a ROI. Click 'OK' when done with all cells.");
534    roiManager("Save", outputfolder+File.separator+"RoiSet.zip");
535    newImage("segSummaryImg", "8-bit black", origWidth, origHeight, origSlices);
536    segSummaryImg=getImageID();
537    nrOfRois=roiManager("count");
538    nrOfRoiValues=9;
539    //ROI-values: left, top, width, height, topSlice, nrOfSlices, mean, max, std
540    roiArray=newArray(nrOfRois*nrOfRoiValues);
541    for(j=0;j<nrOfRois;j++){
542        selectImage(mnSmoothImg);
543        roiManager("select", j);
544        roiName=Roi.getName;//for z-filename generation
545
546        getSelectionBounds(x, y, width, height);
547
548        roiArray[j*nrOfRoiValues+0]=x;
549        roiArray[j*nrOfRoiValues+1]=y;
550        roiArray[j*nrOfRoiValues+2]=width;
551        roiArray[j*nrOfRoiValues+3]=height;
552
553
554
555        run("Duplicate...", "duplicate");
556        croppedCellImg=getImageID();
557        run("Orthogonal Views");
558        XZwindow="XZ "+ floor(roiArray[j*nrOfRoiValues+3]/2);
559        print(XZwindow);
```

```
559        print(XZwindow);
560        wait(3500);
561        if(!isOpen(XZwindow)){
562            waitForUser("XZwindow of expected name "+XZwindow+"not found. Please open/select manually and then click OK!");
563            XZwindow=getTitle();
564        }
565        selectWindow(XZwindow);
566        run("Duplicate...", " ");
567        XZwindow=getImageID();
568        selectImage(croppedCellImg);
569        run("Orthogonal Views");
570        selectImage(croppedCellImg);
571        close();
572        selectImage(XZwindow);
573        run("Set... ", "zoom=200");
574        xOld=5;
575        widthOld=getWidth-5;
576
577        zPosFilename="ZPos-"+roiName+"=";
578
579        zlist = getFileList(outputfolder);
580        for (k=0; k<zlist.length; k++) {
581            if (startsWith(zlist[k],zPosFilename)){
582                //read position, draw selection, delete file
583                yStart=lastIndexOf(zlist[k],"=")+1;
584                yEnd=lastIndexOf(zlist[k],"_");
585                yOld=substring(zlist[k],yStart,yEnd);
586                heightStart=lastIndexOf(zlist[k],"_")+1;
587                heightEnd=lengthOf(zlist[k]);
588                heightOld=substring(zlist[k],heightStart,heightEnd);
589                makeRectangle(xOld,yOld,widthOld,heightOld);
590                File.delete(zlist[k]);
591            }
592        }
593        setTool("rectangle");
594        waitForUser("Confine cell in z-direction an press 'OK'.");
595        getSelectionBounds(x, y, width, height);
596
597        roiArray[j*nrOfRoiValues+4]=y;
598        roiArray[j*nrOfRoiValues+5]=height;
599        zPosFilename=zPosFilename+y+"_"+height;
600        File.saveString(zPosFilename,outputfolder+File.separator+zPosFilename);
601        close;
602        selectImage(mnSmoothImg);
603        roiManager("select", j);
604        run("Duplicate...", "duplicate range="+roiArray[j*nrOfRoiValues+4]+"-"+(roiArray[j*nrOfRoiValues+4]+roiArray[j*nrOfRoiValues+5]));
605        finalCropImg=getImageID();
606        setSlice(floor(nSlices/2));
607        getStatistics(area, mean, min, max, std, histogram);
608        roiArray[j*nrOfRoiValues+7]=max;
609        roiArray[j*nrOfRoiValues+8]=std;
610        setAutoThreshold("Otsu"+" dark show");
```

```
611        getThreshold(down,top);
612        roiArray[j*nrOfRoiValues+6]=down;
613        resetThreshold();
614        thresholdedImg=thresholdMotorneuron(finalCropImg,roiArray[j*nrOfRoiValues+6],roiArray[j*nrOfRoiValues+7]);
615        editedMask=editCellMask(thresholdedImg);
616        segSummaryImg=drawCellMaskInResultImg(segSummaryImg,editedMask, j+1,roiArray[j*nrOfRoiValues+0],roiArray[j*nrOfRoiValues+1],roiArray[j*nrOfRoiValues+4]);
617
618
619
620    }
621    selectImage(segSummaryImg);
622    save(outputFolderFilename);
623    roiManager("reset");
624
625    return 1;
626 }
627
628 function drawCellMaskInResultImg(resultImg, cellMask, fillValue, xShift, yShift, zShift){
629    pxValue=fillValue;
630    selectImage(cellMask);
631    slices=nSlices;
632    maskWidth=getWidth();
633    maskHeight=getHeight();
634    xOffset=xShift;
635    yOffset=yShift;
636    zOffset=zShift;
637    imgMask=newArray((maskHeight+1)*(maskWidth+1)*slices);
638    Array.fill(imgMask,0);
639    selectImage(cellMask);
640    for(zMask=1;zMask<slices;zMask++){
641    setSlice(zMask);
642    for(xMask=0;xMask<maskWidth;xMask++){
643        for(yMask=0;yMask<maskHeight;yMask++){
644        pxCoord=((zMask-1)*maskWidth*maskHeight)+((xMask*maskHeight)+yMask);
645        imgMask[pxCoord]=getPixel(xMask,yMask);
646        }
647    }
648    }
649
650    selectImage(resultImg);
651    for(zMask=1;zMask<slices;zMask++){
652    setSlice(zMask+zOffset);
653    for(xMask=0;xMask<maskWidth;xMask++){
654        xResult=xMask+xOffset;
655        for(yMask=0;yMask<maskHeight;yMask++){
656        yResult=yMask+yOffset;
657        if(imgMask[((zMask-1)*maskWidth*maskHeight)+(xMask*maskHeight)+yMask]!=0){
658            setPixel(xResult,yResult,pxValue);
659        }
660        }
661
662    }
663    updateDisplay();
664    }
665
666
667    return getImageID();
668 }
669
670 function editCellMask(inputImgId){
671    selectImage(inputImgId);
672    setThreshold(128,255);
673    setOption("BlackBackground", false);
674    run("Make Binary", "thresholded remaining");
675    run("Fill Holes", "stack");
676    run("Dilate (3D)", "iso=255");
677    run("Dilate (3D)", "iso=255");
678    run("Dilate (3D)", "iso=255");
679    run("Dilate (3D)", "iso=255");
680    run("Fill Holes", "stack");
681    run("Divide...", "value=255 stack");
682    return getImageID();
683 }
684
685 function thresholdMotorneuron(inputImgId,low,max){
686    //LowerThr=Low+Low*0.05;
687    lowerThr=low;
688    higherThr=round(max-low*0.1);
689    if (lowerThr>=higherThr){
690    lowerThr=low;
691    higherThr=max;
692    }
693    if(higherThr>255){higherThr=255;}
694 //    if(higherThr<60){higherThr=60;}
695 //    if(lowerThr>95){lowerThr=95;}
696 //    if(lowerThr<15){lowerThr=15;}
697    print("3d-Hysteresis thresholding with upper value "+higherThr+" and lower value "+lowerThr+".");
698    selectImage(inputImgId);
699    run("3D Hysteresis Thresholding", "high="+higherThr+" low="+lowerThr);
700    thresholdedImgId=getImageID();
701    neuronThresholdLow[filelistIndex]=lowerThr;
702    neuronThresholdHigh[filelistIndex]=higherThr;
703
704    return thresholdedImgId;
705 }
706
707 function drawSeparateCells(filelistIndex){
708    outputfolder=resultfolder[filelistIndex];
709    inputFolderFilename1=segfolder[filelistIndex]+File.separator+segInp1Filename;
710    inputFolderFilename2=segfolder[filelistIndex]+File.separator+segMN1Filename;
711    open(inputFolderFilename1);
712    inputsImg=getImageID();
713 setVoxelSize(voxelSizeFilelist[filelistIndex],voxelSizeFilelist[filelistIndex],voxelSizeFilelist[filelistIndex],calibratedVoxelUnit);
```

```
714        open(inputFolderFilename2);
715        neuronsImg=getImageID();
716        setVoxelSize(voxelSizeFilelist[filelistIndex],voxelSizeFilelist[filelistIndex],voxelSizeFilelist[filelistIndex],calibratedVoxelUnit);
717        selectImage(inputsImg);
718        Stack.getStatistics(voxelCount, mean, min, max, stdDev)
719        if(max!=0){
720        print(inputFolderFilename1+": "+max);
721        Ext.Manager3D_AddImage();
722        }else{
723        print("Warning: "+inputFolderFilename1+"contains no inputs. Skip...");
724        continue;
725        }
726
727        Ext.Manager3D_Count(nrOfInputs);
728        selectImage(neuronsImg);
729        Stack.getStatistics(voxelCount, mean, min, max, stdDev)
730        if(max!=0){
731        print(inputFolderFilename2+": "+max);
732        Ext.Manager3D_AddImage();
733        }else{
734        print("Warning: "+inputFolderFilename2+"contains no cells. Skip...");
735        continue;
736        }
737        logDate();
738
739        Ext.Manager3D_Count(nrOfObjects);
740        nrOfCells=nrOfObjects-nrOfInputs;
741        print("# of cells: "+ nrOfCells+"# of inputs: "+ nrOfInputs+ "# of objects: "+nrOfObjects);
742        selectImage(neuronsImg);
743        origWidth=getWidth();
744        origHeight=getHeight();
745        origSlices=nSlices;
746        close;
747        selectImage(inputsImg);
748        close;
749        noc=0;
750        Ext.Manager3D_MonoSelect();
751        logDate();
752        for(cell=nrOfObjects-nrOfCells;cell<nrOfObjects;cell++){
753        print("cell: "+cell);
754        noc++;
755        newImage("separatedCell_"+noc, "16-bit black", origWidth, origHeight, origSlices);
756        setVoxelSize(voxelSizeFilelist[filelistIndex],voxelSizeFilelist[filelistIndex],voxelSizeFilelist[filelistIndex],calibratedVoxelUnit);
757        actualCellImg=getImageID();
758        Ext.Manager3D_Select(cell);
759        selectImage(actualCellImg);
760        Ext.Manager3D_FillStack(1,1,1);
761        noi=1;
762        for(input=0;input<nrOfInputs;input++){
763
764            Ext.Manager3D_Dist2(cell,input,"bb",dist);
765            Ext.Manager3D_Dist2(cell,input,"r1c2",distRC);
766            Ext.Manager3D_Dist2(cell,input,"c1b2",distCB);
767            print("bb: "+dist+" rNeuronCInput: "+distRC+" cNeuronBInput: "+distCB);
768            if(distRC>distCB){
769            dist=0;
770            print("bb:"+dist);
771            }
772
773
774            if(dist<=distanceThreshold){
775            Ext.Manager3D_Select(input);
776            noi++;
777            Ext.Manager3D_FillStack(noi,noi,noi);
778            }
779        }
780
781        save(outputfolder+File.separator+noc+result1Filename);
782        selectImage(actualCellImg);
783        close;
784        }
785        run("Collect Garbage");
786        return 1;
787    }
788
789    function measureSeparatedCells(filelistIndex){
790        outputfolder=resultfolder[filelistIndex];
791        outputFolderFilename=resultfolder[filelistIndex]+File.separator+result2Filename;
792        inputFolder=resultfolder[filelistIndex];
793        //existing will not be skipped, but possibly incompletely replaced!
794        run("Clear Results");
795        inputFilelist=getFileList(inputFolder);
796        cellResults=newArray(cRLineLength);
797        for(j=0;j<inputFilelist.length;j++){
798        if(endsWith(inputFilelist[j],result1Filename)){
799
800
801            open(inputFolder+File.separator+inputFilelist[j]);
802            actualCellImg=getImageID();
803            setVoxelSize(voxelSizeFilelist[filelistIndex],voxelSizeFilelist[filelistIndex],voxelSizeFilelist[filelistIndex],calibratedVoxelUnit);
804            Ext.Manager3D_AddImage();
805
806            Ext.Manager3D_Count(nrOfObjects);
807            nrOfCells=1;
808            nrOfInputs=nrOfObjects-1;
809            Ext.Manager3D_Measure3D(0,"Vol",cellVolume);
810            Ext.Manager3D_Measure3D(0,"Surf",cellSurface);
811            Ext.Manager3D_MassCenter3D(0,cx,cy,cz);
812            avgInputVolume=0;
813            for(k=nrOfObjects-1;k>0;k--){
814            Ext.Manager3D_Measure3D(k,"Vol",inputVolume);
815            print("Inputvolume "+k+": "+inputVolume);
```

```
816          print('Voxelsize:'+voxelSizeFilelist[filelistIndex]);
817          avgInputVolume=avgInputVolume+inputVolume;
818          }
819          avgInputVolume=avgInputVolume/nrOfInputs;
820
821          cellResults[0]=lsmFilelist[filelistIndex];//Image of origin
822          cellIdEndIndex=indexOf(inputFilelist[j],'_')-0;
823          cellResults[1]=substring(inputFilelist[j],0,cellIdEndIndex);//cellId
824          cellResults[2]=cellVolume;
825          cellResults[3]=cellSurface;//no border correction
826          cellResults[4]=nrOfInputs;
827          cellResults[5]=avgInputVolume;
828          cellResults[6]=cx;//cell centre of mass x-coordinate
829          cellResults[7]=cy;//cell centre of mass y-coordinate
830          cellResults[8]=cz;//cell centre of mass z-coordinate
831          cellResults[9]=inputThreshold[filelistIndex];
832          cellResults[10]=neuronThresholdLow[filelistIndex];
833          cellResults[11]=neuronThresholdHigh[filelistIndex];
834
835
836
837          //write to resulttable
838          resultrow=nResults;
839          setResult("Image", resultrow, cellResults[0]);
840          setResult("Cell", resultrow, cellResults[1]);
841          setResult("Cell volume [um3]", resultrow, cellResults[2]);
842          setResult("Cell surf. [um2]", resultrow, cellResults[3]);
843          setResult("# of inputs", resultrow, cellResults[4]);
844          setResult("avg input vol. [um3]", resultrow, cellResults[5]);
845          setResult("cx", resultrow, cellResults[6]);
846          setResult("cy", resultrow, cellResults[7]);
847          setResult("cz", resultrow, cellResults[8]);
848          setResult("input threshold", resultrow,  cellResults[9]);
849          setResult("lower neuron threshold", resultrow,  cellResults[10]);
850          setResult("higher neuron threshold", resultrow,  cellResults[11]);
851
852
853          updateResults();
854
855
856          cellResultsArray=Array.concat(cellResultsArray, cellResults);
857          Ext.Manager3D_Reset();
858       }
859       }
860       saveAs("results", outputFolderFilename);
861       return 1;
862 }
863 function compileResultsSummary(){
864     outputfolder=directory;
865     outputFolderFilename=outputfolder+File.separator+result3Filename;
866
```

```
867     run("Clear Results");
868
869     for(j=0;j<cellResultsArray.length/cRLineLength;j++){
870     //write to resulttable
871     resultrow=nResults;
872     setResult("Image", resultrow, cellResultsArray[j*cRLineLength+0]);
873     setResult("Cell", resultrow,  cellResultsArray[j*cRLineLength+1]);
874     setResult("Cell volume [um3]", resultrow,  cellResultsArray[j*cRLineLength+2]);
875     setResult("Cell surf. [um2]", resultrow,  cellResultsArray[j*cRLineLength+3]);
876     setResult("# of inputs", resultrow,  cellResultsArray[j*cRLineLength+4]);
877     setResult("avg input vol. [um3]", resultrow, cellResultsArray[j*cRLineLength+5]);
878     setResult("cx", resultrow,  cellResultsArray[j*cRLineLength+6]);
879     setResult("cy", resultrow,  cellResultsArray[j*cRLineLength+7]);
880     setResult("cz", resultrow,  cellResultsArray[j*cRLineLength+8]);
881     setResult("input threshold", resultrow,  cellResultsArray[j*cRLineLength+9]);
882     setResult("lower threshold neuron", resultrow,  cellResultsArray[j*cRLineLength+10]);
883     setResult("upper threshold neuron", resultrow,  cellResultsArray[j*cRLineLength+11]);
884
885     }
886     updateResults();
887     saveAs("results", outputFolderFilename);
888     return 1;
889 }
890
891
892
893
894 function summariseResults(){
895     for(i=0;i<cellResultsArray.length/cRLineLength;i++){
896     resultrow=nResults;
897     setResult("Folder/File", resultrow, cellResultsArray[i*cRLineLength+0]);
898     setResult("Cell no.", resultrow, cellResultsArray[i*cRLineLength+1]);
899     setResult("# of inputs", resultrow, cellResultsArray[i*cRLineLength+2]);
900     setResult("Soma volume [cubic microns]", resultrow, cellResultsArray[i*cRLineLength+3]);
901     setResult("avg. dist. of inputs", resultrow, cellResultsArray[i*cRLineLength+4]);
902     setResult("Avg. inp. vol. [cubic microns]", resultrow, cellResultsArray[i*cRLineLength+5]);
903     setResult("Inp Thr.", resultrow, cellResultsArray[i*cRLineLength+9]);
904     setResult("Neuron Thr.low", resultrow, cellResultsArray[i*cRLineLength+10]);
905     setResult("Neuro Thr. high", resultrow, cellResultsArray[i*cRLineLength+11]);
906
907     }
908     updateResults();
909     saveAs("Results", directory+File.separator+"ResultSummary.xls");
910
911     return 1;
912 }
913
914
915 function inspectCellSegmentation(filelistIndex){
916     outputfolder=segfolder[filelistIndex];
917     inputFolderFilename=segfolder[filelistIndex]+File.separator+segMN1Filename;
```

```
917     inputFolderFilename=segfolder[filelistIndex]+File.separator+segMN1Filename;
918     outputFolderFilename=inputFolderFilename;
919
920     open(inputFolderFilename);
921     maskedImg=getImageID();
922     run("Select None");
923     run("Duplicate...", "duplicate");
924     maskedImgWorkingCopy=getImageID();
925     selectImage(maskedImg);
926     close;
927     selectImage(maskedImgWorkingCopy);
928     run("glasbey");
929     print("Make sure to select the right gray value for each of your edits. You can draw black pixels to delete mask pixels. Be aware that you have to edit each slice ind
930     waitForUser("You can now edit the segmentation mask by means of the ImageJ drawing tools. \n Your changes will be saved automatically.\n If you did not change anythin
931     if(isOpen(maskedImgWorkingCopy)){
932     selectImage(maskedImgWorkingCopy);
933     run("Select None");
934     run("Grays");
935     save(outputFolderFilename);
936     close;
937     return 1;
938     }else{
939     return 0;
940     }
941 }
942
```

Eidesstattliche Erklärung

Ich erkläre hiermit, dass ich diese Dissertation selbstständig ohne Hilfe Dritter und ohne Benutzung anderer als der angegebenen Quellen und Hilfsmittel verfasst habe. Alle den benutzten Quellen wörtlich oder sinngemäß entnommenen Stellen sind als solche einzeln kenntlich gemacht.

Diese Arbeit ist bislang keiner anderen Prüfungsbehörde vorgelegt worden und – abgesehen von unten angegebener Teilpublikation – noch nicht veröffentlicht worden; eine solche Veröffentlichung vor Abschluss des Promotionsverfahrens werde ich nicht vornehmen.

Die Bestimmungen dieser Promotionsordnung sind mir bekannt. Die von mir vorgelegte Dissertation ist von Prof. Dr. rer. nat. Brunhilde Wirth und PD Dr. Thomas Wunderlich betreut und in der Arbeitsgruppe von Prof. Dr. rer. nat. Brunhilde Wirth durchgeführt worden.

Die Teilpublikation ist in Kapitel 9 angegeben.

_____

Ort, Datum   Miriam Peters

Lebenslauf

Miriam Peters, geb. 03.07.1986, München, ledig

SCHULISCHE AUSBILDUNG

September 2004 – Juni 2006	Gymnasium Weilheim i. OB.
Oktober 2002 – Juli 2004	Asam Gymnasium München
September 2002 – Oktober 2002	Staatliche Fachoberschule Weilheim
November 1998 – Juli 2002	Staatliche Realschule Weilheim (Mittlere Reife)
September 1998 – Oktober 1998	Staatliche Realschule Marktoberdorf
September 1996 – Juli 1998	Volksschule Marktoberdorf – Hauptschule
September 1994 – Juli 1996	Sankt-Martin-Volkschule Marktoberdorf
September 1992 – Juli 1994	Volksschule in München – Guldeinschule

AKADEMISCHE LAUFBAHN

Mai 2012 – laufend	Anfertigung einer Dissertation unter Anleitung von Prof. Dr. Brunhilde Wirth, Uniklinik Köln, Institut für Humangenetik
SS 10 – WS 11/12	Pharmaceutical Sciences, Master, LMU München
WS 06/07 – WS 09/10	Pharmaceutical Sciences, Bachelor, LMU München

BERUFSERFAHRUNG

Mai 2012 – laufend	Uniklinik Köln, Institut für Humangenetik
März 2004 – April 2012	Studentischer HiWi am ZAE Bayern in Garching